Noninvasive Imaging of Cardiac Electrophysiology in Pathological Hearts

A DISSERTATION

SUBMITTED TO THE FACULTY OF

UNIVERSITY OF MINNESOTA

BY

Zhaoye Zhou

IN PARTIAL FULFILLMENT OF THE REQUIREMENTS

FOR THE DEGREE OF

DOCTOR OF PHILOSOPHY

Prof. Bin He, Advisor

October 2016

Acknowledgements

I would like to express my most sincere appreciation to my advisor, Prof. Bin He, for his guidance and assistance over the pass years. His insightful advice and consistent support have helped me make steady progress in my dissertation research. His advice on both research and career have been invaluable. I would also like to greatly thank the members of my dissertation committee, Dr. Paul Iaizzo, Dr. Jianping Wang, Dr. Shai Ashkenazi, for their time, support and valuable comments.

I would like to thank Dr. Paul A. Iaizzo, Professor at the University of Minnesota, for his collaboration, very useful discussion, and access to resources in his visible heart lab. I also would like to acknowledge many collaborators in Dr. Iaizzo's lab for collaborating in the patient study, data acquisition, and providing expertise in cardiac electrophysiology experiments.

I would like especially to thank Dr. Lin Y. Chen, cardiologist and professor at the department of medicine, University of Minnesota, for his collaboration, very useful discussion, and access to clinical data.

I would also like to thank Dr. Liqun Wu, at the Department of Cardiology, Ruijin Hospital Affiliated to Shanghai Jiaotong University, for his collaboration, useful discussion, and access to resources in the catheterization lab. I also would like to acknowledge many collaborators in Dr. Wu's lab, especially Dr. Qi Jin, for collaborating in the patient study, data acquisition, and providing expertise in cardiac electrophysiology experiments.

I am also indebted to many lab colleagues who have worked in the Biomedical Functional Imaging and Computation Laboratory at University of Minnesota, who have contributed a lot to the research contained in this dissertation. Special thanks to Dr. Chengzong Han and Dr. Chenguang Liu, for helpful discussion on data analysis and interpretation, for being a lab teammate and wonderful friend. I also graciously thank Dr. Dakun Lai, for his great help in clinical study especially at the initial stage of my research. I would also like to thank Mr. Long Yu and Ms. Ting Yan for their help in experiment and clinical studies and useful discussion in data analysis, and for being wonderful tem members.

Finally, I am grateful to all other lab members whom I have worked with: Dr. Zhongming Liu, Dr. Han Yuan, Dr. Xu Li, Dr. Christopher Wilke, Dr. Xiaotong Zhang, Dr. Gang Wang, Dr. Gang Hu, Dr. Yakang Dai, Dr. Audrey Royer, Dr. Lin Yang, Dr. Leo Mariappan, Dr. Yunfeng Lu, Mr. Keith Jamison, Dr. Huishi Zhang, Dr. Jiaen Liu, Ms. Nessa Johnson, Mr. Alexander Doud, Ms. Kaitlin Cassady, Mr. Abhrajeet Roy, Mr. Bryan Baxter, and Mr. Haijun Shan. Thanks to them for their help in my study and life, and for being friends. Thanks to them for helping collect experimental data, share experience, and for being friends.

Finally this work was supported in part by NIH grant HL080093 and NSF grant CBET-0756331.

Dedication

This dissertation is dedicated to my parents, Ji Zhou and Rongzhen Mo, and my grandparents, Xiaogang Zhou and Shiyin Xiao, for their unwavering love and support throughout my life, and for encouraging me to do everything to the best of my life. I also would like to dedicate this dissertation to my Husband, Fang Liu, for his tremendous love, encouragement, patience, and support during all these years.

Abstract

Noninvasive imaging of cardiac electrical activity is important to both basic cardiovascular research and clinical treatment. It offers the capability to translate body surface electrical signals into cardiac electrical activities and provide direct information on the electrical status of the heart. This dissertation research is aimed to investigate a novel physical-model-based cardiac electrical imaging technique (CEI) under different pathological conditions, for the purpose of further developing it into a clinical useful tool. The CEI technique is adapted to image myocardial infarction and atrial arrhythmias. For the imaging of myocardial infarction, the computer simulation was performed by using a cellular automaton heart model with simulated myocardial infarctions. The simulation results demonstrate that CEI can quantify myocardial infarction and offer the potential to distinguish between epicardial and endocardial infarctions. Furthermore, the CEI approach was adapted to image atrial electrical activities. A frequency-based CEI technique has been proposed to incorporated spectral analysis with the electrical source imaging technique to localize high-frequency drivers during atrial fibrillation (AF). The imaging results were compared with clinical electrophysiological mappings and shown good consistency. The CEI technique was also applied to image atrial excitations in subjects with normal atrial activation and atrial flutter. The results from patients with atrial flutter demonstrated that CEI is also capable of imaging reentrant pattern. The performance of CEI was also experimentally evaluated in *in situ* swine heart with induced ventricular tachycardia. The consistency between the non-invasively imaged electrical activities and computer simulation or the directly measured counterparts from

clinical/animal study implies that CEI is capable of localizing electrically-abnormal substrate, extracting the spectral features during AF, reconstructing the global patterns of atrial and ventricular activation sequences, localizing the arrhythmogenic foci, and imaging dynamically changing arrhythmia on a beat-to-beat basis. The promising results presented in this dissertation study suggest that the cardiac electrical imaging technique has the potential to assist in the diagnosis and treatment of cardiovascular diseases. The present dissertation research takes an important step towards further translating this technique into clinical assistive tool by extending the application to hearts with electrophysiological abnormal substrates, adapting it to image atrial electrical activities, and further evaluating the performance in a clinical setting on human subjects.

TABLE OF CONTENTS

List of Tables

List of Figures

Chapter 1

Introduction

1.1 Overview

Heart disease is classified as a group of heart conditions in which abnormal electrophysiology or structure is presented in the heart or blood vessels. It constitutes a major cause of mortality and disability among the world's population. As a leading cause of death, heart disease accounts for 17.3 million deaths (31.5%) per year (Mozaffarian et al. 2016, Naghavi et al. 2015), producing immense health and economic burdens worldwide. It may be classified into three categories: electrical disorders, circulatory disorders and structural abnormality. In particular, atrial fibrillation (AF) alone affects 2%-3% of the population in developed countries (Zoni-Berisso et al. 2014) and gains significant clinical concerns due to the prevalence. Both pharmacotherapy and nonpharmacologic treatment (Van Wagoner et al. 2015) have been developed and used for the intervention of AF. Radiofrequency ablation that usually guided by electrophysiological mapping is a common treatment on patients who are not responsive to antiarrhythmic medications. However, current strategy of mapping and ablation still produce suboptimal results and need to be further explored: the 1 year ablation success rate for paroxysmal AF patient is only 50-70%, with a much lower number in patient with persistent AF (January et al. 2014). Another type of cardiovascular disease is myocardial infarction (MI), which is the leading cause of sudden death. The border zone of MI or

ischemia is closely related to life-threatening ventricular arrhythmias, and thus the mapping of MI substrate bears significant diagnostic and therapeutic importance.

Understanding the electrical phenomena inside the heart and the underlying pathological mechanisms is of great importance for both clinical disease managements and the basic cardiovascular research. Cardiac electrophysiological mapping become a prominent tool to assist in the clinical treatments, e.g., guiding catheter ablation (Zeppenfeld et al. 2007), mapping infarction substrate (Volkmer et al. 2006) and optimizing cardiac resynchronization therapy (Spragg et al. 2010). It may also play a significant role in the basic research of the pathological mechanisms (Pogwizd et al. 1998). Important advancements have been made on mapping of the endocardial electrical activities by using the catheter mapping technique. The mapping of potential distributions and the activation sequence from the endocardium is an important clinical routine for determining activation patterns, locating the initiation sites of cardiac arrhythmias, and identifying electrical substrates (Iaizzo 2009). There are two mapping systems that are commonly used in catheterization lab (Taccardi et al. 1987, Gepstein et al. 1997, Schalij et al. 1998): the CARTO electroanatomical mapping system and the EnSite noncontact mapping system. The CARTO system records endocardial electrograms (EGMs) in a sequential and direct manner, while the EnSite system measures intracavitary potentials in the blood-filled camber without direct contact with the endocardium. Both are capable of providing endocardial EGMs and activation maps. Though both techniques are successful and widely applied, the technique of catheter-based endocardial mapping is not without limitations. The placement of the catheter is an

invasive procedure and also requires fluoroscopic tracking and/or magnetic guidance to navigate the catheter in the heart and the blood vessel (Wittkampf et al. 2000) (Iaizzo 2009). It's a lengthy procedure and needs to keep patients in prolonged periods of cardiac arrhythmias. In some cases, such mapping technique requires stable rhythms so it may be difficult to perform on patients with complex arrhythmias.

A noninvasive methodology is desirable to image and localize the cardiac electrical activities directly in the heart without the requirement of lengthy invasive procedure. To address the abovementioned issues, research interests have been focused on noninvasive detection, interpretation, and analysis of surface electrocardiography (ECG). In clinical practice, the standard 12-lead ECG, which measures the time-varying electrical signals on the body surface produced by the heart's electrical activity, has been widely used to interpret the internal cardiac electrical information. The body surface potential mapping technique is another classic approach to illustrate electrical activities on the torso by using high-density surface electrodes (Taccardi 1962, Taccardi 1963, Horan et al. 1963, Abildskov et al. 1976, Ideker et al. 1987, Flowers & Horan 1995, De Ambroggi et al. 1997, Akahoshi et al. 1997, Guillem et al. 2009). Yet the surface recordings/mappings measures a summation of all cardiac signals from different vectors on the body surface and thus reflect the actual cardiac electrical activities in the heart domain in an indirect manner. Therefore, many investigators have been working on combining the surface recordings and subject-specific heart-torso model to reconstruct the cardiac electrical activities by solving the inverse problem. Typical approaches include the reconstruction of epicardial potentials (Barr et al. 1977, Franzone et al. 1985, Yamashita & Takahashi

1984, Throne & Olson 1994, Shahidi et al. 1994, Oster et al. 1997, Greensite & Huiskamp 1998, MacLeod & Brooks 1998), activation isochrones on the heart surface (Cuppen & Van Oosterom 1984, Huiskamp & Greensite 1997, Pullan et al. 2001, Tilg et al. 2002, Greensite 2004), and the cardiac electrical activity throughout three-dimensional myocardium (He & Wu 2001, He et al. 2003, He et al. 2002, Ohyu et al. 2002, Skipa et al. 2002, Zhang et al. 2005, Liu et al. 2006, Liu et al. 2006, Nielsen et al. 2007, Liu et al. 2008, Han et al. 2008, Wang et al. 2011, Han et al. 2011, Han et al. 2012, Han et al. 2013, Han et al. 2015, Yu et al. 2015). Such techniques translate the body surface potential information into the heart domain, and therefore provide significant clinical value in the diagnosis and intervention of cardiovascular diseases.

1.2 Significance and Motivations

The present dissertation study aims to evaluate the performance of a novel physical-model-based cardiac electrical imaging (CEI) technique in pathological conditions under clinical settings. By coupling multi-channels body surface ECGs with individual heart-torso geometric model, the CEI technique is capable of providing detailed reconstructions on cardiac electrical activities. In previous studies, a large amount of work has been done to validate the technique by using animal models with ventricular paced rhythms and arrhythmias in experimental setting (Han et al. 2008, Han et al. 2011, Han et al. 2012, Han et al. 2013). The present dissertation research takes an important step towards further translating this technique into clinical application by extending the application to hearts with electrophysiological abnormal substrates, broadening the application from imaging ventricular arrhythmias to atrial arrhythmias, and further evaluating the performance in a

clinical setting on human subjects.

The present study could overcome the limitations of the invasive catheter-based mapping technique, which is widely used in the clinical practice and also facilitate current noninvasive cardiac electrical imaging techniques. For instance, it is of great clinical significance for physicians to localize the drivers of AF. However, current noninvasive methods for atrial fibrillation are based on epicardial potential imaging, which did not provide information from the perspective of frequency analysis. In the present study, we have brought in the concept of spectral analysis into the cardiac source imaging technique and are able to localize AF drivers which are featured by high-frequency electrical activities in both paroxysmal and persistent patients. The CEI method has been previously used to image hearts with normal electrophysiological properties. In the present study, we further utilized it in hearts with abnormal electrical substrates such as MI. The extended applications of this noninvasive imaging technique may also provide an alternative for noninvasive imaging of electrical substrates and AF drivers, thus advancing the clinical diagnosis of MI and ischemia and the pre-surgical planning by significantly decreasing the risks and expenses related to current clinically-applied invasive procedures.

1.3 Scope of Dissertation

In chapter 2, a brief literature review is given on the electrophysiology of the human heart, the background knowledge of ECG and the body surface potential map (BSPM), the noninvasive cardiac source imaging technique. Important previous

researches related to the current study are also reviewed.

In chapter 3, computer simulations of myocardial infarction are conducted to investigate the feasibility of localizing and quantifying MI. Transmural and surface MI were simulated in a realistic geometric model and the performance of 3D-CEI technique for MI quantification is evaluated.

In chapter 4, a frequency-based noninvasive imaging concept has been proposed to detect the high-frequency sources in atrial fibrillation. Clinical study is conducted to evaluate the performance of the frequency-based CEI technique. The imaged high-frequency sites are compared with ablation area from CARTO map. Both paroxysmal and persistent AFs have been studied, and the imaging results are consistent with ablation outcomes. The reasonable results indicate the potential of this novel CEI technique as an assistive tool for guiding ablation and understanding the underlying arrhythmic mechanism.

In chapter 5, we further extend the application of the CEI technique to the atria. The CEI approach has been utilized to image atrial activation for the first time. The results suggest that CEI is capable of delineating both focal and reentrant mechanisms in good consistency with EP findings and literatures, and that it offers a noninvasive manner to define arrhythmic mechanism and guide catheter ablation.

In chapter 6, we extend the experimental investigation of the CEI technique in the intact swine heart for the purpose of evaluating the performance of ventricular activation imaging, which provides closer approximation to the clinical setting as compared with previous studies in rabbits and canines. The noninvasive imaging results are compared

with the simultaneous measurements from endocardial noncontact recordings. The good results indicate the potential of this novel CEI technique as an assistive tool in clinical practice for ventricular imaging.

In chapter 7, the major contributions of the present dissertation research are summarized. Recommendations for future works are also discussed.

Chapter 2

Background

2.1 Cardiac Electrical Activity

The heart works like an automatic pump, transporting blood to the lungs and peripheral organs by mechanical contraction of the heart muscles and providing oxygen for human survival needs. It is the electrical excitation of the heart which provides the fundamental of the mechanical contraction of the cardiac tissues. Anatomically, the heart is consisted of the right atrium (RA), the left atrium (LA), the right ventricle (RV) and the left ventricle (LV). A normal heart rhythm (also the so-called sinus rhythm) starts from the sinoatrial node (SA node) in the RA, which serve as a natural pacemaker of the heart, transmit to the ventricles through the AV node, and further conducts through the left and right bundle of His to Purkinje fibers to excite the LV and the RV. The electrical excitation propagates through the time-ordered conduction system and cause depolarization of the heart muscle, which consequently triggers mechanical contraction of the heart to pump bloodstream to the cardiovascular circulatory system.

The electrical excitation of the cardiac muscle is usually resulted from the electrochemical reactions of the ion channels in excitable cells (Malmivuo & Plonsey 1995). The inflowing and outflowing ions across the cellular membrane through ion channels lead to dramatic change in membrane potential. Once the membrane potential reaches certain threshold, an action potential is produced as the cell shift from the resting sate to the excited state. A depolarization phase of the action potential is featured by a

rapid rise in membrane potential and a result of the influx of a large amount of sodium ions. A repolarization phase subsequently occurs as a result of the influx of the potassium ions.

2.2 Cardiovascular Diseases and Clinical Electrophysiological Mapping

Cardiac electrophysiological mapping is an important tool for understanding the initiation and maintenance of arrhythmias and the underlying pathophysiological mechanisms. It has been widely used in clinical practice and critical for the selection of treatment strategy. The applications include guiding catheter ablation (Zeppenfeld et al. 2007) (Volkmer et al. 2006), optimizing cardiac resynchronization therapy (Spragg et al. 2010), and more. Mapping of cardiac electrical activities can provide endocardial potential distributions over time, activation sequence, and therefore assist in localizing ectopic foci, identifying the electrically-abnormal substrates, reconstructing global activation patterns, and guiding the catheter ablation. (Iaizzo 2009). In clinical practice, two mapping systems are commonly used in the catheterization lab: the CARTO electroanatomical mapping system and EnSite noncontact mapping system. CARTO is a non-fluorescent electroanatomic catheter mapping system, which uses ultralow electromagnetic field to navigate the movement of catheter in the heart chamber and veins (Gepstein et al. 1997, Schalij et al. 1998). The system allows to reconstruct the chamber's endocardial geometry and records unipolar EGMs at multiple points of the endocardium, and then relates the potentials to the geometry to constitute the endocardial potential maps and activation maps. This system is also called sequential mapping system

as the electrical field and anatomic information are acquired in a point-by-point manner by navigating the catheter tip along the endocardial wall. It has widespread clinical use and has been applied for the study of a wide range of arrhythmias, e.g., atrial fibrillation, atrial flutter and ventricular tachycardia. Specifically, it has also been utilized to study the high-frequency source during AF by reconstructing endocardial dominant frequency maps as a derivative of the recorded endocardial EGMs (Sanders et al. 2005). Another clinical tool, which belongs to the category of continuous mapping systems, uses an noncontact multielectrode probe to record the intracavitary potentials in the blood-filled chamber (Taccardi et al. 1987). The potentials over the endocardial surface are inversely reconstructed from the beat-to-beat potential measurements on the multi-array catheter probe (Gornick et al. 1999, Jia et al. 2000, Kadish et al. 1999, Khoury et al. 1998, Liu et al. 1998, Sun et al. 1998). Although these catheter-based mapping techniques are successful and have played significant roles in the clinical diagnosis and treatment, they are not without limitation. The placement of the catheter is an invasive procedure and also requires fluoroscopic/magnetic tracking to precisely navigate the catheter in the heart (Iaizzo 2009, Wittkampf et al. 2000). It is a lengthy procedure and needs to keep patients in lengthened periods of cardiac arrhythmias. In some cases, the mapping technique requires stable rhythms so it may be difficult to perform on patients with complex arrhythmias.

2.3 Electrocardiography and Body Surface Potential Mapping

Current clinical noninvasive detection of the cardiac electrical activity is to record

thoracic electrical potentials over a period of time by attaching electrodes to the outer surface of the skin. The electrodes are placed in standard positions and provide electrical activities from 12 vectors, which is the so-called 12-lead ECG. The 12-lead ECG system is consisted of three bipolar limb leads (Lead I, II and III), six unipolar precordial leads (Lead V1 to V6) grounded by Wilson Center Terminal (Wilson et al. 1934), and three augmented unipolar leads (aVR, aVL, and aVF) (Goldberger 1942). The 12-lead ECG gives important electrical information on cardiovascular system and plays a significant role in clinical diagnosis of heart diseases. The placement of electrodes for 12-lead ECG system is standardized and consisted of 9 recording sites. On one hand it provides a consistent interpretation to the cardiovascular disorder, but on the other hand the summation of cardiac electrical information conveyed from a limited number of vectors may not be able to provide sufficient spatial information.

A lot of efforts have also been dedicated into the investigation of body surface potential mapping techniques, which measures multiple channels of ECGs from various sites of the torso to give instant spatial potential maps over the body surface (Taccardi 1963) and creates the so-called BSPM. A number of researchers dated back to 1960s had studied BSPM and its derivatives on healthy human subjects, and patients with various cardiac disorders (Taccardi 1962, Taccardi 1963, Akahoshi et al. 1997, SippensGroenewegen et al. 2000). The large amount of work done in the past 40 years has shown that BSPM may provide more valuable diagnostic information than standard 12-leads, as it is capable of giving both spatial and temporal description on the electrical condition of the heart (Abildskov et al. 1976, Flowers & Horan 1995, Akahoshi et al.

1997, Mehra et al. 1983, Mirvis 1980, He & Cohen 1992). One important feature of the BSPM is that the negative and positive potentials on the BSPM map are directly associated with the excitation wavefronts in the heart (Spach & Barr 1971), providing a spatial-temporal manner to noninvasively interpret cardiac electrical excitation from the outer surface. Although BSPM provides electrical information in a more comprehensive way, it is still not able to give direct and detailed depiction of the cardiac electrical activity considering the fact that electrical signals received over the body surfaces are compromised by the "smearing" effects of the heart-torso volume conductor and that the potential recorded from the thorax are always a summation of all the cardiac electrical activities.

2.4 Cardiac Electrical Imaging

Noninvasive cardiac electrical imaging techniques reconstruct detailed electrical activities in the heart and thus overcome the above-mentioned limitations of 12-lead ECG and BSPM. The cardiac electrical imaging technique includes ECG forward problem and ECG inverse problem and each will be elaborated in the following chapters (Fig. 1).

2.4.1 ECG Forward Problem

The ECG forward problem usually entails the calculation of electrical fields over the body surface by projecting given cardiac electrical sources onto the thorax. The equivalent cardiac sources presenting the realistic electrical activities in the heart can be

defined in different contexts, such as equivalent current density, epicardial potentials, or moving dipoles. Usually, the sources are immersed in bounded volume conductors with predefined geometry and electrical properties (e.g. conductivities). Once the details of the

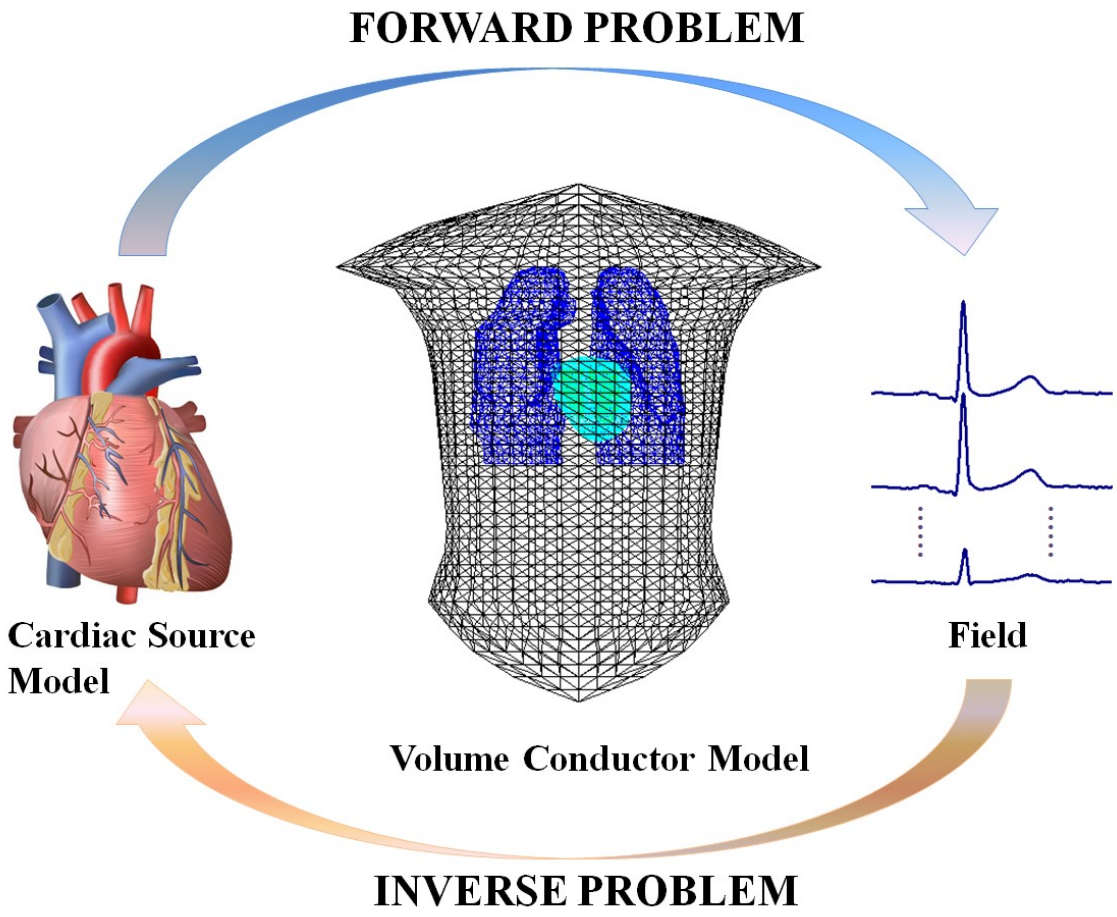

Fig. 1. ECG forward and inverse problem.

source and the volume conductor are provided, the forward problem has a unique solution and the electrical field can be calculated with certain accuracy (Malmivuo & Plonsey 1995).

In general, the electrical field of the heart-torso volume conductor can be governed

by the partial differential equations (He 2004, Malmivuo & Plonsey 1995), which can be discretized into a set of linear equations. There are several underlying assumptions which are important to the forward problem (He 2004, Nash & Pullan 2005). First of all, the electrical field is assumed to be quasistatic, which means at each time instant the potential field on the body surface is solely depend on the simultaneous electrical status of the cardiac sources. As a consequence, the forward problem can be thought of as a series of problems independent in time – one for each time instant. Second, the source-to-field transfer matrix is assumed to be constant over time - the geometry as well as the tissue conductivity remains unchanged, and the cardiac motion is ignored here.

The solutions for the forward problem can be categorized into the surface methods and the volume methods, and the relating applications have been detailed in the review papers (Gulrajani 1998, Gulrajani 2004). The surface methods, which are also termed the boundary element methods (BEM), consider the interfaces between different torso regions and digitize the boundary to represent the numerical torso model. Each region of interest is assumed to be homogenous, but the conductivities may be different between regions. In the volume method, the entire three-dimensional volume is represented by a combination of tetrahedral and hexahedral, and it is the only way to incorporate individual regions of varying conductivity (Gulrajani 1998). The volume methods can be further subdivided into 3 categories: finite-element Method, finite-difference method, and finite-volume method. In general, both the surface method and the volume method have their advantages and drawbacks, thus a combination of both methods may complement each other. The surface methods can be used where the torso is isotropic and

the volume methods can be used where it is anisotropic. This combination takes advantage of any computational savings afforded by the surface methods, while at the same time allows the handling of anisotropies.

2.4.2 ECG Inverse Problem

In contrast to the ECG forward problem, which starts with the selected equivalent cardiac sources inside the conductor and calculate the corresponding electrical potential on the surface, the ECG inverse problem reconstruct the cardiac source distribution from the body surface potential fields through certain mathematical manipulation (He & Liu 2010). Obviously, it is the ECG inverse problem that has clinical importance in medical application of bioelectric phenomena (Malmivuo & Plonsey 1995). Due to the fact that there are infinite equivalent cardiac sources, which may contribute to the same body surface potential measurements, the ECG inverse problem does not possess a mathematically unique solution like the forward problem does.

Tremendous efforts have been made to overcome the difficulty of non-uniqueness of ECG inverse problem by using different formulations of equivalent cardiac electrical generators. Among these works, cardiac electrical activities have been represented by a limited number of equivalent sources, such as a few moving dipoles (Mirvis et al. 1977, Gulrajani et al. 1984a, Gulrajani et al. 1984b, Armoundas et al. 2003, Lai et al. 2010), multipoles (Geselowitz 1960), multiple fixed dipole arrays (Barber & Fischmann 1961, Bellman et al. 1964). However, the fact that cardiac electrical activities exist widely over the heart domain indicates that distributed source models are more suitable to depict the

distributed electrical activities. One approach is to reconstruct the epicardial potentials from the BSPM (Barr et al. 1977, Franzone et al. 1985, Yamashita & Takahashi 1984, Throne & Olson 1994, Shahidi et al. 1994, Oster et al. 1997, Greensite & Huiskamp 1998, MacLeod & Brooks 1998). This method constructs a transfer matrix relating epicardial to body surface potentials without making any assumption about the electrical activities in the internal heart region. It has been investigated by several groups in both animal models and human subjects, under normal or abnormal cardiac electrophysiological conditions. Another approach reconstructs activation isochrones over the epicardial and endocardial surfaces, and is called heart surface isochrones imaging (Cuppen & Van Oosterom 1984, Huiskamp & Greensite 1997, Pullan et al. 2001, Tilg et al. 2002, Greensite 2004). This approach reconstructs an equivalent uniform dipole layer on both endocardium and epicardium to represents the cardiac electrical activities, lining the activated regions of the heart surfaces. In the previous studies, this method has been investigated in human subjects, under both normal, paced, and arrhythmic conditions (Berger et al. 2006, Van Dam et al. 2009, Berger et al. 2011). A modern approach to ECG inverse problem is the 3D cardiac electrical imaging pioneered by He and his colleagues since 2001 (He & Wu 2001, Li & He 2001, He et al. 2003, He et al. 2002, Ohyu et al. 2002, Skipa et al. 2002, Zhang et al. 2005, Liu et al. 2006, Liu et al. 2006, Nielsen et al. 2007, Liu et al. 2008, Han et al. 2008, Wang et al. 2011, Han et al. 2011, Han et al. 2012, Han et al. 2013, Yu et al. 2015).

Another challenge of solving the ECG inverse problem lies in the ill-posedness of the problem, so that small uncertainties in the input data, like geometric errors and

measurement noises, may lead to significantly unstable solutions. Therefore, the techniques of regularization must be applied to suppress the effects of inevitable errors due to imposing constrains on the inverse solution. In this regard, many investigators have been working on exploring the regularization techniques in order to obtain stable and electrophysiological reasonable inverse solutions (Greensite 2004, Tikhonov & Arsenin 1977, Hansen & O'Leary 1993, Johnston & Gulrajani 1997, Brooks et al. 1999).

Considering the fact that the origins of the arrhythmias typically located at subendocardium and sometimes at epicardium or even intramural sites (Pogwizd et al. 1998), it is important to gauge the physiological or pathophysiological status throughout the 3-dimensional myocardium space by using the inverse solutions. Therefore, although the abovementioned challenges of inverse problem can be tackled, either by using equivalent source models to obtain unique solution or by imposing constraints on the solution and using regularization schemes to suppress the effects of noise, additional methods are needed to noninvasively image the electrical activities over the 3-D myocardium volume. Much efforts has been dedicated in the past decades to develop such method (He & Wu 2001, Li & He 2001, He et al. 2003, He et al. 2002, Ohyu et al. 2002, Skipa et al. 2002, Zhang et al. 2005, Liu et al. 2006, Liu et al. 2006, Nielsen et al. 2007, Liu et al. 2008, Han et al. 2008, Han et al. 2011, Han et al. 2012, Han et al. 2013, Li & He 2001, Wang et al. 2010, Zhou et al. 2015). One of the 3D inverse methods, which is namely the heart-model-based approach, is to estimate the 3D cardiac electrical activities by using a heart-excitation model and minimize the residuals between estimations and measurements with a nonlinear optimization function (He et al. 2003, He

et al. 2002, Li & He 2001). This approach has been evaluated in both the computer simulation and animal experiments, and the results show high consistence between the estimated activation time and "true" simulated activation time in simulations (He et al. 2002, Li & He 2001) or the measured activation time in experiments (Zhang et al. 2005, Liu et al. 2008). Moreover, potential distributions over the 3D ventricular myocardium have been estimated from the BSPMs by using this heart-model-based cardiac electrical imaging method (He et al. 2003, Liu et al. 2012). In recent years, a physical-model-based 3D cardiac electrical imaging (3D CEI) approach has been proposed to mathematically model the cardiac electrical activity in 3-dimensional myocardial volume using equivalent current density (ECD) distribution without the needs of a priori information of cardiac electrophysiology (Liu et al. 2006). The activation sequences are therefore extracted based on the inverse solution of ECD to reconstruct the activation map of the 3D ventricular myocardium. This novel 3D CEI approach is based on the biophysical relationship between the cardiac excitation wavefront and the current density, and requires minimal knowledge of cardiac electrical properties. This physical-model-based 3D CEI method has been investigated in both computer simulation and animal experiments under normal, pacing, and arrhythmic conditions, and has been proven to be promising in various cardiac physiological conditions (Liu et al. 2006, Liu et al. 2006, Han et al. 2008, Han et al. 2011, Han et al. 2012, Han et al. 2013, Zhou et al. 2015, Han et al. 2007b, Han et al. 2007a, Han et al. 2009, Han et al. 2010).

2.5 Three-dimensional cardiac electrical imaging

In the previous section, we have discussed the need for developing the 3D CEI technique. The physical-model-based cardiac electrical imaging technique models the cardiac electrical activities as equivalent source, and the cardiac activation could thus be extracted based on fundamental biophysical principles. The materials in this section have been previously published (Liu et al. 2006) but we include them for the purpose of clarity.

The bidomain theory states that the cellular architecture of the heart can be simplified into a macroscopic continuum model that consists of two domains: the intracellular domains and the extracellular domains. And the two domains are coupled by the continuity of the transmembrane current of individual cells which flows from the intracellular domain to the extracellular one through a theoretical membrane (Tung 1978, Miller & Geselowitz 1978). Based on the bidomain theory, the electrical field within the heart-torso volume conductor is governed by the following equation:

$$\nabla \cdot [(G_i(r) + G_e(r)) \nabla \phi_e(r,t)] = \nabla \cdot [-G_i(r) \nabla \phi_m(r,t)] \tag{2.1}$$

where G_i and G_e are the effective conductivity tensors for intracellular space and extracellular space, respectively, ϕ_m is the transmembrane potential, and ϕ_e is the extracellular potential. The equivalent current density $\vec{j}_{eq}$ is defined as:

$$\vec{j}_{eq}(r,t) = -G_i(r) \nabla \phi_m(r,t) \tag{2.2}$$

and equation (2.1) becomes

$$\nabla \cdot [(G_i(r) + G_e(r)) \nabla \phi_e(r,t)] = \nabla \cdot \vec{J}_{eq}(r,t) \tag{2.3}$$

Equation (2.3) suggests that $\vec{j}_{eq}$ can serve as an equivalent source to compute the

extracellular potentials.

In CEI, the electrical sources throughout the three-dimensional myocardium are represented by the distributed equivalent current density. Once geometrical heart-torso model is tessellated and the electrical conductivity of relevant tissues and organs are assigned based on prior knowledge (Malmivuo & Plonsey 1995, Gabriel et al. 1996), applying the boundary element model yields a discrete matrix as (2.4)

$$\Phi(t) = LJ(t) \tag{2.4}$$

Where $\Phi(t)$ is an $M \times 1$ column vector of body surface potentials from M body surface electrodes at time t, $J(t)$ is a $3N \times 1$ column vector of ECD distribution from N myocardial grid points, and L is the $M \times 3N$ transfer matrix that relates the ECD distribution to the body surface measurements. Equation (4) is used to compute the body surface potentials $\Phi(t)$ at M electrode positions from the equivalent cardiac source $J(t)$ at N given myocardial locations for any time instant t.

This linear inverse problem was solved using the weighted minimum norm (WMN) estimation (Liu et al. 2006, Pascual-Marqui 1995, Wang et al. 1992), which minimizes the following objective function:

$$\min_{J(t)} (\| \Phi(t) - LJ(t) \|_2^2 + \lambda \| WJ(t) \|_2^2) \tag{2.5}$$

Where W is the Kronecker product of a 3×3 identity matrix I and a $N \times N$ diagonal matrix Ω. λ is the regularization parameter, which can be determined by the L-curve method (Christian, 1992).

2.6 Intracavitary Potential-based Inverse Solution

Besides the BSPM-based inverse solutions, important advancements have also been made on the development of intracavitary potential-based inverse solution, which images cardiac electrical activity from the electrical potentials measured within the blood cavities using catheter technology. In one of the formations, a cavitary noncontact catheter-probe with multi-electrode array is placed in the blood cavity to record the beat-to-beat electrical potentials. These intracavitary potential measurements are then used to inversely reconstruct the electrical potentials over the endocardial surface (Taccardi et al. 1987). Both animal experiments and clinical studies have been performed to validate the technique (Gornick et al. 1999, Jia et al. 2000, Kadish et al. 1999, Khoury et al. 1998, Liu et al. 1998, Ciaccio et al. 2004). While the endocardial approach provides a minimal invasive way to image and localize the electrical activity on the endocardial surface, the performance is limited when the activation initiates from the myocardial locations far from the endocardial surface. Recently, efforts have been made to extend the inverse solution from endocardium into 3D myocardium space (He et al. 2007). Both the computer simulation (He et al. 2007) and animal experiments (Liu et al. 2012) show the feasibility of this novel method. Although promising, this novel technique still requires sophisticated clinical manipulations to place the catheter, and the procedure may cause clinical complications on patients with unstable hemodynamics.

Chapter 3

Noninvasive Imaging of Myocardial Infarction from BSPM

3.1 Introduction

Myocardial infarction is a major public health problem that is usually caused by the occlusion of coronary arteries (Roger et al. 2011). MI increases the risk of sudden cardiac death by creating electrophysiological abnormal substrate responsible for triggering life-threatening ventricular arrhythmias. Thus the identification of the MI substrate bears diagnostic and therapeutic importance for the clinical management of cardiac arrhythmias. Efforts have been made toward the development of invasive and noninvasive diagnostic tools, including biochemical markers, single-photon-emission, computed tomography, echocardiography (Antman et al. 2000), delay-enhanced magnetic resonance imaging (Pennell 2010), as well as catheter mapping techniques (Codreanu et al. 2008). Among these clinical techniques, the catheter mapping method is capable of defining the MI substrate based on the direct electrophysiological recordings of the myocardial tissue. However, such invasive techniques require prolonged procedures, and may put patients at risk of sudden cardiac death (Volkmer et al. 2006). By contrast, the noninvasive cardiac electrical imaging technique utilizes the body surface ECG to reconstruct the cardiac electrical activities, thus is able to bypass the above-mentioned limitations and possesses the potential to delineate the MI substrate based on electrical properties and further to assist in the clinical treatment of substrate-related heart arrhythmias.

In the previous chapter, we have introduced a physical-model-based 3D CEI approach, which has been proposed to mathematically model the cardiac electrical activity in 3-dimensional myocardial volume using equivalent current density distribution without the needs of a priori information of cardiac electrophysiology (Liu et al. 2006). Both the computer simulation (Liu et al. 2006, Han et al. 2008) and animal experiments (Han et al. 2008, Han et al. 2008, Han et al. 2011, Han et al. 2012, Han et al. 2013, Han et al. 2007b) showed the promises of this approach for extracting 3D cardiac activation sequence from the inverse solution of ECD distribution. In the present study, we have developed a new method to non-invasively image and localize the MI substrate based on the 3D CEI. We estimate MI substrate based on the physical relationship between equivalent current source and the transmembrane potentials. ECD distributions during S-T segment are inversely estimated and used to identify the MI substrate. A series of computer simulations were performed to comprehensively evaluate the proposed method. The non-invasively identified MI substrates were quantitatively compared with the simulated MI substrates to assess the performance.

This chapter has been published at IEEE Transactions on Biomedical Engineering (Zhou et al. 2015).

3.2 Materials and Methods

3.2.1 Principle of Imaging MI Substrates from ECD Distribution

MI is caused by the blockage of coronary blood supply, followed by subsequent remodeling processes, which create substrates with altered electrophysiological

properties in terms of low action potential amplitude (Lazzara et al. 1978). This results in infarcted tissues, which are considered electrically unexcitable throughout the whole cardiac cycle or with much smaller action potential amplitude as compared with the normal action potential. During S-T segment, the transmembrane potential (TMP) of normal myocardial cells rises to the plateau potential while the TMP of infarcted myocardial cells remains in low potential (Lazzara et al. 1978). This creates a voltage difference, and thus the high magnitude of the spatial gradient of TMP surrounding the MI border, as shown in Fig. 2(D). In addition to TMP, this important feature of the TMP spatial gradient during S-T segment provides an alternative way to characterize the MI substrates. According to the bidomain theory (Miller & Geselowitz 1978), the local ECD at each myocardial site is defined to be proportional to the TMP spatial gradient, and therefore the MI substrates could be identified from the ECD distribution throughout the myocardium during the S-T segment.

In previous chapter, we have presented the details for forward and inverse computation of the CEI technique. It is noted that the solution of the linear inverse problem leads to a smoothed distribution of ECD, especially at areas with a large ECD magnitude. Due to the spatial smoothness effect of the inverse operator, the spatial distribution of the estimated ECD would mostly likely overlap with each other. The tissue volume within the MI would most likely have a large ECD relative to the normal tissue outside the MI area due to the spatial summing of ECD within a confined MI area. Hereby, the MI substrate and the edge would have an ECD magnitude higher than the normal tissue during the S-T segment, and thus can be quantified by setting a pre-defined

threshold. The threshold can be defined as a certain percentage of the spatial ECD maximum magnitude, expressed as:

$$Threshold = \partial * \arg\max(J_{ave}) \tag{3.3}$$

where ∂ is the predefined threshold and J_{ave} is the temporal average of 30 ms of the $J_{est}(t)$ which is inversely estimated from S-T segment of BSPM. In the present study, myocardial tissue with a J_{ave} that is higher than the threshold is identified as the substrate of infarction.

3.2.2 Computer Simulation

To assess the performance of the proposed method, a series of computer simulations were performed using a cellular automaton heart model as used in previous studies (He et al. 2002, Li & He 2001, Li & He 2004) to simulate the ventricular electrical activity during MI. The spatial resolution of the ventricular model was 1.5mm. The electrical properties of the myocardial tissue were defined based on the knowledge of cardiac anatomy and electrophysiology (He et al. 2003, Li & He 2004). Specifically in the heart excitation model, the excitation conduction velocity for the infarcted unit is set to 0 m/s so that no tissue in the area will be activated. MI tissue is modeled with an action

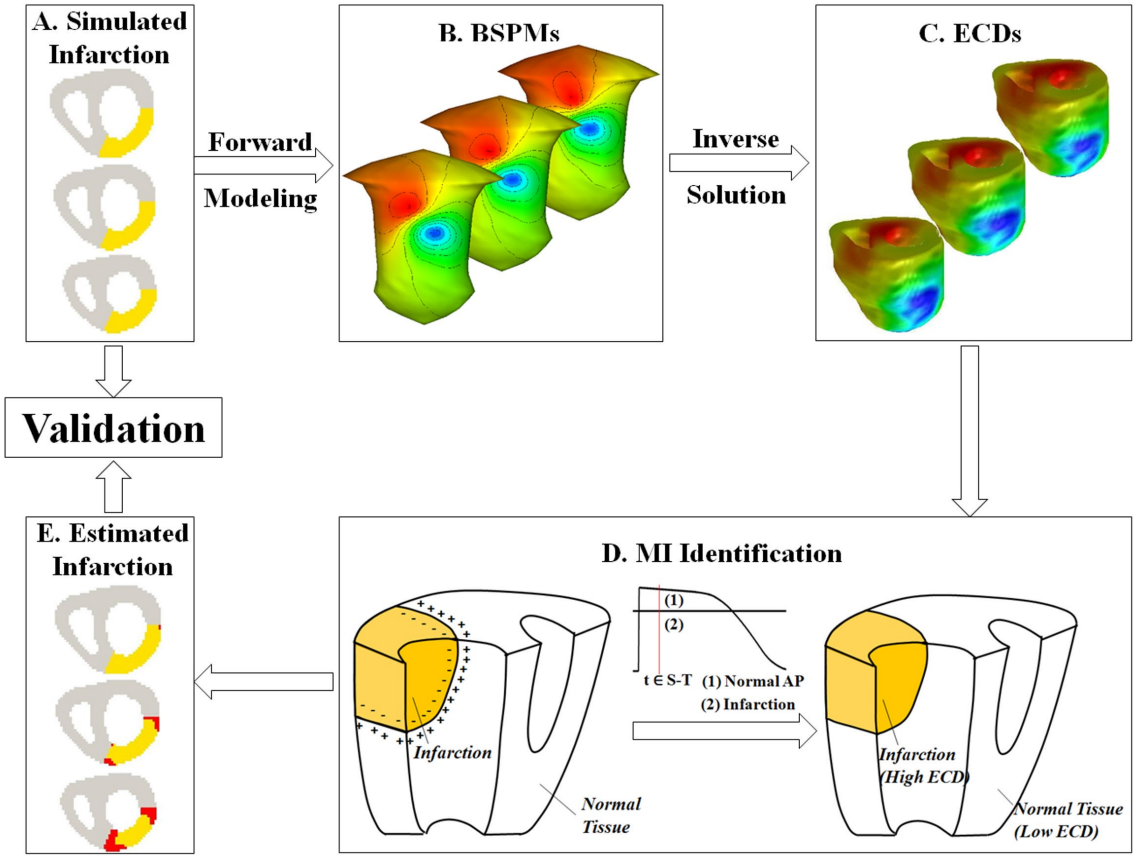

Fig. 2. Framework of computer simulation and the principle of proposed method. AP = action potential; BSPM = body surface potential map; ECD = equivalent current density; MI = myocardial infarction.

potential of constant zero. As isolated right ventricle (RV) infarction only occurs in 3% of MI patients and may not significantly alter the cardiac output, it is considered to be less critical in clinical applications compared with the left ventricle (LV) infarction (Kinch & Ryan 1994, Andersn et al. 1987). Therefore the computer simulations were performed in LV. The LV myocardium was divided into 17 segment based on the American Heart Association (AHA) standard (Cerqueira et al. 2002). This heart model was embedded in a realistic-geometry inhomogeneous heart-torso volume conductor model, and body surface potentials were generated based on forward computation. The

ECD was then reconstructed from BSPM during S-T segment with a time window of 30ms and averaged over time. The MI substrate was defined, based on the predefined threshold.

In total, 114 transmural MI substrates were simulated with different sizes and various locations throughout the entire LV. Single or a combination of multiple neighborhood segments were selected as the infarcted tissue with altered electrophysiological properties. There were 26 anterior infarctions, 41 lateral infarctions, 20 posterior infarctions, 21 septal infarctions and 6 apical infarctions, with the size ranging from 5.1% to 38.2% of the LV volume.

Computer simulations were also conducted to assess the performance of the proposed approach in identifying non-transmural MI substrates located at the epicardium and the endocardium. We simulated 91 epicardial infarctions and 36 endocardial infarctions at various LV locations, with a thickness of approximately 1/3 - 1/2 of the transmural MI substrates. The sizes of the epicardial infarctions ranged from 5.6% to 22.9% of the LV volume, while the sizes of the endocardial infarctions varied from 4.4% to 14.9% of the LV volume.

To investigate the effect of noise level on the proposed method, the forward calculated BSPMs were contaminated by Gaussian white noise (GWN) with different noise levels of 0 μV, 5 μV, 10 μV, 15 μV, 20 μV, and 30 μV, assuming that the peak to peak value of sinus BSPM is 3 mV, though we are mapping MI substrates from S-T segment. Meanwhile, we used different numbers of electrodes (256, 205, 182, 156, and 98) to examine the effect of electrode density on the proposed method with additive

10μV level GWN. The effect of volume conductor modeling errors was also studied by adding 10% torso geometry uncertainty and 4mm heart position uncertainty.

3.2.3 Statistical Analysis

Four parameters were computed to quantify the performance of the proposed method: sensitivity, specificity, Dice's coefficient, and distance between the centers of gravities (DCG). Sensitivity represents the percentage of the accurately estimated infarction in the true infarction, and specificity represents the percentage of the accurately estimated normal region in the true normal tissue. Dice's coefficient compares the similarity between the real infarction and the estimated infarction. They are defined as: sensitivity = TP/(TP+FN) and specificity = TN/(TN+FP), Dice's coefficient = 2TP/(TP+FN+TP+FP), in which true positive (TP) is the volume of true infarction that is correctly identified as infarction, false negative (FN) is the volume of true infarction that is mistakenly considered as normal tissue, true negative (TN) is the volume of true normal tissue that is correctly identified as normal, and false positive (FP) is the volume of normal tissue that is mistakenly characterized as infarction. DCG is defined as the Euclidean distance between the gravity center of the estimated infarction and that of the true infarction.

3.3 Results

3.3.1 Transmural Infarctions

Fig. 3 depicts examples of imaging the transmural MI substrates that were located

at the

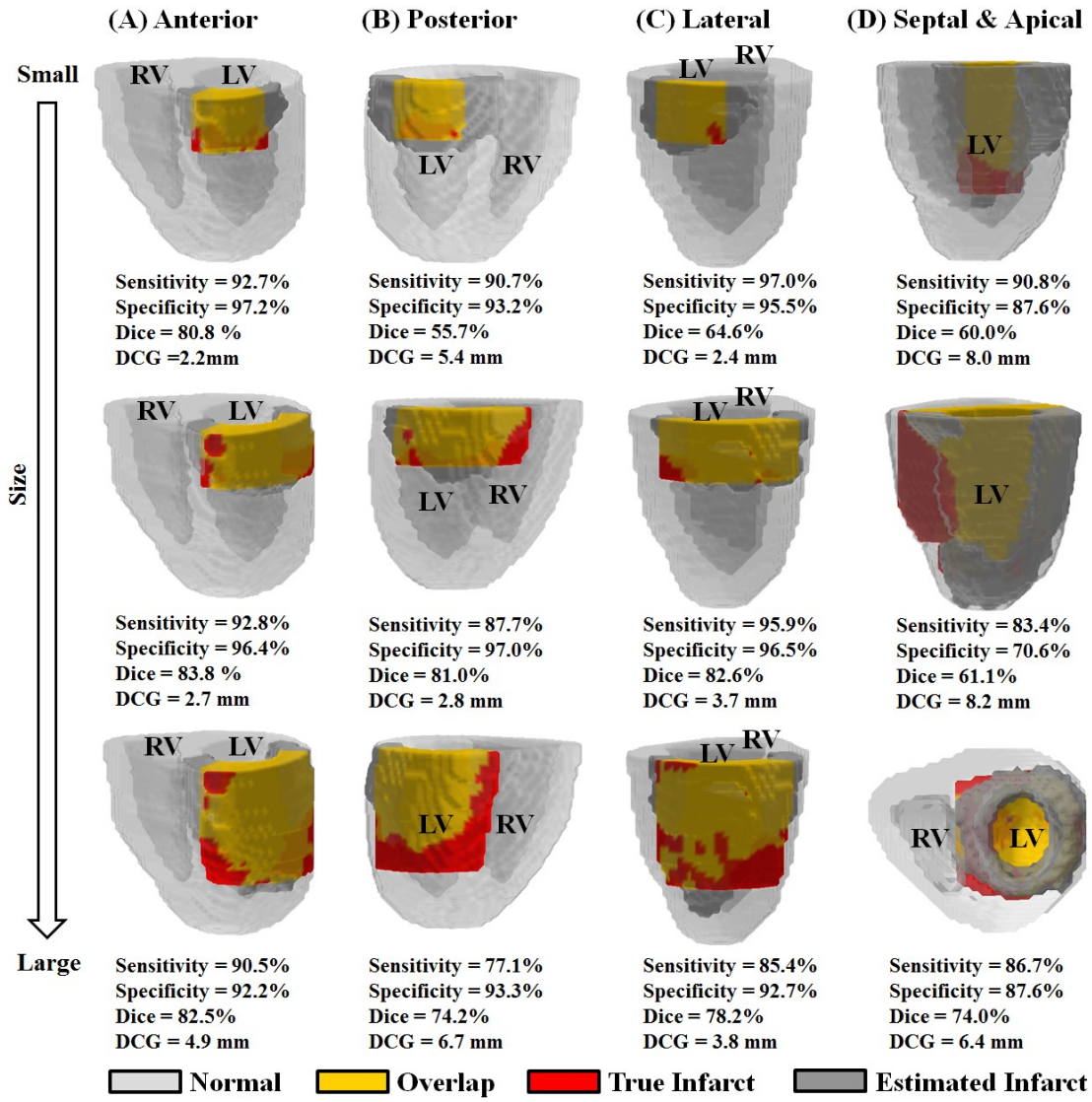

Fig. 3. Overlap between the simulated infarcts and the imaged infarcts with varying sizes and locations. The normal tissue, the overlap between simulated infarction and estimated infarction, the simulated infarction, and the estimated infarction are color coded in transparent silver, yellow, red and gray, respectively. DCG = distance from the center of gravity, LV = left ventricle, RV = right ventricle.

anterior, posterior, lateral, septal, and apical walls of the LV, with various sizes. The simulation was performed with 205 surface electrodes and 10 μV additive GWN. The

normal tissue, simulated true infarction, and the overlap between simulated infarction and imaged infarction, and estimated infarction are shown in transparent silver, solid red, solid yellow, and solid gray, respectively. As shown in Fig. 4, with different sizes and anatomical locations, the imaged MI substrates were in good consistency with the simulated MI substrates. The overall performance was evaluated from 114 simulated transmural MI substrates, and on average, sensitivity was 83.4% ± 16.7%, specificity was 82.2% ± 12.9%, Dice's coefficient was 65.0% ± 12.9%, and DCG was 6.5 ± 3.5 mm, based on a 50% threshold.

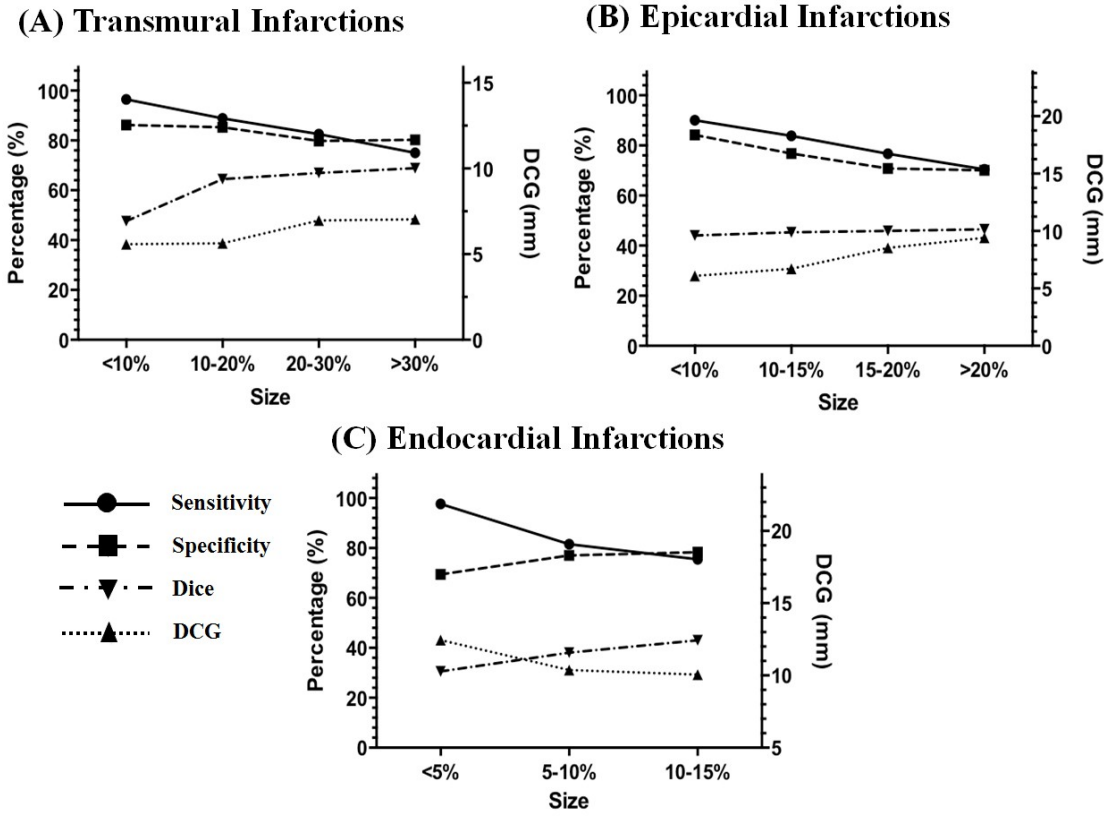

Fig. 4. Performance of the proposed method with varying infarction sizes ranging from 5% to 30% of left ventricle.

Fig. 4(A) compares the effect of the transmural infarction sizes on the inverse

results. In general, smaller infarction size led to higher sensitivity and specificity, lower DCG, but lower Dice's coefficient, suggesting a bigger portion of infarction was accurately identified at the price of over expanded estimation. Specifically, when the size decreased from 30% of the LV volume to 10% of the LV volume, the averaged sensitivity increased from 75.1% to 96.5%, the averaged DCG decreases by 1.5mm, and the averaged Dice's coefficient decreased by 22%. Regardless of the geometrical size, this method was able to identify more than 75% of the infarcted tissue in terms of sensitivity, with a localization error around 7 mm. The result indicated that our method was capable of identifying the dominating infarction substrate with various infarction sizes.

We also investigated the effect of MI locations on the imaging performance. The locations of infarctions have been classified into 5 groups based on their anatomical locations: anterior, lateral, posterior, septal and apical regions. Fig. 5(A) summarizes the results based on the locations of transmural infarctions. On average, the anterior infarctions obtained 11.6% higher sensitivity (86.5% vs. 74.9%) and 1.9 mm lower DCG (6.1 mm vs. 8.2 mm) than posterior infarctions. The lateral infarctions also presented relatively higher accuracy than the septal infarctions in terms of sensitivity (92.3 % vs. 66.6%) and DCG (5.6 mm vs. 6.6 mm). The results of the apical infarction gave an intermediate DCG (7.7 mm) and a much higher sensitivity of 96.7%. The results suggested that our method was feasible to image MI substrates at diversified locations throughout LV.

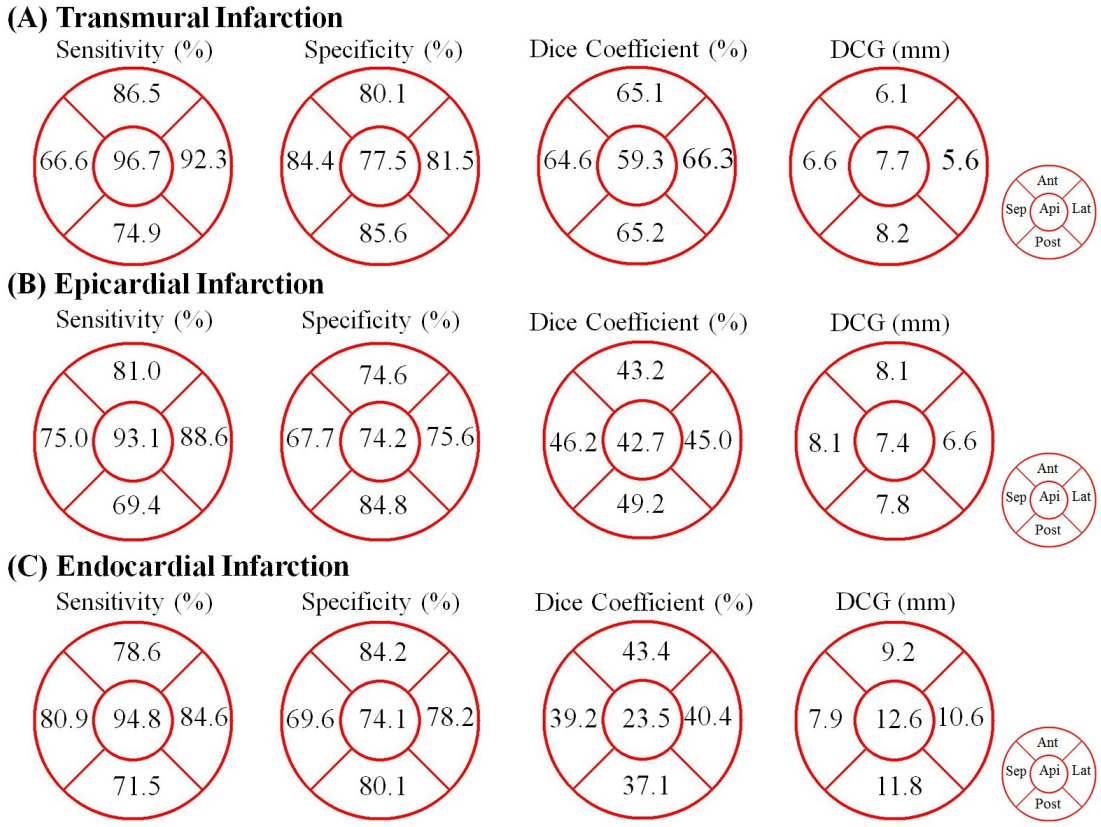

Fig. 5. Performance of the proposed method with varying anatomical locations of infarction. Ant=Anterior, Sep=Septal, Lat=Lateral, Post=Posterior.

3.3.2 Epicardial and Endocardial Infarction

To assess the feasibility of identifying superficial infarctions, we simulated a total of 126 surface infarctions in LV, including 91 epicardial infarctions and 36 endocardial infarctions, assuming 205 surface BSPM electrodes and 10μV GWN. The epicardial infarctions and endocardial infarctions were distinguished by the location of the maximum ECD magnitude. Fig. 6 gives representative examples of imaging epicardial infarctions located at anterolateral LV (Fig. 6(A)), and endocardial infarction located also at anterolateral LV (Fig. 6 (B)). The estimated non-transmural infarctions were closely

consistent with the true infarctions, with a sensitivity of 81.8% and 85.7%, respectively, for these cases. Their positions on the myocardium (epicardial vs. endocardial) were also successfully identified by localizing the spatially maximal ECD (Fig. 6, black asterisks).

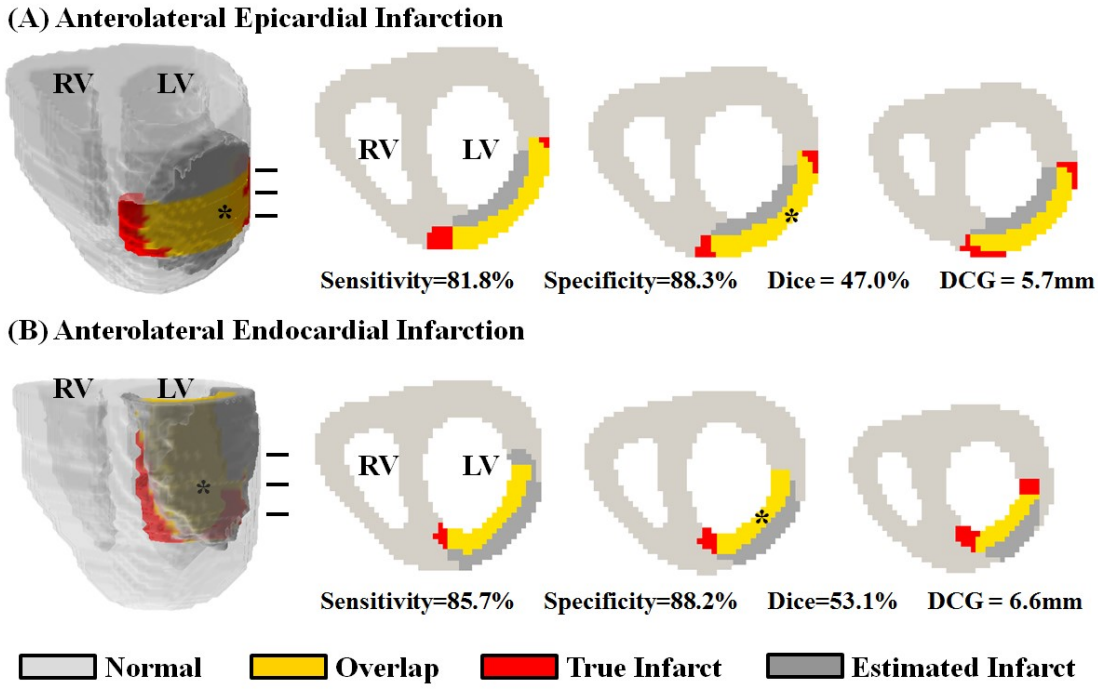

Fig. 6. Selected examples of surface infarctions. (A) Anterolateral epicardial infarct. (B) Anterolateral endocardial infarct. The black asterisks indicate the spatial-maximum ECD localized on epicardium/endocardium. The black lines represent the axial 2-D slices displayed on the right panel.

The average accuracies of 91 epicardial infarctions were 81.6% ± 15.4% for sensitivity, 75.8% ± 15% for specificity, 45.3% ± 7.4% for Dice's coefficient, and 7.5 ± 2.8 mm for DCG. Among the 91 epicardial cases, 65 of them (71%) have been successfully recognized to be epicardial infarctions as the corresponding maximal ECD magnitude locates at the LV epicardium. This method provided a better performance in localizing anterior epicardial infarctions and lateral epicardial infarctions: 80% of the

anterior infarctions and 82% of the lateral infarctions were recognized correctly as on the epicardium. Similar to the transmural infarctions, a smaller size leads to larger sensitivity and specificity, lower DCG, but a slight decrease in Dice's coefficient (Fig. 4(B)). Fig. 4(B) summarizes the results with respect to infarction locations. A better performance was obtained from the anterior and lateral epicardium in terms of sensitivity than the posterior and septal infarctions.

We further investigated in total 36 endocardial infarctions, with an averaged sensitivity of 80.0% ± 15.1%, specificity of 77.0% ± 9.5%, Dice's coefficient of 39.2% ± 5.5%, and DCG of 10.4 ± 2.9 mm. A total of 22 out of the 36 (61%) cases have been successfully identified as endocardial infarctions. Similar to transmural and epicardial infarctions, the sensitivity of endocardial infarctions increased with reducing size at the cost of decreased Dice's coefficient (Fig. 4(C)), and were location-dependent (Fig. 5(C)). Note that the sizes of the endocardial infarctions are much smaller compared to the transmural infarctions. The performance of the proposed method varied when imaging the infarct at different transmural depth. Compared with endocardial infarcts, the epicardial infarcts were estimated with smaller localization error (DCG: 7.5mm vs. 10.4 mm) and slightly higher accuracies (sensitivity: 81.6% vs. 80.0 %). Moreover, non-transmural infarctions were more challenging than the transmural infarctions, which was reflected by generally higher averaged sensitivity and specificity, and lower DCG.

3.3.3 Effects of Noise Level, Electrode Number and Geometry Uncertainty

The effect of the measurement noise was evaluated by adding six different noise levels (0, 5, 10, 15, 20, and 30μV) to 205 channels of BSPM. Fig. 7(A) shows the

sensitivity, specificity, and DCG averaged over 114 transmural infarcts with various noise levels. While a higher noise level led to a slight decrease of sensitivity, specificity and Dice's coefficient, and a slight increase of the DCG, the overall performance of the proposed approach was still robust under different noise levels. As the noise level increases four times from 5 to 20μV, the performance decreased by only 1.4% in terms of sensitivity, 4.9% in terms of specificity, 8.6% in terms of Dice's coefficient, and 2.1 mm in terms of DCG. Even under high noise level of 30 μV, the proposed method can still identify on average over 75.1% of the infarct with averaged DCG of around 10 mm.

We also evaluated the effect of the electrode number on the imaging performance by using 256, 205, 182, 156, and 98 body surface electrodes under 10μV noise from 114 transmural MIs. The electrode arrays were evenly distributed over anterior chest and posterior chest. Fig. 8 illustrates an example of 182 electrodes (11 x 10 on the anterior and 9 x 8 on the posterior). More specifically, there is a 9 x 7 array on the anterior chest and a 7x5 array on the posterior for 98 electrodes; 10 x 10 on the anterior and 8 x 7 on the posterior for 156 electrodes; 12 x 10 on anterior and 11 x 8 on the posterior (with the top 3 electrodes on the back omitted) for 205 electrodes; 13 x 12 array on the anterior and 10 x 10 array on the posterior for 256 electrodes. Fig. 7(B) suggests while high electrode number generally provides better performance, reasonable results were still obtained with a low electrode number. The performance under 98 electrodes was comparable to 205 electrodes, which was supported by the similar obtained sensitivities (81.8% vs. 83.4%), specificities (82.8% vs. 82.2%), Dice's coefficients (61.1% vs. 65.0%) and DCG (7.4 mm vs. 6.5 mm), respectively.

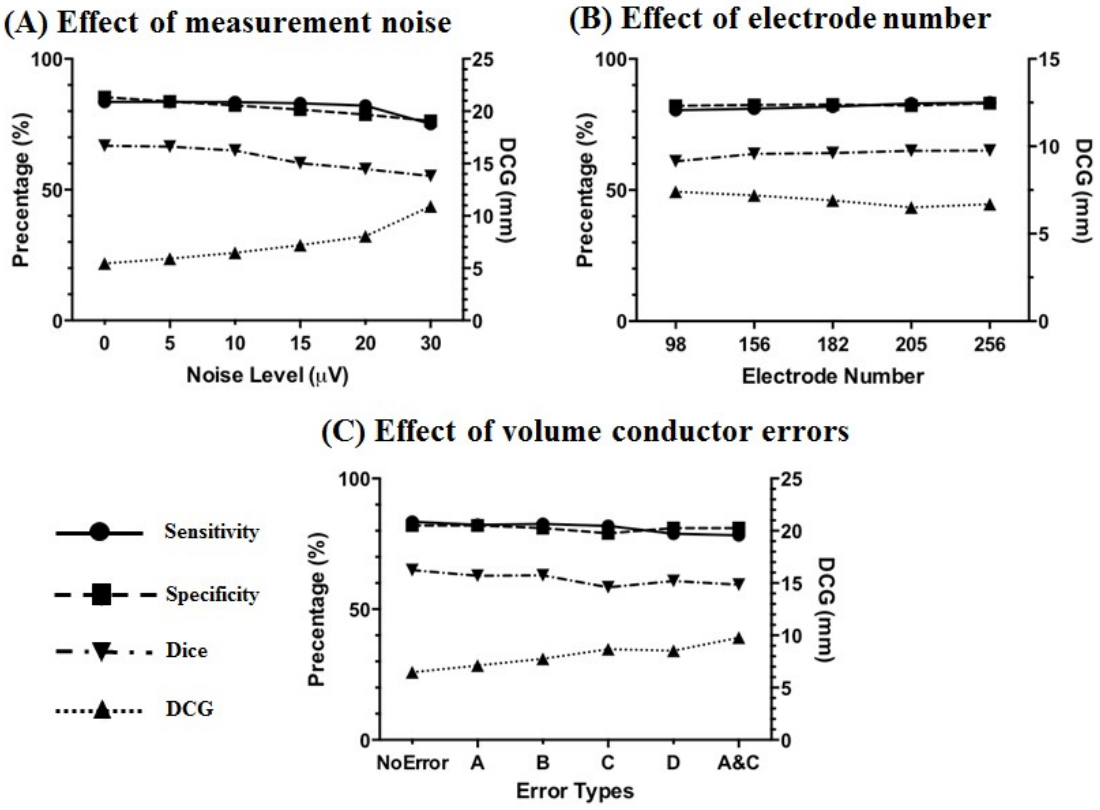

Fig. 7. Sensitivity, specificity, Dice's coefficient, and DCG averaged over 114 cases of infarcts obtained with (A) various levels of additive noise; (B) different numbers of electrodes; (C) six different volume conductor modeling errors. 'No error': without volume conductor modeling error; 'A': heart shifting 4 mm from left to right; 'B': heart shifting 4 mm from front to back; 'C': torso expanded by 10%; 'D': torso reduced by 10%; 'A & C': combination of error A and C.

The effects of the volume conductor modeling errors were further assessed by including torso geometry uncertainty and heart position uncertainty. The heart position was shifted by 4 mm from left to right (error A) or from the front to back (error B), while the torso volume was either expanded (error C) or reduced (error D) by 10%. We also investigated the situation of combining 10% dilation of the torso geometry with 4mm rightward transition of the heart (error A&C). Fig. 7(C) shows that our method still possessed reasonable robustness against abovementioned modeling errors. And even in

the worst case, with the existence of both geometry error and heart position shifting (error A&C), this method still obtained a reasonable sensitivity of 78.3%, a specificity of 80.8%, a Dice's coefficient of 59.4%, and DCG of 9.8 mm, averaging over 114 transmural infarcts.

3.4 Discussion

In the present study, we have developed a new method for noninvasive imaging of the MI substrates based on physically modeling the cardiac electrical sources using the ECD distribution throughout the ventricular myocardium during the S-T segment. Comprehensive computer simulation studies were performed by simulating a number of transmural infarctions, epicardial infarctions and endocardial infarctions. The simulation results indicated that: 1) under 10μV GWN, the transmural infarction can be identified with an average sensitivity of 83.4%, specificity of 82.2%, Dice's coefficient of 65.0%, and DCG of 6.5 mm over 114 cases, respectively; 2) the present method can reasonably provide information with respect to the substrate depth (epicardium vs endocardium); 3) A reasonably good imaging performance can still be obtained under various noise levels, fewer BSPM electrodes, and mild volume conductor modeling errors, respectively.

The present simulation study provides a quantitative and comprehensive evaluation on the performance of the proposed method by simulating a number of transmural and non-transmural MI with various sizes and locations. Although not tested using experimental data, the computer simulation results suggest the potential clinical applicability of the present method to noninvasively identify the MI substrate throughout

the 3D myocardium within one cardiac cycle. The identification of the MI substrate and its border zone may have a great clinical interest due to the role of border zone in initiating the life-threatening cardiac arrhythmias. Compared with other clinical imaging modalities, the sequential mapping technique defines MI substrate in an electrophysiological way, but is only able to give 2-dimensional surface representation instead of volumetric geometry (Volkmer et al. 2006). By contrast, the proposed method suggests the potential to provide 3D volumetric information of MI substrate and further delineates the geometry of border zone instead of being limited to the endocardial surface. Compared with conventional ECG recording, the method is able to provide a direct visualization on the location and geometry of MI substrate. In the present study, the simulation results show that this proposed method is able to localize the surface location in 71% epicardial infarctions and in 61% endocardial infarctions, and thus suggests the potential to differentiate between epicardial and endocardial infarctions and to provide assistive information to ablation procedures in the clinical condition. While imaging non-transmural infarctions possessed more challenges than imaging transmural infarctions, the present method still achieved a reasonable performance for the epicardial infarction (sensitivity = 81.6%, specificity = 75. 8%, Dice's coefficient = 45.3%, and DCG = 7.5mm) and endocardial infarction (sensitivity = 80.0%, specificity = 77.0%, Dice's coefficient = 39.2%, and DCG = 10.4 mm). Such results suggest that the ECD-based method may have the potential to noninvasively and quantitatively estimate non-transmural infarctions and provide information on source depth.

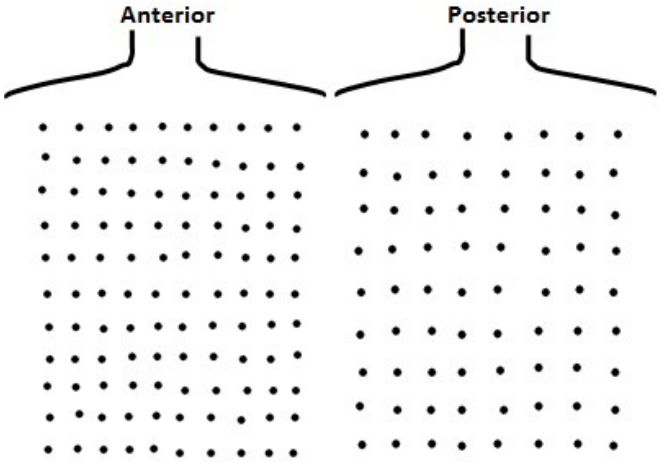

Fig. 8. The electrode arrays in the case of 182 electrodes.

The purpose of the present study is to develop and evaluate an ECD-based approach for quantifying the MI substrates in the heart. A few simplified assumptions have been used in computer simulation while the reliability of model validation has been retained. We have assumed a constant zero for the potential at the simulated substrate, while in reality a relative complex action potential featured by a low amplitude as compared with normal tissue would be expected. The assumption on action potential has simplified the computer simulation while retained the feature of potential gradient at the border zone at plateau phase.

We have used realistic geometry volume conductor model and piece-wise homogeneous boundary element model (BEM) in the simulation process. The BEM model was consisted of torso, lungs, heart muscle, the LV and RV blood cavities, with conductivity values of 0.21 s/m, 0.05 s/m, 0.21 s/m, and 0.67 s/m, respectively. Considering that in the volume conductor model, the infarction area has a conductivity of 0 s/m so it may affect the forward computation of BSPM if this is not taken into account.

To address the issue, we simulated the situations that MI regions are having zero electrical conductivity with the aid of the finite element method (FEM). Specifically, in additional to the similar setting above, for infarction area, the electrical conductivity was chosen to be zero in the FEM model. We have also simulated infarctions with 1.5 mm-thick ischemic border zone as well. The electrical conductivity of the border zone in the FEM model was chosen to be 1/10 of the normal tissue in the longitudinal direction and 1/1000 in the transverse direction. We used such FEM-generated BSPM and estimated MI with BEM based inverse procedure in two infarction cases: anterior infarction and lateral infarction. The anterior infarction was imaged with a sensitivity of 90.1%, specificity of 91.3%, Dice's coefficient of 71.2%, and DCG of 3.5 mm. The anterior infarction with ischemia was imaged with a sensitivity of 91.2%, specificity of 90.5%, Dice of 70.3%, and DCG of 3.8 mm. The imaging result is comparable to the result obtained with BEM-generated BSPM and BEM based inverse procedure (Sensitivity=92.7%, specificity = 97.2%, Dice's coefficient = 80.8%, DCG =2.2 mm). The lateral infarction was estimated with a sensitivity of 93.1%, specificity of 91.8%, Dice's coefficient of 60.3%, and DCG of 3.4 mm. The lateral infarction with ischemia was imaged with a sensitivity of 92.6%, specificity of 90.3%, Dice of 57.6%, and DCG of 3.2mm. The imaging result of FEM-generated lateral infarction is also comparable to the result obtained with BEM-generated BSPM (sensitivity = 97.0%, specificity – 95.5%, Dice = 64.6%, and DCG = 2.4mm). These results suggest that ignoring the electrical conductivity value in our computer simulations does not significantly impact the simulation results. This also suggests that simulating MI substrate using zero action

potential may provide a reasonable approximation.

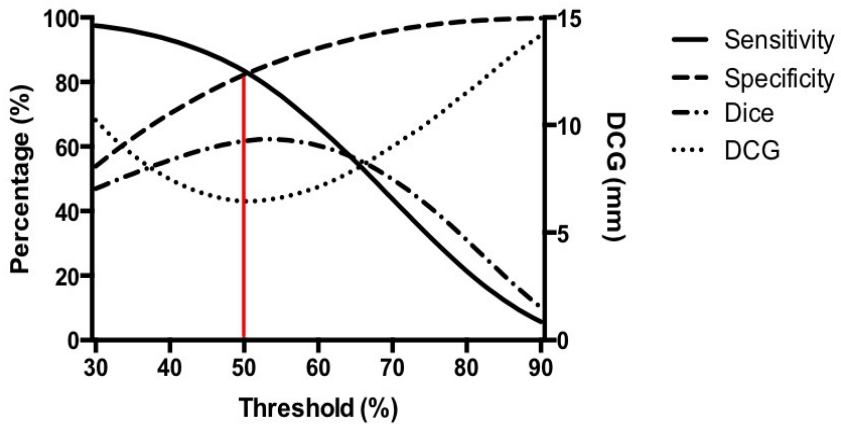

Fig. 9. Selection of the threshold. The x axis represents different thresholds which were used to quantify the MI volume; the y axis represents the mean sensitivity, specificity, Dice coefficient and DCG obtained from 114 cases of infarctions based on the corresponding threshold from x axis

In the present study, the selection of threshold would affect the volume of estimated infarction. We have chosen a 50% threshold to quantify the MI substrate and corresponding computer simulations were performed to evaluate the selection of threshold. For 114 cases of transmural infarction, the MI substrates have been quantified with different thresholds ranging from 30% to 90%. And the corresponding mean sensitivity, specificity, Dice's coefficient, and DCG achieved with different thresholds were computed and illustrated in Fig. 9. The simulation outcome suggests that the 50% threshold is an appropriate choice at which the method would achieve reasonably good performance in terms of the four parameters.

3.5 Conclusions

In conclusion, we have proposed a novel method for noninvasive imaging of the myocardial infarction substrate throughout the 3D myocardium using the equivalent current density model. The comprehensive computer simulation results suggest that the proposed method may have the potential to non-invasively estimate transmural and surface infarction, and to provide information with respect to epicardial infarction and endocardial infarction.

Chapter 4

Noninvasive Imaging of Drivers of Atrial Fibrillation

4.1 Introduction

The mechanism of atrial fibrillation (AF) is complex and not yet fully understood. Contemporary studies suggested that disorganized electrical activation during AF might be maintained by drivers with exceedingly high activation rate, namely the highest dominant frequency (DF) (Sanders et al. 2005, Lazar et al. 2004, Skanes et al. 1998). Ablation of such drivers with successful elimination of the bi-atrial frequency gradient predicts long-term freedom of fibrillation (Atienza et al. 2009). Therefore, it is postulated that the high-frequency drivers are effective targets for AF ablation. The locations of the highest-DF drivers can be found in both atria in patients with persistent and non-pulmonary-vein-foci paroxysmal AF. However, intracardiac mapping has limitations in identifying the locations due to the challenge of generating precise spatial-temporal maps within limited procedure time. Therefore an alternative noninvasive technique to reconstruct atrial DF maps is needed for treatment individualization.

Noninvasive cardiac electrical source imaging techniques reconstruct cardiac electrical activities based upon body surface ECGs and patient's heart-torso geometry (Greensite & Huiskamp 1998, He & Wu 2001, He et al. 2003, He et al. 2002, Ohyu et al. 2002, Liu et al. 2006, Liu et al. 2008, Han et al. 2008, Wang et al. 2011, Han et al. 2011, Han et al. 2012, Han et al. 2013, Armoundas et al. 2003, Li & He 2001, Wang et al. 2010, Wang et al. 2013). Unlike BSPMs which present a spatial summation of overall cardiac

electrical activities on the torso, cardiac electrical imaging reconstructs myocardial activation by mapping BSPM onto the source domain - the heart, thus allowing direct interpretation on cardiac activities. In previous studies, the cardiac electric imaging technique has been mainly utilized to image atrial activations with a focal-onset or a macro-reentry mechanism, such as atrial tachycardia and atrial flutter, by using either the heart surface method (Tilg et al. 2001, Tilg et al. 2003, Seger et al. 2006) or the epicardial potential method (Ramanathan et al. 2004, Ramanathan et al. 2006, Wang et al. 2007a, Roten et al. 2012, Shah et al. 2013, Cakulev et al. 2013). Most recently, the electrical activities during AF have also been investigated using the epicardial potential approach. Based on the epicardial potentials that are reconstructed from the inverse solution of electrocardiography, the activation time and the phases of wave-propagation can be extracted to study the complexity of activation patterns and rotor activities (Cuculich et al. 2010, Haissaguerre et al. 2014, Rudy 2013, Haissaguerre et al. 2013). However, those studies did not examine whether frequency domain features can be noninvasively imaged from BSPMs. In the present study, we have proposed a frequency-based noninvasive cardiac electrical imaging approach, which integrates spectral analysis with source imaging to reconstruct DF maps during AF. The goal of the study is to evaluate whether CEI is capable of identifying highest-DF drivers and recovering frequency features in AF patients.

This chapter has been published at IEEE Transactions on Biomedical Engineering (Zhou et al. 2016a).

4.2 Materials and Methods

4.2.1 Study populations

BSPMs were measured on 13 patients (Female=8, Male=5, averaged age = 58.5 ± 9.3) with paroxysmal AF and persistent AF. Subjects' clinical characteristics are summarized in Table 1. Among the 13, a total of 7 of them underwent spontaneous AF and the AF episodes during BSPM recordings and were analyzed by using the CEI method. All protocols were approved by the Institutional Review Board (IRB) of the Shanghai Ruijin Hospital (affiliated with Shanghai Jiao Tong University School of Medicine, Shanghai, China) and the IRB of the University of Minnesota. Data collection was performed after the signed informed consents were obtained from patients. Fig. 10 shows the schematic diagram of the study.

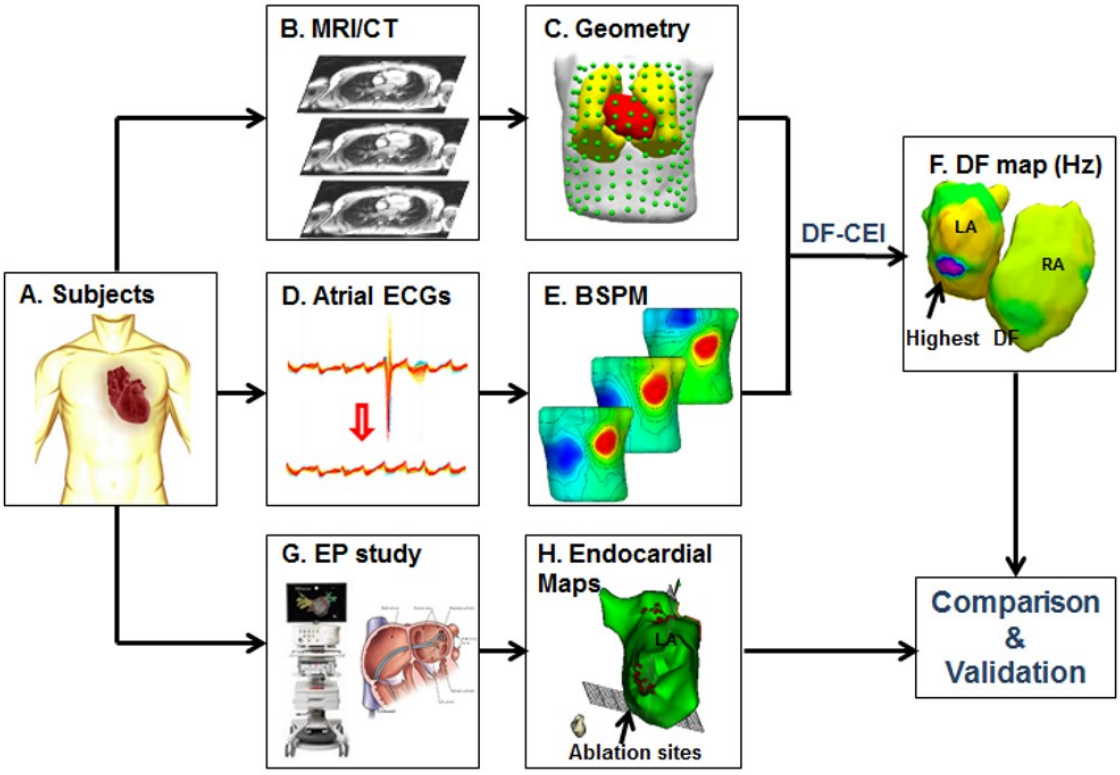

Fig. 10. Schematic diagram of the frequency based cardiac electric imaging and validation in patients with atrial fibrillation.

4.2.2 Body surface potential mapping

The BSPMs were recorded when patients were at resting state (supine position with smooth breath). Before the BPSM recording session, a total of 208 channels of Ag-AgCl carbon electrodes (BioSemi Active-Two) were placed on the anterior-lateral chest (n=144) and the posterior trunk (n=64). The electrodes were connected to BioSemi

TABLE 1
PATIENT CHARACTERISTICS AND MEDICAL HISTORIES

	Age	Gender	Diagnosis	Previous Ablation	Blood Pressure	Rhythm	Antiarrhythmic Medication	Medical History*	Atrial Size
1	59	M	Persistent	None	123/74	AF	Metoprolol Warfarin Valsartan Amlodipine	Hypertension, Tricuspid Regurgitation	LA Enlargement
2	60	M	Persistent	None	149/94	AF	Metoprolol Digoxin	Hypertension, Mitral Regurgitation	LA Enlargement
3	59	F	Persistent	None	116/84	AF	Bisoprolol Warfarin	Mitral Regurgitation, Tricuspid Regurgitation	LA Enlargement
4	62	M	Persistent	1	129/102	AF	Bisoprolol Fumarate	Hyperlipemia, Tricuspid regurgitation	RA Enlargement
5	60	M	Paroxysmal	1	103/62	AF	Warfarin Flecainide Diltiazem	Hyperlipemia, Mitral Regurgitation	Normal
6	64	F	Paroxysmal	1	90/52	AF	Wafarin, Dronedarone	Hypertension, Tricuspid Regurgitation, Mitral valve Disorders, Congestive Heart Failure	Normal
7	38	F	Paroxysmal	1	91/58	AF	Wafarin Lisiopril Metoprolol	Restrictive Cardiomyopathy Hypertention	LA Enlargement
8	45	F	Paroxysmal PAC	None	120/71	Sinus	None	N/A	Normal
9	55	F	Paroxysmal	None	130/80	Sinus	Aspirin	Diabetes	LA Enlargement
10	56	F	Paroxysmal	None	137/76	Sinus	Metoprolol	N/A	Normal
11	68	F	Paroxysmal PAC	None	150/90	Sinus	Aspirin, Clopidogrel	Hypertension	LA and RA Enlargement
12	70	M	Paroxysmal	None	101/48	Sinus	Wafarin	Mitral Regurgitation	Normal
13	65	F	Paroxysmal AFL	None	126/65	Sinus	Cordarone	N/A	Normal

*Selective cardiovascular related medical history; F = female, M=male, BSPM=body surface potential map, PAC=premature atrial contraction, AFL=atrial flutter.

Active-Two measurement system with a sampling rate of 2048 Hz (with 400 Hz cut off frequency of low pass filter) and a 24 bit analog-to-digital converter. During the BSPM recording, patients were told to keep still with slow respiration in order to minimize baseline wandering and motion artifacts. After the BSPM measurement, the locations of electrodes were recorded by using a radio frequency digitizer (Fastrak, Polhemus Inc., Vermont).

4.2.3 Anatomical data acquisition

Computer Tomography (CT) was performed on each subject to obtain subject-specific heart-torso geometry. The heart geometries were obtained by continuous volume scanning from the great vessel level down to the diaphragm with intravenous (IV) contrast. The slice thickness was 0.4 mm and was fine enough for the segmentation of a refined heart model. Additional torso scans were performed with a slice thickness of 6 mm from the level of collar bone down to the lower abdomen, and were used to build a complete torso model. The in-plane resolution of the CT scan was fixed at 512 x 512 pixels. In order to avoid respiratory artifact, patients were alerted before the scanning to hold respirations. Continuous ECG was monitored and used for gating the CT scanner. The CT images were further processed by commercial software (Curry 6.0, Neuroscan, North Carolina) to obtain the individual heart-torso geometry. The heart and torso CT images were coupled based on important cardiac anatomical landmarks, such as the apex, and the co-registration errors were minimized with the assistance of Curry 6.0. Detailed anatomy structures including the atria, the ventricles, the lung and the torso were segmented. For the segmentation of the atria, important anatomical structures, like the pulmonary veins (PV), superior vena cava (SVC), inferior vena cava (IVC), tricuspid annulus (TA) and mitral annulus (MA), were identified and marked.

4.2.4 Signal processing

BSPMs were grounded with Wilson center terminal (WCT) and filtered with either 50-Hz or 60-Hz second-order infinite impulse response notch filter to remove the utility frequency component. BSPMs contained ventricular signals which would affect the atrial

DF reconstruction, hence a classic and validated QRS-T template subtraction technique was applied to remove ventricular activities (Xi et al. 2003). As ventricular components are independent from the atrial activities during AF (Rieta et al. 2004), the Independent Component Analysis was further utilized following the template subtraction to remove any presented QRS residuals in Curry 6.0. BSPMs were then further low-pass filtered by a 10th order Butterworth filter with a cut-off frequency of 40 Hz.

4.2.5 Equivalent current density modeling

Based on the bi-domain theory, for a given point r in the myocardium, the equivalent cardiac source $\vec{j}_{eq}(r,t)$ representing the cardiac electrical activities can be derived as

$$\vec{j}_{eq}(r,t) = -\sigma_i(r)\nabla\phi_m(r,t) \tag{4.1}$$

where $\sigma_i(r)$ is the intracellular conductivity tensor, and $\phi_m(r,t)$ is the transmembrane potential (TMP) at location r and time t. Equation (4.1) defines $\vec{j}_{eq}(r,t)$ to be proportional to the spatial gradient of TMP. The depolarization phase of action potential is featured by an instantaneous rise from the resting potential to the plateau phase. The propagation of cardiac activation wavefront separates the myocardium into depolarized region and non-depolarized regions.

Note that the widely-used intracardiac mapping technique using bipolar electrograms (EGM), is approximately a directional component of the spatial gradient of TMP (Han et al. 2008) . The relationship between $\vec{j}_{eq}(r,t)$ and $\nabla\phi_m(r,t)$ in equation (4.1) tells that, similarly, the bipolar EGM can also be considered as a directional component

of the local current density $\vec{j}_{eq}(r,t)$, that is, $|\vec{j}_{eq}(r,t)|$ provides an alternative and equivalent feature as bipolar EGMs for deriving the local activation rates.

4.2.6 Frequency analysis of cardiac sources

Clinical EP studies based on bipolar EGMs reported that the AF drivers with the highest DF served as potential ablation targets for AF treatment. As discussed above, local current density provides equally effective characteristics as the bipolar EGMs for frequency analysis, which enable us to implement the concept of DF into noninvasive cardiac source imaging technique.

Considering the local current density $|\vec{j}_{eq}(r,t)|$ at myocardium point r, which are sampled into T discrete samples j_n, n=0,1, 2,...,T-1. The local excitation frequency can be determined by using Discrete Fourier transform (DFT) to transform j_n from time domain to Jeq(k) in the frequency domain:

$$Jeq(k) = \sum_{n=0}^{T-1} j_n e^{-i2\pi kn/T} \tag{4.2}$$

where T is the number of samples, n is the current sample being considered, k is the index of frequency. The actual frequencies of periodic sequences depend on the sampling rate f_s and can be expressed by $f = f_s k / T$. The DF of atrial electrical activities for a given location r is corresponding to the frequency at which the power spectrum reaches maximal amplitude:

$$DF(r) = \frac{f_s}{T} \underset{k}{\operatorname{argmax}}\left(\frac{|Jeq(k)|^2}{T}\right) \tag{4.3}$$

The time to frequency domain transform of cardiac sources allows us to investigate the

spectral features of AF and identify high-frequency drivers for catheter ablation in a noninvasive way.

4.2.7 Forward and inverse solutions

The CEI technique was previously used to reconstruct 3-D ventricular cardiac activation patterns from BSPM, and has been validated with animal studies (Liu et al. 2006, Han et al. 2008, Han et al. 2011, Han et al. 2012, Han et al. 2013). The method for forward and inverse computation is presented in the previous chapters. However, in the present study, the application of CEI was extended to image atrial electrical activity. Similarly, the cardiac sources are presented by distributed equivalent current density. However, it's needed to noted that, given the thin nature of atrial wall, the equivalent cardiac electrical sources were assumed to distributed over the endocardium of the LA and RA.

4.2.8 Data Analysis

In the present study, a 2-dimensional (2-D) atrial surface source model was used to equivalently represent atrial electrical activity, ignoring the thickness of atria. The LA and RA were discretized into 2282 ± 576 grid points with a spatial resolution of 3mm. The 2-D atrial ECD distributions were then reconstructed by coupling the BSPM with boundary element model (BEM) obtained from patient-specific heart-torso geometry (Liu et al. 2006, Han et al. 2008, Han et al. 2011, Han et al. 2012, Han et al. 2013). In order to image AF drivers exciting at relatively stable high frequency, a fixed 5-seconds length of BSPMs was used for analysis to ensure the capture of reliable high-frequency source.

Following ECD reconstruction, the ECD were then tapered with Hanning window

to set the edge value to zero, and processed with a 3 Hz – 15 Hz band-pass filter. The ECD of 5 seconds was then zero-padded to 20 seconds in order to obtain higher spectral resolutions. FFT was then performed on the ECD at each given atrial location using the commercial MATLAB package (MATLB R2012b, Mathworks, Massachusetts). The bi-atrial DF map was computed from the frequency corresponding to the highest peak in the power spectrum. The regularity index (RI) was defined as the ratio of the power at the DF and its neighboring 0.75 Hz frequency band to the power of the 3-15 Hz band (Sanders et al. 2005), and was used here to guarantee the reliability of the reconstructed DF. Only points with RI>0.2 were selected in the reconstruction of DF map. The maximal DF site was defined as the highest DF surrounded by a ≥20% decreasing frequency gradient.

4.2.9 BPSM DF maps

CEI reconstructs the spatial distribution of atrial electrical activities at each time instant, from the potential map on the torso at the corresponding time point. It is necessary to evaluate whether it can also reliably recover the frequency features in the atria based on what is spatially observed from BSPM. Therefore, the DF distribution on the torso was computed by performing the same FFT analysis procedure on the BSPM and compared with the reconstructed atrial DF map. After removal of ventricular components, the surface ECGs were tapered with Hanning window and filtered by 3 Hz – 15 Hz band-pass filter. The BSPM DF map was then computed by applying FFT analysis to 5-second surface ECGs and selecting the frequency with highest peak in the power spectrum.

4.2.10 Statistical Analysis

To further investigate the dispersion and coherence of the results, statistical analysis was applied to compare the variability of frequency features in different groups of patients. Paired student's t test was applied in the comparison for maximal DFs in RA and LA within each group (paroxysmal group vs. persistent group) in order to evaluate the LA-to-RA frequency difference. The result was considered to be statistically significant when the p-value was found to be <0.05. Repeating variables, like the maximal DFs observed in patients from different time intervals, were reported in the form of mean ± standard deviation (SD).

4.3 Results

A total of 7 patients had spontaneous AF during BSPM recording (n=3 for paroxysmal patients, n=4 for persistent patients) and were analyzed by using the CEI technique. In paroxysmal AF patients, atrial enlargements were found in one of the three analyzed patients. All persistent AF patients had atrial enlargements (LA=3, RA=1), which might indicate more risks of structural heart disease. Patients without spontaneous AF were recorded with sinus rhythm and therefore no high-frequency drivers could be observed.

Fig. 11 shows successive DF maps obtained from a 60-year old male paroxysmal AF patient. The patient had AF recurrence 22 months after the first ablation procedure. Spontaneous AF was recorded one day prior to the second procedure. On this patient, CEI repeatedly showed: (1) focal maximal DF sites at the inferior of the right inferior PV

(RIPV), the superior area of the left superior PV (LSPV), and the LA roof; and (2) a persistent LA-to-RA frequency gradient (maximal DFs in LA vs. maximal DFs in RA: 7.2 ± 0.4 vs. 6.6 ± 0.2, $p<0.05$). CEI was able to image the persistent maintenance as well as transition of maximal DF sites over time. At time window A, the maximal DF sites were observed at superior LSPV (7.4Hz) and LA roof (7.4 Hz) (Fig. 11A). Later on, the maximal DF at superior LSPV persists (7.8 Hz) while the high frequency activity at roof LA vanishes, and the inferior RIPV begins to activate as the secondary highest DF site (7.4 Hz) (Fig. 11B). In the following time window C, the superior LA completely degenerates into low frequency activity, and the RIPV inferior takes the role of dominant driver (6.8Hz). Note that the temporal transition of highest DF sites appeared to be spatially stable, namely highest DF sites were only found in certain locations. The time window for observation was shown by lead V1, each with a fixed 5-second interval. A sustaining LA-to-RA frequency gradient was observed over time regardless of the change of the maximal DF sites. The imaged maximal DF site corresponded well with the ablation sites (Fig.11, red balls, superior LSPV, LA roof and the inferior of RIPV), and the variation of the highest DF was confined to the sites of ablation.

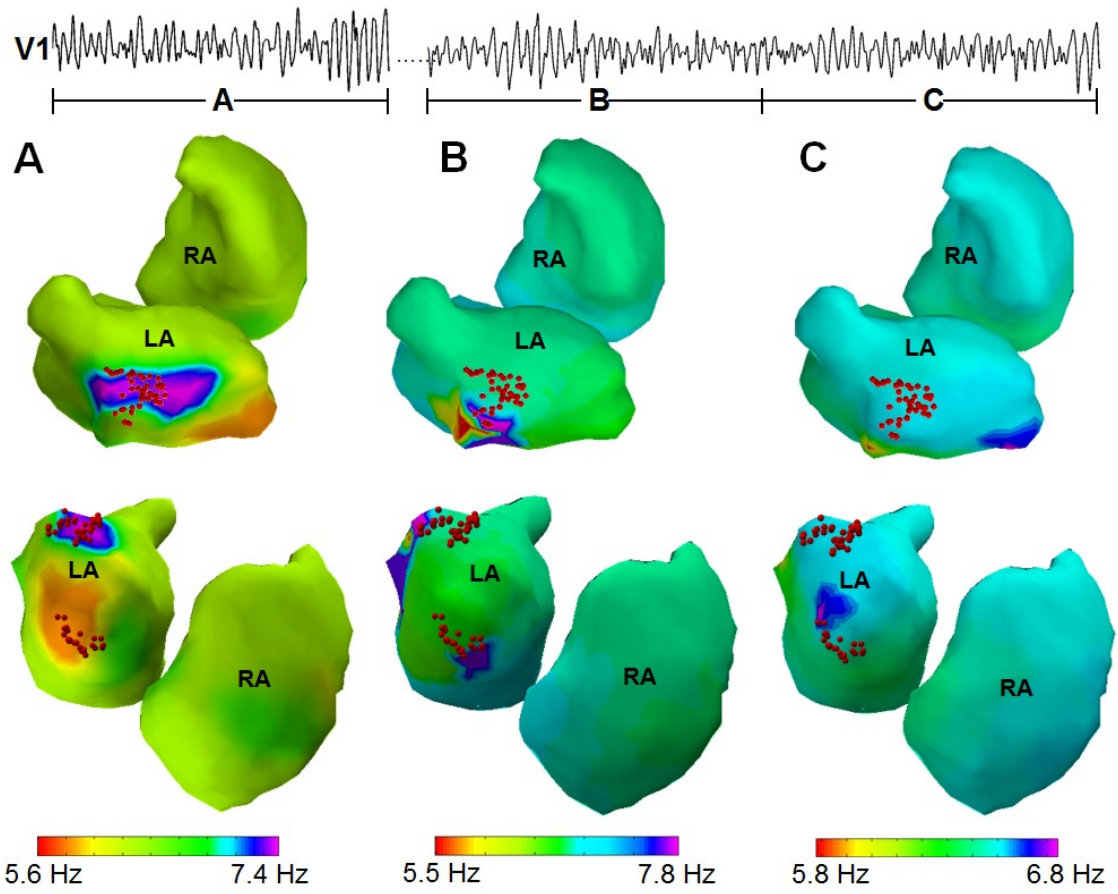

Fig. 11. (A)-(C) Imaged DF maps from a selected paroxysmal AF patient. The corresponding BSPM time frames A-C were shown in lead V1 in the upper panel. The dark red balls show the ablation points in CARTO record. The DF value is color coded from red (low frequency) to purple (high frequency).

Fig. 12 shows the examples of DF maps reconstructed from a 59-year old patient with persistent AF, the time windows for imaging were shown by ECG lead V1. In a sequential time series, CEI repeatedly found: (1) Maximal DF sites localized at the left inferior PV (LIPV), RIPV, right superior PV (RSPV) and right atrial appendage (RAA); (2) the absence of significant hierarchical LA-to-RA DF gradient and a spatial disorganization of frequency distribution; (3) a bi-atrial dispersion of high-frequency

activities as compared with the paroxysmal patient; and (4) the maximal DF sites migrated over time yet were restricted in a confined region and can be repeatedly imaged from independent AF segments. The results show stationary maintenance, dynamic transition, and spatial repetition of maximal DF sites over time: a sustaining maximal DF was observed to be harboring at the RAA over time (the lower panels of Fig. 12 A-D), the maximal DF located at LIPV was stable during time window A-B (purple area in white dotted line, the upper panels of Fig. 12 A-B), yet degenerated at time window C, and RSPV and RIPV have become the sites with maximal DF (Fig 12 C and D). This patient underwent circumferential pulmonary isolation (CPVI) and AF re-occurred at day 2 after ablation. The un-ablated persistent highest DF site at RAA might possibly associate with the remaining drivers leading to the recurrence of AF episode.

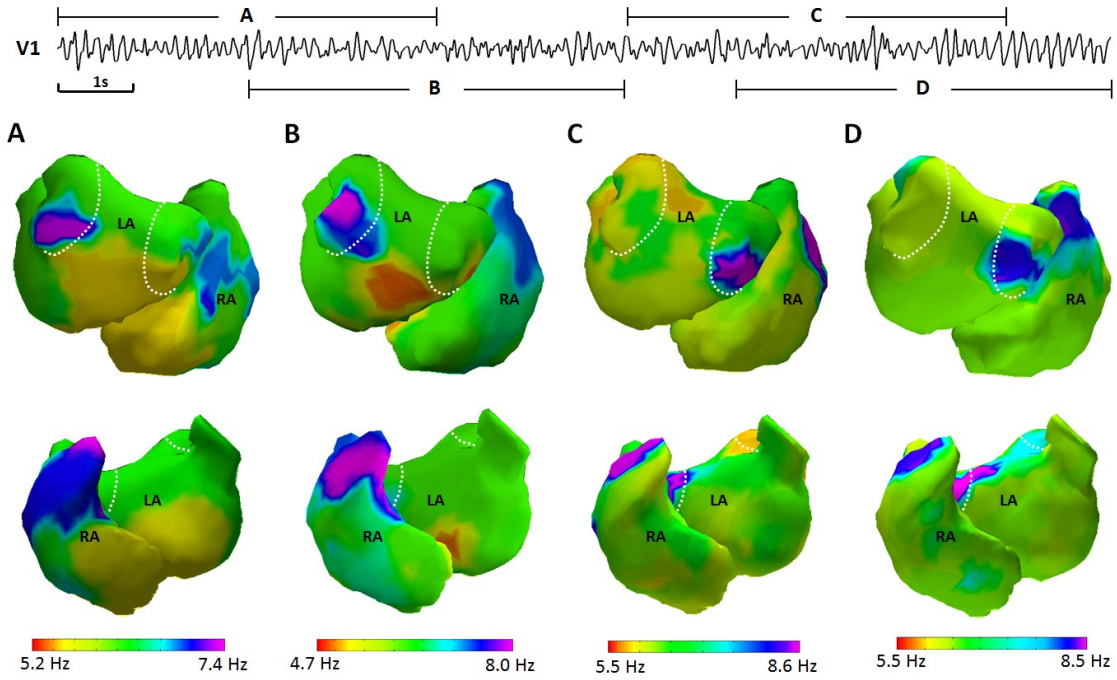

Fig. 12. Imaged DF maps in one persistent AF patient. Lead V1 on the upper panel shows the time frames which were used for the DF reconstruction. Figure (A) - (D): the DF maps obtained from time frame A - D with a fixed length of 5 seconds in lead V1, respectively. The dotted white line indicates the ablation zone to isolate the electrical activities from the pulmonary vein area.

The highest DF sites found in all patients were summarized and compared with ablation sites in Table 2. AF drivers were also found around PVs in the other 2 paroxysmal patients who underwent circumferential PV isolation (7.48 ± 0.8 Hz). In all paroxysmal patients, a significant left-to-right frequency gradient was found (7.42 ± 0.66 Hz vs. 5.85 ± 1.2 Hz, LA vs. RA, $p<0.05$). The imaged drivers were consistent with ablation sites in paroxysmal AF patients. All persistent AF patients underwent circumferential PV isolation, but AF was not terminated by ablation (Table 2). High frequency drivers were identified in all persistent AF patients. In three out of the four persistent AF patients, non-PV drivers were found at LAA and RAA, suggesting the

existence of un-ablated sources likely to maintain AF. Compared with paroxysmal AF, a loss in LA-to-RA frequency order was observed from persistent AF patients (8.09±1.06 Hz vs. 7.6 ± 1.03 Hz, LA vs. RA, p=0.2).

TABLE 2
HIGHEST-DF SITES FOUND ON PATIENTS BY USING THE CEI TECHNIQUE IN COMPARISON WITH PATIENTS' CLINICAL OUTCOME.

#	AF Type	Locations of Highest DF	Ablation	Other Procedure	Un-ablated DF Sites*	Termination after Ablation
1	ParoAF	LSPV LA Roof Inferior RIPV	LSPV LA Roof Inferior RIPV	N/A	None	Y
2	ParoAF	LSPV LIPV RIPV	CPVI	N/A	None	Y
3	ParoAF	LIPV	N/A	MAZE	N/A	N/A
4	PerAF	LIPV RIPV RSPV RAA	CPVI	N/A	RAA	N
5	PerAF	LIPV LSPV RIPV RAA	CPVI	N/A	RAA	N
6	PerAF	RSPV LSPV	CPVI	N/A	None	N
7	PerAF	LSPV LAA	CPVI	N/A	LAA	N

*Atrial sites found with highest DF but were not ablated in radiofrequency ablation; CPVI = Circumferential pulmonary vein isolation; LSPV = Left superior pulmonary vein; LIPV = Left inferior pulmonary vein; RSPV = Right superior pulmonary vein, RIPV = Right inferior pulmonary vein; Y = Yes; N = No; N/A = Not applicable; ParoAF=Paroxysmal AF; PerAF=Persistent AF.

We also evaluated the correlation between the body surface DFs and the imaged atrial DF. Figure 13 shows the DF map on the torso determined from 5-s BSPM in figure 12C. The body surface DF map shows similar frequency ranges with the imaged atrial

DF map. Highest DF sites on the torso were located at right anterior chest and medial to right posterior trunk, which were the projections of highest intracardial DF from RAA and left pulmonary veins. The mean DF was 6.4 Hz for body surface and 6.5 Hz for the atrium.

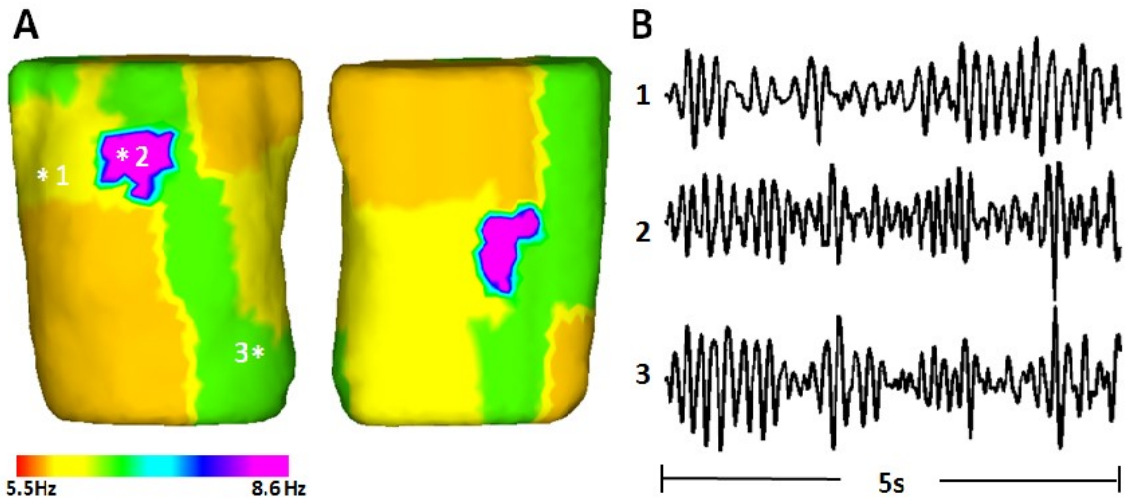

Fig. 13. (A) The DF distribution on the torso corresponding to the 5-s BSPM in figure 12C. (B) The signals on surface leads.

4.4 Discussions

We report for the first time an investigation of imaging the spectral characteristics of AF from BSPM in a group of patients by integrating the cardiac electric imaging with clinical dominant frequency (DF) concept. The frequency-based CEI technique is capable of imaging the spatiotemporal behavior of DF and pinpointing the drivers with highest activation frequency during AF. On paroxysmal AF patients, the hierarchical spectral patterns featured by LA-to-RA maximal frequency gradient were observed. In persistent AF patients, the DF behavior was characterized by the loss of the hierarchical pattern and

the dispersion of AF drivers in both atriums. Although the DF maps were reported previously from intracardiac recordings, our results indicate, for the first time, that similar findings can be obtained noninvasively from the frequency-based CEI. For patients with both paroxysmal and persistent AF, the CEI captured the temporal dynamic transition as well as repetition of highest-DF drivers. Therefore, for AF patients with significant spatial and temporal variability, the CEI may assist in the planning of ablation strategy by identifying drivers with high-occurrence rate as effective targets for AF termination. The present imaging results were retrospectively evaluated with clinical outcome and the DF sites found from paroxysmal patients were consistent with ablation sites. The CEI also identified untargeted high-frequency sources which might be a reason of AF maintenance in persistent AF cases. Our findings suggest that the CEI is able to image AF triggers and substrates featured by high-frequency activities during AF. Hence it offers the potential to further aid in clinical intervention of AF by pre-surgically pinpointing regions of interest and personalizing the ablation strategy.

A recent study, using a sheep model has demonstrated that DF increased with the progression from paroxysmal to persistent AF, and that the speed of DF change was strongly correlated with the time of AF transition (Martins et al. 2014). The dynamic transition of DF reflects altered activation frequency resulting from the complex atrial remodeling process; hence, investigating spectral variation may yield insights into novel AF mechanisms. Since there are limitations in extrapolating from animal models, and spontaneous AF are likely to have different mechanisms, it is important to study how electrical activity behaves as AF evolves in human subjects in real-life settings. The CEI

technique enables noninvasive electrical imaging from body surface recording; hence it provides the potential to investigate AF mechanism in intact human hearts and gives more insights into the realistic electrical remodeling process.

The paroxysmal AF data presented here reveals the underlying AF mechanisms. Specifically, the existence of sustaining left-to-right DF gradients is consistent with the spatiotemporal organization of paroxysmal AF (Sanders et al. 2005, Lazar et al. 2004, Skanes et al. 1998, Skanes et al. 1998). The single or multiple highest DF sites featured by high-frequency periodical electrical activities are in good agreements with ablation sites. The observation of temporal variation as well as spatial repeatability of the highest DF sites agree with the spatio-temporal complexity of AF itself and is further supported by previous findings (Konings et al. 1994, Schuessler et al. 2006). The abovementioned observations suggest localized sites of high-frequency electrical activities with a corresponding frequency hierarchy as the mechanism of AF in patients studied.

The CEI method also offers the potential to further aid in clinical intervention of paroxysmal AF. Patients with paroxysmal AF may have non-PV triggers (Lin et al. 2003). The locations of AF triggers in these patients were found to be dispersive over LA and RA. Therefore, it is of clinical significance to distinguish between PV and non-PV initiated paroxysmal AF and to further predict the location of the non-PV triggers. As the highest DF is closely associated with such underlying source maintaining AF, the CEI may characterize locations of the high-frequency sources and optimize the ablation strategy pre-operatively.

Our technique also has important clinical implication for assisting the ablation of

persistent and long standing persistent AF, which has much lower success rates than paroxysmal AF. Compared with the paroxysmal AF, it is characterized by spatiotemporal disorganization, a loss of the hierarchical frequency gradient, and a biatrial dispersion of the highest DFs (Sanders et al. 2005, Lazar et al. 2004). It has also been suggested that failure of termination might be due to the untargeted critical highest DF dispersed at both atria (Sanders et al. 2005, Lazar et al. 2004, Atienza et al. 2009). The temporal complexity of persistent and long-standing persistent AF results in the challenge of intraoperative mapping (Habel et al. 2010). Knowledge regarding the spatio-temporal distributions of these underlying substrates is important and might help improve the ablation outcome. While clinical sequential mapping is limited in this aspect (Habel et al. 2010) , the CEI technique offers the potential to localize these critical DF sites, image the spatiotemporal variation of highest DF before clinical intervention and assist in individualizing the ablation strategy.

We have used a 2D equivalent current density source model to represent atrial electrical activity. Due to the very thin nature of atria over most areas, such approximation is deemed appropriate which is supported by our promising clinical results. In a more accurate source model, one would need to account the volume nature of atria by expanding the 2D atrial surface current density source model to a 3D atrial current density source model, see (Liu et al. 2006, Han et al. 2008, Han et al. 2011, Han et al. 2012, Han et al. 2013, Han et al. 2010, Han et al. 2010).

The current density distribution (the source model adopted in this study) maybe interpreted as the spatial gradient of the transmembrane potential and thus its components

are dependent to the direction of the activation wavefront, e.g. the directional component will be zero if parallel with the activation wavefront. It has similar biophysical indication to intracardiac bipolar EGMs which have already been used for clinical DF maps – both are physical scalars due to the propagation of activation wavefront and reflect local excitation frequency. For these considerations, we have performed the spectral analysis on the norm of the current density vector. Alternatively one may perform FFT on individual directional components which maybe computationally more efficient, but there maybe challenges in its biophysical interpretation.

To our knowledge, this study represents the first report to noninvasively imaging the frequency feature of AF from BSPM by coupling the cardiac electric imaging technique with dominant frequency concept. This technique has important clinical implication for assisting catheter ablation, individualizing ablation strategy, and facilitating the study of AF mechanism in real-life setting. The scope of the present study is to evaluate the feasibility of CEI to imaging DF behaviors during AF, thus a relatively limited number of patients was included. A large-scale patient study including paroxysmal, persistent and long-standing persistent AF patients is needed for further rigorous evaluation.

In the present study, direct intracardiac DF map is not available due to the fact that the acquisition of bi-chamber electrograms is not a standard clinical routine. We evaluated the frequency-based CEI by 1) comparing the highest DF sites with ablation sites and 2) comparing the overall spectral characteristics with literatures of intracardiac DFs. Multiple studies with intarcardiac AF electrograms and body surface potential maps

(Petrutiu et al. 2009, Guillem et al. 2013, Bojarnejad et al. 2012, Bojarnejad et al. 2014), reported that the DFs presented in atria were correlated with DFs presented on the body surface: 1) high frequency sites on the torso are correlated with high frequency sites in the closest chamber; 2) the LA-to-RA DF gradient in atria can also be observed on the body surface; 3) regions of maximal DF can be reflected on the body surface. Therefore, although DF map from intracardiac recording is not available in current study, comparing simultaneous BSPM DF with imaged DF suggests the qualitative concordance between these two measures.

4.5 Conclusions

We have developed a new approach integrating cardiac electric imaging with spectral analysis, and evaluated the method in a group of patients suffering from AF. The present study reports for the first time a noninvasive investigation of the spatial distribution of dominant frequency and identifying high-frequency drivers that maintain AF. The frequency based cardiac electric imaging revealed high frequency drivers consistent with ablation sites in the patients studied. The present results indicate noninvasive frequency analysis of AF is feasible and may give insight into the underlying mechanism in intact human hearts. Furthermore, a priori knowledge of the atrial substrate maintaining the fibrillation activity may help individualize ablation strategy, improve ablation outcome, and reduce procedural time.

Chapter 5

Noninvasive Imaging of Atrial Activations

5.1 Introduction

Electrophysiological mapping is an important clinical tool for the management of cardiac arrhythmias. The acquisition of electrical information for substrate and ectopic foci enables the individualization of therapeutic plan and effective guidance of catheter ablation. However, the minimal invasive procedure might increase patients' burden due to the requirement of sedation and the need of prolonged time for acquiring high-resolution bi-chamber maps. Instead, cardiac electric source imaging technique is an alternative way to delineate the electrophysiology of the heart. Such approach translates the body surface ECG distribution into cardiac electric sources throughout the heart domain, thus allowing direct interpretation of electrical activities without the need of invasive mapping procedure. By reconstructing bi-chamber cardiac electric activities by using a single heartbeat, it allows effective guidance of ablation for arrhythmias with unstable hemodynamics and further facilitates current understanding of the mechanisms of complex arrhythmias.

Many efforts have been made in the development of cardiac electric source imaging techniques. Investigations have been made to reconstruct the single moving dipole (Gulrajani et al. 1984b, Armoundas et al. 2003, Lai et al. 2010), the epicardial

potentials (Barr et al. 1977, Oster et al. 1997, Greensite & Huiskamp 1998, Cuppen & Van Oosterom 1984, Jamison et al. 2011), and the heart surface isochrones (Cuppen & Van Oosterom 1984, Huiskamp & Greensite 1997, Pullan et al. 2001, Tilg et al. 2002, Tilg et al. 2003, Tilg et al. 2003, Seger et al. 2006), by integrating the BSPMs with heart-torso geometry and solving the electrocardiographic inverse problem. Recently, efforts have been made to image the cardiac electrical activities throughout the 3-dimensional (3D) myocardium (He & Wu 2001, He et al. 2003, He et al. 2002, Ohyu et al. 2002, Liu et al. 2006, Nielsen et al. 2007, Liu et al. 2008, Han et al. 2008, Li & He 2001, Wang et al. 2010). As atrial arrhythmias account for a large patient group, efforts have been made to noninvasively image atrial electrophysiology by using the above-mentioned approaches. In the last two decades, the cardiac electrical imaging technique has been mainly utilized to image atrial activations with a focal-onset or a macro-reentry mechanism (Tilg et al. 2001, Tilg et al. 2003, Seger et al. 2006, Modre et al. 2003, Ramanathan et al. 2004, Ramanathan et al. 2006, Wang et al. 2007a, Roten et al. 2012, Shah et al. 2013, Cakulev et al. 2013, Wang et al. 2007b, Revishvili et al. 2015). In these investigations, validations on human subjects were performed by quantitatively comparing noninvasively-obtained activation sequences in the atrium with the electroanatomic maps during atrial pacing, evaluating the performance of identifying chambers of focal origins or reentry, or qualitatively comparing flutter circuits with CARTO map. Although these studies have contributed to the management of atrial arrhythmias, rigorous and quantitative validations is needed, specifically, for those

patients with macro-reentry in the atrium, to fully prove the clinical validity of the technique.

In recent years, a novel 3D cardiac electrical imaging approach has been developed to mathematically model the ventricular electrical activities by using ECD distribution. The method has been rigorously validated with systematic computer simulations and animal studies using 3D intracardiac mapping (Liu et al. 2006, Han et al. 2008, Han et al. 2011, Han et al. 2012, Han et al. 2013). Due to the fact that atrial electrical signal is much smaller than the ventricular signal, imaging the atrial activities can be intrinsically challenging. The purpose of the present study is to further extend the application of the CEI technique from imaging ventricular activation to imaging atrial activation, in the case of both focal pattern and reentrant excitation in the atria, in a quantitative manner. The performance was quantitatively assessed by comparison with invasive mapping using CARTO. The imaging results from normal subjects and patients with atrial flutter were consistent with both CARTO maps and historical findings, suggesting that CEI is capable of delineating atrial activation pattern on a single-beat basis and that it's feasible to reconstruct reentrant activation with close similarity to direct intracardiac mappings.

This chapter has been accepted for publication at PLOS ONE (Zhou et al. 2016b)

TABLE 3
CLINICAL CHARACTERISTICS OF THE STUDY POPULATION

#	Age	Gender	Classification	Clinical History*	Atrial Size	Clinical intervention	Clinical Outcome
AL2	60	M	AFL	N/A	Normal	Linear ablation at TI	SR
AY3	67	F	AFL	Pulmonary Hypertension Tricuspid Insufficiency	LA Enlargement	Linear ablation at TI	SR
AX4	47	F	AFL	Hypertension Aortic Insufficiency Mitral Insufficiency	LA Enlargement	Linear ablation at TI	SR
NS5	36	M	SR	N/A	Normal	N/A	N/A
NS6	32	M	SR	N/A	Normal	N/A	N/A
NS7	26	M	SR	N/A	Normal	N/A	N/A
NS8	34	M	SR	N/A	Normal	N/A	N/A

M = Male; F = Female; LA = Left atrium; RA = Right atrium; CPVI = Circenferential pulmonary vein isolation; TI = Tricuspid isthmus; SR = Sinus rhythm. *Selected medical history

5.2 Study design

5.2.1 Data collection

The study population includes 7 subjects (5 males; 2 females) with atrial flutter (AFL, n=3) or sinus rhythm (n=4). The characteristics of the study population are summarized in Table 3. All protocols were approved by the Institutional Review Board (IRB) of the Ruijin Hospital (affiliated to Shanghai Jiaotong University School of Medicine, Shanghai, China) and University of Minnesota, where written informed consent was obtained from all patients before data collection was performed. Fig. 14

shows the schematic diagram of the study.

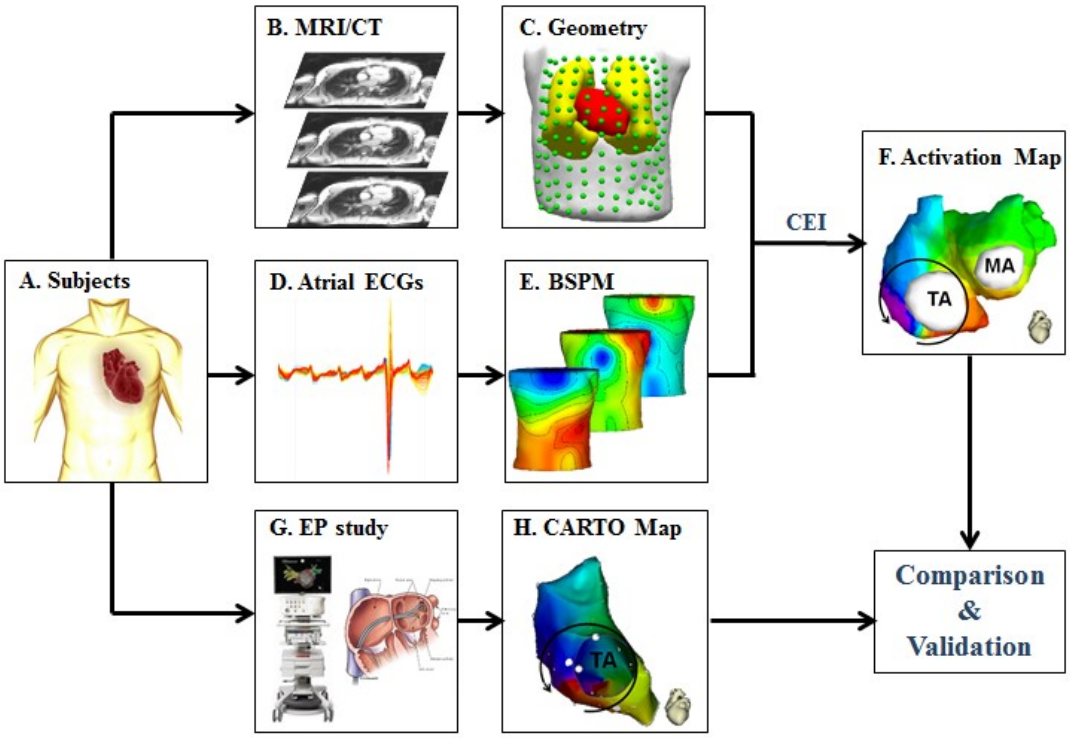

Fig. 14: Schematic diagram. BSPM = body surface potential map.

5.2.2 Anatomic data collection

Computer Tomography (CT) was performed on patients with atrial flutter in order to obtain subject-specific heart-torso geometry. The heart geometries were obtained by continuous volume scanning from the great vessel level down to the diaphragm with intravenous (IV) contrast. The slice thickness was 0.4 mm and was fine enough for the segmentation of a refined heart model. Additional torso scans were performed with a slice thickness of 6 mm from the level of collar bone down to the lower abdomen, which were used to build the thorax model. The in-plane resolution of the CT scans was fixed at

512 x 512 pixels. Respiration was held by alerting the patient before the scanning in order to avoid respiratory artifact. Continuous ECG was monitored and used for gating the CT scanner. Magnetic resonance imaging (MRI) was performed on the other four healthy subjects with the same geometric coverage of CT. The slice thickness of MRI was 2 mm for the heart and 5 mm for the torso.

The CT and MRI images were further processed by commercial software (Curry 6.0, Neuroscan, North Carolina) to obtain the individual heart-torso geometry. The heart and torso images were coupled based on important cardiac anatomical landmarks, such as the apex, and the co-registration errors were minimized with the assistance of Curry 6.0.

Detailed anatomy structures including the atria, the ventricles, the lung and the torso were segmented. For the segmentation of the atria, important anatomical structures, like the pulmonary veins (PV), superior vena cava (SVC), inferior vena cava (IVC), tricuspid annulus (TA) and mitral annulus (MA), were identified and marked.

5.2.3 Body surface potential mapping

For each patient, the BSPMs was recorded at resting state (supine position with smooth breath) by using a total of 208 channels of Ag-AgCl carbon electrodes (BioSemi Active-Two), with a sampling rate of 2048 Hz and a 24 bit analog-to-digital converter. In order to retrieve full comprehensive electrical activities, the electrodes were placed on both the anterior chest (n=144) and the posterior trunk (n=64). The surface ECGs were further filtered with a 1-400 Hz cut off frequency of bandpass filter. After the BSPM recording has done, the locations for electrodes were recorded using a radio frequency digitizer (Fastrak, Polhemus Inc., Vermont). During the recording of BPSM, patients

were told to keep still with smooth respiration in order to minimize baseline wandering and motion artifacts. BSPMs were grounded with Wilson center terminal (WCT) and filtered with either 50-Hz or 60-Hz second-order infinite impulse response notch filter to remove the utility frequency component.

5.2.4 Data analysis

The physical-model-based CEI technique was previously used to reconstruct the activation sequence throughout the ventricular myocardium and validated with animal studies (Han et al. 2008, Han et al. 2011, Han et al. 2012, Han et al. 2013). In the present study, the application of CEI was firstly extended to estimate atrial activation sequences. The forward computation and inverse method were described in details in previous publications (Han et al. 2008, Han et al. 2011, Han et al. 2012). Briefly, subject-specific geometry models were reconstructed from MRI/CT and translated into boundary element models, using a commercial software package Curry 6.0 (Neuroscan, North Carolina). Due to the thinness of atrial wall, the electrical activities were assumed to occur over 2-dimensional (2-D) surface other than the 3-D volume, hereby the source surfaces are defined as the endocardium of the LA and RA. The LA and RA were discretized into 1445±242 grid points with a spatial resolution of 3mm for the inverse computation. The 2-D distributed ECD representing cardiac electric sources were thus reconstructed by coupling measured BSPM with BEM to solve the inverse problem (Liu et al. 2006, Han et al. 2008).

5.2.5. Principle of current density reconstruction

In current study, the cardiac source is modeled as the ECD which distributed over

the endocardial surfaces of the left and right atria. The ECD is then reconstructed from the surface potentials. More details of the inverse solution are provided in chapter 2. Briefly, this linear inverse problem was solved using the minimum norm least square (MNLS) solution (D, 1995; Liu et al, 2006; Wang et al, 1992). The MNLS method (Wang et al. 1992) has been widely used to solve equation (2.5) in chapter 2 and was also used in the study to provide optimal estimate of ECD in the least-squares sense. In equation (2.5), the dipole sources $J(t)$ are assumed to have arbitrary orientations and strengths but fixed and pre-assigned locations. Therefore the leadfield matrix L remains unchanged throughout the fit. The model term $\|WJ(t)\|_2^2$ is needed for searching unique solution in a problem with such large number of free parameters (e.g. unknown dipole moment per location)(He & Wu 2001, Compumedics 2008).

Fig. 15A shows the reconstructed $J(t)$ for three time instants: earliest onset, intermediate phase when both atria were excited, latest excitation. The direction of $J(t)$ is presented by visualizing the corresponding x, y, and z components for the three time instants (Fig. 15B). The unit for the current density is $\mu A/mm^2$. For a given time instant t, the area where the excitation wavefront travels through presents relatively high current density values. At the time instant of earliest excitation t_1, relatively high current densities were found at the location of SVC, which corresponds to the anatomic location of SA node where the activation starts from. At the time instant t_3 of latest excitation, highest current densities were found at the left atria appendage.

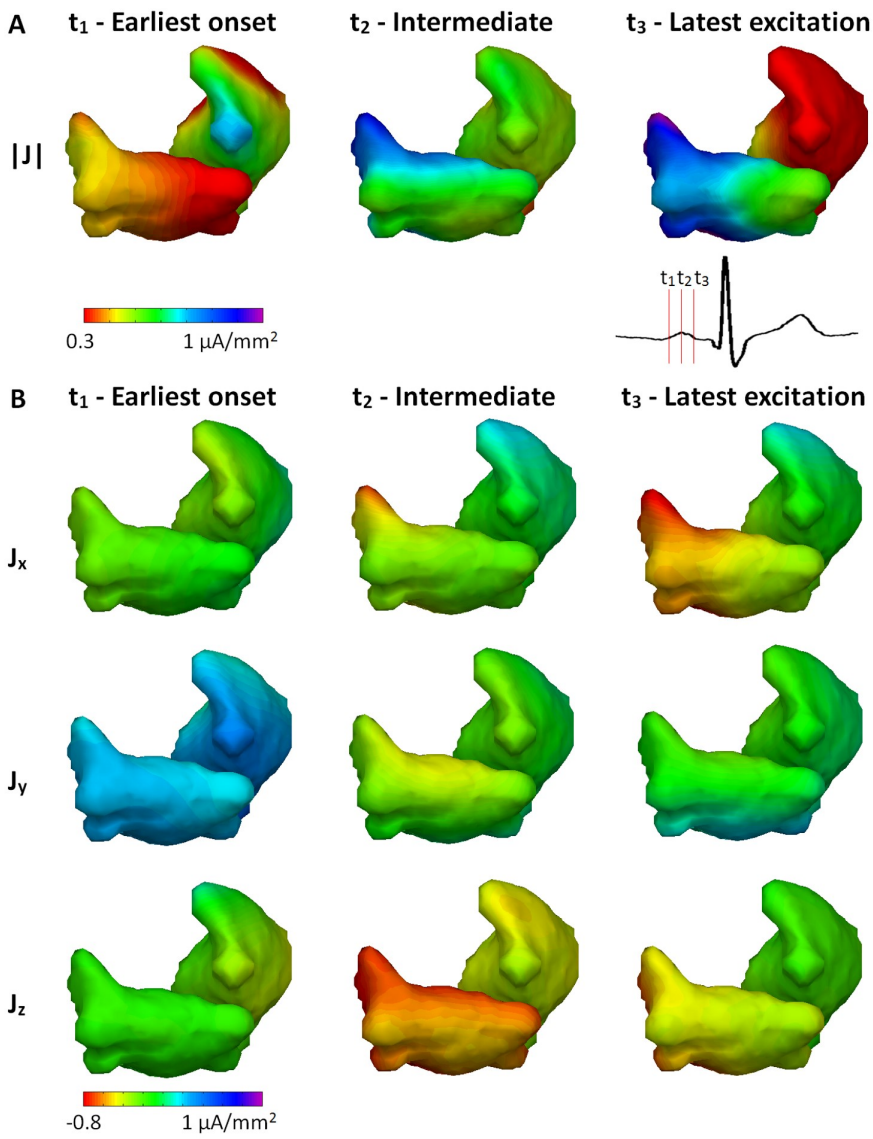

Fig. 15: (A). J(t) reconstructed at three time instants: earliest onset, intermediate phase when both atria were excited, latest excitation; (B) The strength of J|t| at x, y, and z direction.

By definition, ECD is proportional to the gradient of transmembrane potentials. From the peak criterion proposed in our previous studies, the activation time τ at a given location i was determined as the time instant corresponding to the maximum value of

ECD waveform $J(i,t)$:

$$\tau(i) = \underset{t \in T}{\arg\max} (|J(i,t)|) \tag{5.1}$$

Intracardiac activations of AFL patients were recorded on to electroanatomic maps (CARTO, Biosense-webster), and compared with imaged activation times quantitatively by computing the correlation coefficients (CC) and relative error (RE). The equations for calculating CC can be expressed as follows:

$$CC = \frac{\sum_{i=1}^{n}(AT^E - \overline{AT^E})(AT^M - \overline{AT^M})}{\sqrt{\sum_{i=1}^{n}(AT_i^E - \overline{AT^E})^2} \times \sqrt{\sum_{i=1}^{n}(AT_i^M - \overline{AT^M})^2}} \tag{5.2}$$

And RE is defined as:

$$RE = \sqrt{\frac{\sum_{i=1}^{n}(AT_i^E - AT_i^M)^2}{\sum_{i=1}^{n}(AT_i^M)^2}} \tag{5.3}$$

Where n is the number of grid points at the endocardium . AT_i^E and AT_i^M are the i^{th} elements in the estimated activation sequence AT^E and measured activation sequence AT^M, respectively. $\overline{AT^E}$ and $\overline{AT^M}$ are the corresponding mean values.

The registration between CARTO anatomic map and CT geometry were optimized by minimizing the averaged distance between the two sets of points on the surfaces of the anatomic geometries (Liu et al. 2008). For patients with CARTO maps, quantitative comparisons were performed if the average geometry co-registration difference between CT and CARTO is smaller than 1 cm after optimization. A total of 32 cycles of AFL were analyzed, and the imaged activation sequences from single-beat estimations were

compared with the average activation sequences.

5.3 Results

5.3.1 Normal atrial activation

Normal atrial activations were reconstructed from 4 healthy subjects. BSPMs during P-wave were coupled with subject-specific heart-torso geometry to image the atrial activation sequence. Fig. 16 shows one representative example of normal atrial activation obtained from a 36-years old healthy male subject. The activation sequence is color coded from red to violet, corresponding to the earliest and the latest activation. The P-wave used for reconstruction is marked with red window from lead II. The earliest activation initiated in RA from the right border of SVC, which is corresponding to the anatomic location of sinoatrial (SA) node. For LA excitation, the electrical impulse passed to LA through Bachman's bundle，as indicated by the yellow region in the LA of Fig. 16. The latest atrial excitation was found at the inferior LA and LA appendage (LAA).

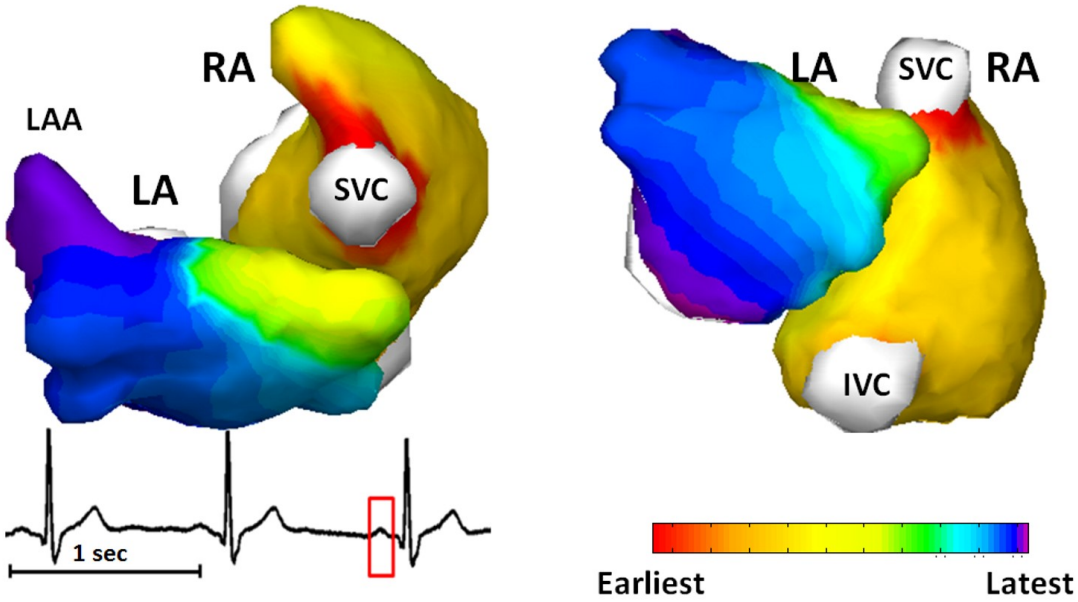

Fig. 16: Imaged normal atrial activation from subject NS5. IVC = inferior vena cava; LA = left atrium; LAA = left atrial appendage; RA = right atrium; SVC = superior vena cave.

Fig. 17 shows another example of the normal atrial activation from a 26-years old male. The earliest activation starts from the SA node located at inferior and right area of SVC (Fig. 17, red region) in RA, travels to LA through Bachman's bundle (Fig. 17, light-red area in LA) and ends up at the inferior LA (Fig. 17, violet region). The locations of SA node were identified from all patients at the regions around SVC. For the group of healthy subjects, the atrial activation patterns show intra group similarity, which can also be observed by comparing Fig. 16 and 17. The features of atrial normal excitation, e.g. SA nodes in the RA indicated by earliest activation sites, the anatomical location of Bachman bundle indicated by earliest excitation site in LA, and the latest activation sites in LA, are consistent with direct recording from isolated human hearts as reported in

literature (Durrer et al. 1970).

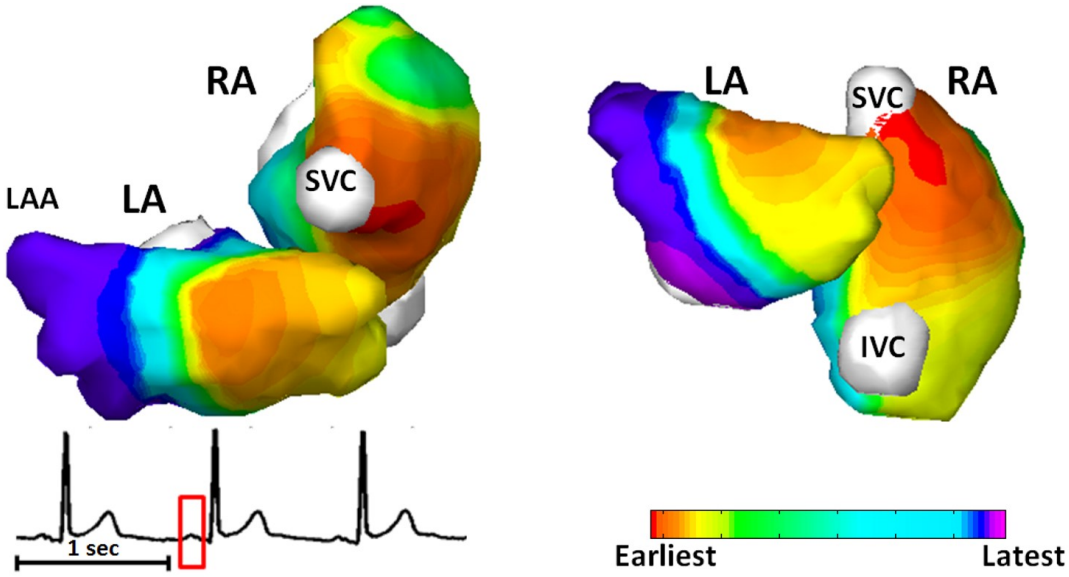

Fig. 17: Imaged normal atrial activation from subject NS7. IVC = inferior vena cava; LA = left atrium; LAA = left atrial appendage; RA = right atrium; SVC = superior vena cave.

5.3.2 Atrial Flutter

Fig. 18 demonstrates the feasibility of CEI to image AFL in subjects with macro reentry. This is a 47-years old female patient with 9-years' history of atrial flutter and did not response to anti-arrhythmia medications. The surface ECG is characterized by saw-tooth waveform at a rate of 285 beats/min with a cycle length of 210 ms. Figure 18.A and 18.B depict one cycle of imaged counter-clockwise typical AFL and the average AFL activation, respectively. The reentry circle in the RA is marked in solid black line. The imaged reentrant circuit ascends from the tricuspid isthmus (TI) near the coronary sinus ostium (CSO), forming an upward wavefront traveling through the septum. The wave front then was split into two branches traveling around SVC anteriorly and posteriorly:

one propagates anteriorly into the area between the SVC and the superior TA; the other excitation wavefront travels posteriorly between SVC and IVC. The two wavefronts then joined together and descends along the RA free-wall, and finally reached the isthmus between TA and IVC at the end of the reentry circuit. The LA activation does not involve in the reentry circuit. The earliest excitation in the LA starts from the inferior LA, indicating the trans-septal activation from RA through coronary sinus (CS). The excitation then propagates upward along the anterior and posterior LA wall. The single-beat-based imaging result and the average activation sequence share similar global activation pattern, which are featured by the macro reentry in the RA, the intra-atria conduction through CS, and the inferior-to-superior excitation in the LA (Fig. 18.A and B). Quantitative comparison between the two activation sequences yield a CC of 0.94 and a RE of 0.37.

The patient received ablation therapy and the AFL was terminated with linear ablation in the isthmus between the inferior vena cava (IVC) and tricuspid annulus (TA) (Fig. 18C, red balls). Endocardial activation map was acquired by using CARTO in EP study (Fig.18C) during stable AFL rhythm. The global activation pattern of noninvasively imaged AFL was found to be in good agreement with the electroanatomic map, which is reflected by a CC of 0.77 and a RE of 0.28.

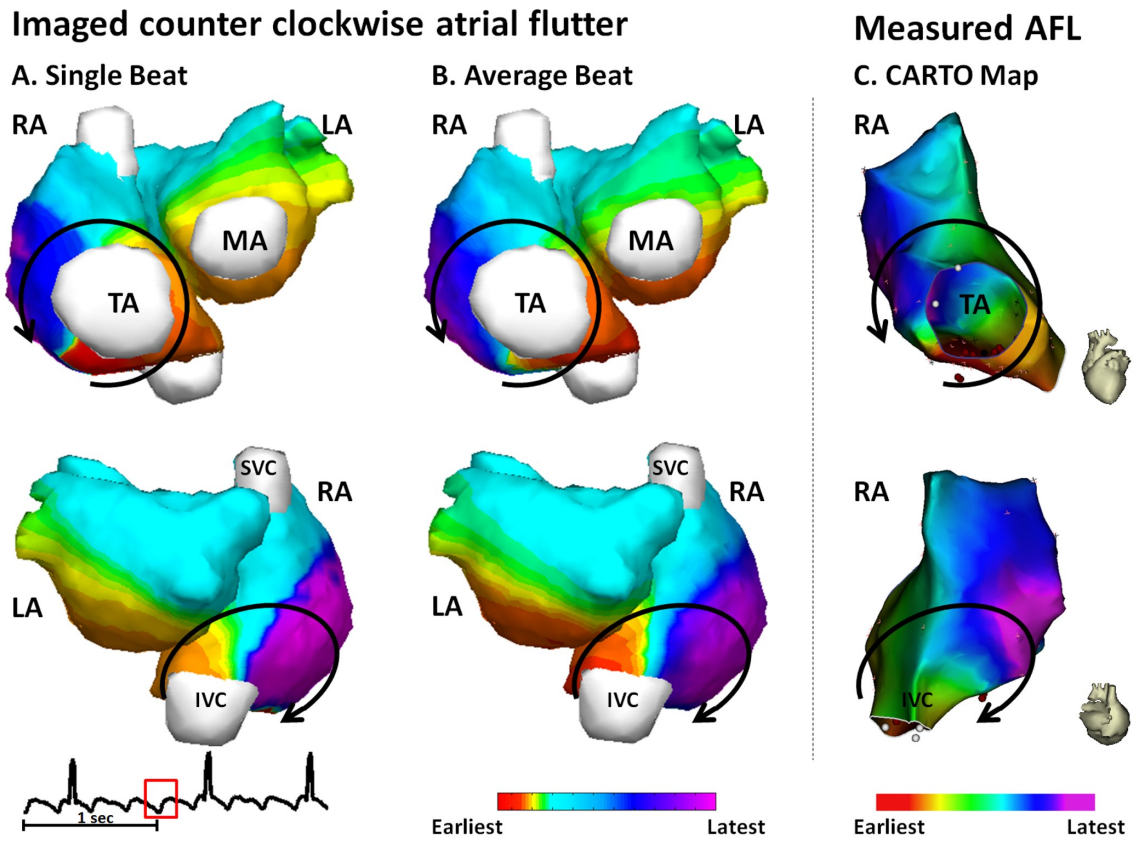

Fig 18: Activation maps for patient AX4. (A) Noninvasively imaged AFL reentry circuit from one single beat. Solid black lines represent propagation wavefronts in RA. (B) Average AFL reentry circuit. (C) CARTO activation map. AFL = Atrial flutter; IVC = Inferior vena cava; LA = Left atrium; MA = Mitral annulus; RA = Right atrium; SVC = Superior vena cava; TA = Tricuspid annulus.

For the patient, a total of 12 independent cycles of atrial flutter were analyzed. The activation sequences imaged from singles beats were quantitatively compared with the average activation sequence as well as the CARTO map. Overall, the activation sequences obtained from independent beats, the average activation sequence, and the activation sequence generated by CARTO share similar global activation pattern and are also in good quantitative agreement with each other (Table 4, subject AX4).

TABLE 4
QUANTITATIVE EVALUATIONS USING THE MEAN ACTIVATION SEQUENCE AND CARTO AS THE REFERENCES.

Reference	Subject #	Number of Beats	CC	RE
Mean	AL2	10	0.90±0.04	0.30±0.06
Activation	AY3	10	0.90±0.03	0.29±0.05
Sequence	AX4	12	0.92±0.03	0.27±0.05
CARTO	AX4	12	0.70±0.04	0.42±0.05

CC = Correlation coefficient; RE = Relative error.

Fig.19 shows another example of the reentry circuit from a 60-years old male. Like most counterclockwise atrial flutter, the activation map is featured by macro reentry in the RA circulating around the tricuspid valve annulus and RA-to-LA propagation through CS (earliest excitation in LA observed at the inferior region near MA). The CC between the single-beat-based activation sequence and the average activation sequence (Fig. 19.B) is 0.90, and the RE is 0.30. For this patient, a total of 10 independent cycles of atrial flutter were analyzed. On average, the single-beat-based global activation sequences share 90% of similarity with the average activation sequence (Table 4, subject AY3).

The patient received ablation therapy and the electroanatomic map was acquired by using CARTO in EP study during stable AFL rhythm. The ablation was delivered at the isthmus between IVC and TA, as shown by the red balls in Fig. 19C. For this patient, Fig. 19 has demonstrated that, both the imaged reentry circuit from single beat and the average reentry circuit are in good agreement with the measurements from clinical EP study.

For AFL, a total of 32 beats were analyzed. For each patient, the single-beat-based activation sequences were averaged to produce the subject-specific mean activation sequence, which was used as a reference to quantitatively evaluate the performance of CEI. Overall, the mean CC is 0.91±0.03, and the mean RE is 0.29±0.05. For each patient, the CC and RE between single-beat-based activation sequences and the mean activation sequences are summarized and reported in table 4.

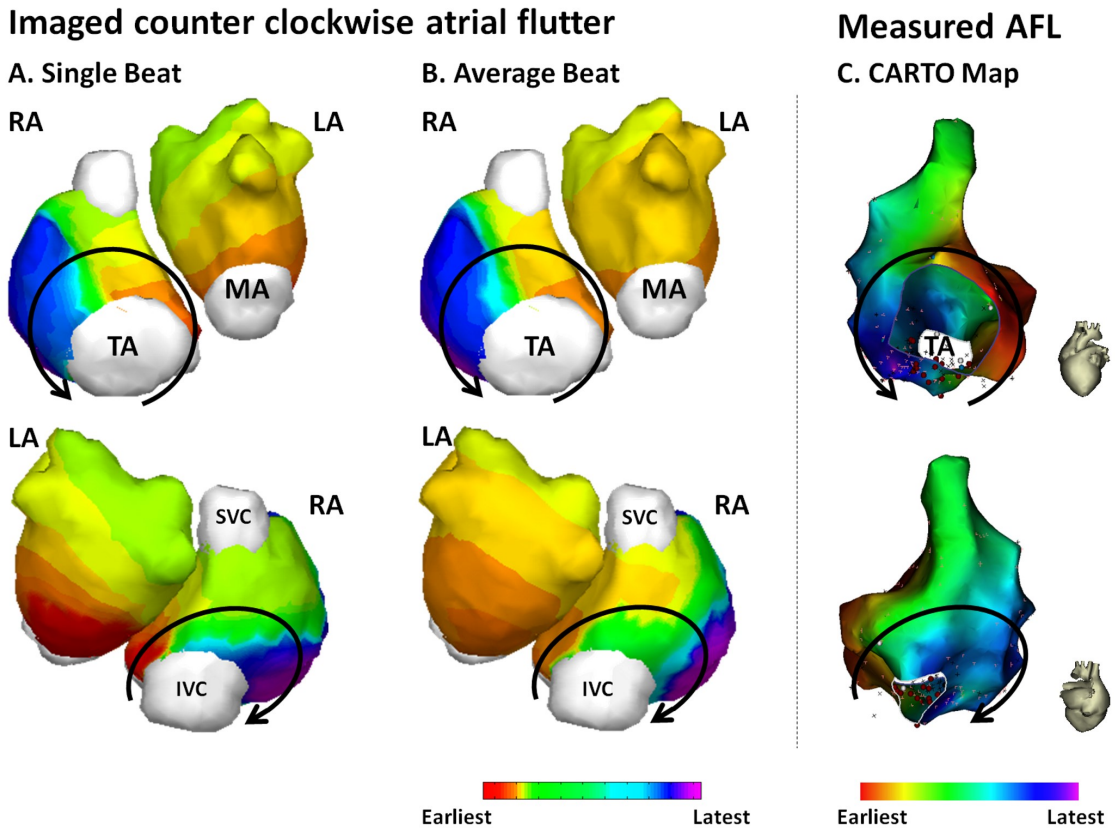

Fig. 19: Activation maps for patient AL2. (A) Noninvasively imaged AFL reentry circuit from one single beat. Solid black lines represent propagation wavefronts in RA. (B) Average AFL reentry circuit. (C) CARTO activation map. AFL = Atrial flutter; IVC = Inferior vena cava; LA = Left atrium; MA = Mitral annulus; RA = Right atrium; SVC = Superior vena cava; TA = Tricuspid annulus.

5.4 Discussion

As cardiac arrhythmias remains a major public health problem, the study of cardiac electrophysiology on individual patient is important for personalizing disease management and treatment. CEI translates the body surface electrical potentials into cardiac sources and provides a noninvasive approach to image cardiac electrical activities. Such noninvasive approach may leverage clinical treatment by assisting in planning for the intervention strategy, localizing ablation targets pre-surgically to shorten ablation time, and helping with post-surgery evaluation over time. In addition, it may also facilitate current understanding to electrophysiological characteristics and mechanisms of spontaneous arrhythmias in intact human hearts, considering that there exists difference between animal models and human in terms of substrate properties.

For the development of cardiac electrophysiological imaging technique, validations on human subjects are important to demonstrate the clinical validity and establish its clinical value. In previous studies of atrial electrical imaging on human subjects, quantitative evaluations were reported for activations with focal onset (Tilg et al. 2001, Tilg et al. 2003, Seger et al. 2006, Modre et al. 2003) (Ramanathan et al. 2004, Ramanathan et al. 2006, Wang et al. 2007a, Roten et al. 2012, Shah et al. 2013, Cakulev et al. 2013, Wang et al. 2007b, Revishvili et al. 2015), by using CARTO recording as the reference. In contrast, the present study has quantitatively evaluate the performance of imaging atrial macro-reentry, by comparing the noninvasively obtained reentry circuits with the CARTO maps. Such quantitative assessment constitute an important part of the clinical study for the technique development. Furthermore, multiple beats (>=10) from

each individual were analyzed and the intra-subject similarities of the imaged activations were evaluated. The high correlations between single-beat-based activation sequences and the average activation sequences (CC=0.91±0.03) has further demonstrated the reliability of the technique in clinical application.

The present study shows that CEI were able to image cardiac rhythm of both focal pattern and reentrant pattern. Previous studies on animal models had demonstrated that CEI can reconstruct ventricular activation with a localization error of 7 mm in canines with pacing rhythm and ventricular tachycardia (Han et al. 2012). In the present study, we further evaluated the performance of CEI on imaging atrial activations in a clinical setting, and compared the results with clinical EP studies from the same patients and also with the published invasive measurements from isolated hearts. The results from normal subjects (Fig. 16 and 17) demonstrated the capability of CEI of imaging atrial focal activations. The activation details regarding initiation of activation wavefront, conducting pathway of Bachman bundle, latest activation site like LAA, were well captured by CEI. The reconstructions are consistent with the publications on isolated human hearts (Durrer et al. 1970), indicating that CEI has the potential to localized ectopic foci in not only the ventricle (Han et al. 2008, Han et al. 2011, Han et al. 2012, Han et al. 2013) but also in the atria. For AFL patients, CEI reconstructed reentry details that could not be observed directly from ECG or BSPM. For counter-clock-wise flutter, the imaged reentry was defined within the RA and in good agreement with the EP measurements (Fig. 18 and 19, which is reflected by an average of CC=0.70±0.04 and an average RE of 0.42±0.05). Besides the macro-reentry in the RA, CEI was also able to capture the electrical

conduction from RA to LA through coronary sinus and the inferior-to-superior activation in the LA. Our results suggested that CEI can reliably reconstruct both focal and reentry activation pattern and its application is not limited in ventricle.

In the present study, the capability of delineating the reentry loop in the atria suggests that CEI may play a useful role in VT management and treatment. The imaged atrial flutters show good consistency with clinical EP mapping Reentry is an important mechanism for ventricular tachycardia (VT) and commonly associated with regions of scar. The reentrant loops are individually different in terms of location, configurations and size since the path of propagation wavefronts are usually pre-defined by unexcitable scar or function block. While clinical catheter mapping requires stable hemodynamics to reconstruct reliable activation map, CEI may help depicting VT reentry circuits and slow conductions by using single beat and translating such electrophysiological properties into a more effective therapy.

In the present study, the CEI technique was utilized to image atrial activation and the reentrant mechanism for the first time. Our result shows the feasibility to image atrial arrhythmias with focal as well as reentrant patterns with close match to literatures and good agreement with clinical EP findings. While the present results are promising, the number of subjects are relatively small. With the feasibility demonstrated in the present work, future investigation should be conducted in a large number of subjects with atrial arrhythmias, including age/gender matched healthy controls. With more rigorous quantitative validation studies and further development in the future, the CEI may become a complementary tool in clinical practice aiding diagnosis and ablation planning

(e.g., localizing ectopic foci and the critical zones for ablation), and further assist in researches of arrhythmic mechanism.

5.5 Conclusion

The present study utilized CEI approach to image atrial activation for the first time. The results suggest that CEI is capable of delineating both focal and reentrant mechanisms in good consistency with EP findings and literatures. The CEI technique offers a noninvasive manner to define arrhythmic mechanism and guide catheter ablation.

Chapter 6

Imaging of Ventricular Activation in an *in situ* Swine Model

6.1 Introduction

For rigorous validation of the novel 3D CEI technique, *in vivo* rabbit and canine studies have been performed in the past during pacing and induced VT (Han et al. 2008, Han et al. 2011, Han et al. 2012, Han et al. 2013). In these *in vivo* studies, plunge needles electrodes has been inserted into the LV and RV myocardium after sternotomy for the recording of intramural bipolar potentials. The 3D intracardiac mapping was then performed simultaneously with body surface potential measurements during different pacing protocols and drug-induced VTs. However, the open-chest protocol might bring in uncertainty to the volume conductor model regarding conductivities and geometry, although these studies have been carefully designed and carried out to minimize potential bias. To complement previous work, the present study aims to evaluate the performance of the 3D CEI technique in an *in situ* closed-chest swine model with the aid of a clinical non-contact mapping (NCM) system, which maximally maintains the integrity of the biological subject and provide closer approximation to clinical settings.

6.2 Materials and Methods

6.2.1 Animal Experiment

The experiment protocol was approved by the Institutional Animal Care and Use

Committee at the University of Minnesota. Fig. 20 shows the schematic diagram of the study. A total of 4 healthy swine (75-85 Kg) were studied. The hemodynamic and electrical monitoring as part of the surgical preparation has been reported in previous studies (Liu et al. 2008, Liu et al. 2012). For each animal, intubation and mechanical ventilation were performed with 65% air and 35% O2 to maintain a PaCO2 of 40 ± 2 mmHg, and anesthetization was performed with a fentanyl infused at 0.75 mcg/kg/min.

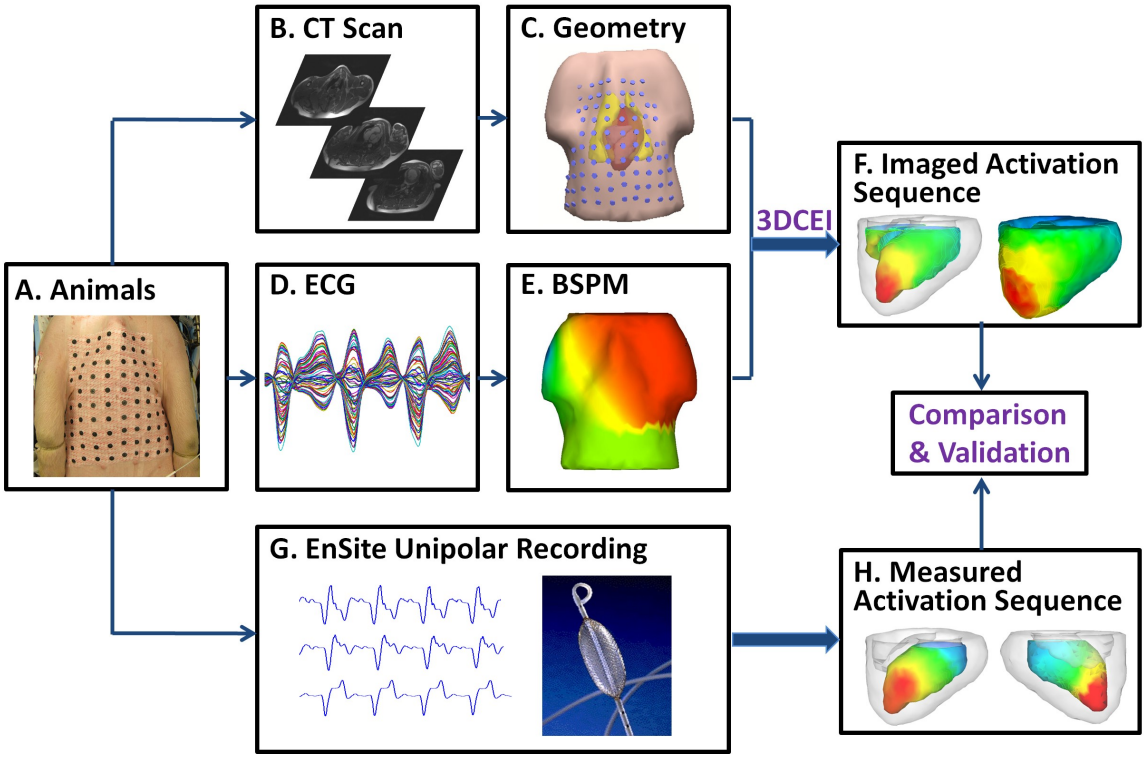

Fig. 20: Schematic diagram of the swine study.

For the purpose of generating alternate activation patterns other than the sinus rhythm, a multi-electrode array catheter (St. Jude Medical, Inc., St. Paul, MN) was introduced into the left ventricle (LV) via the jugular along with a quadripolar electrophysiology catheter (MarinR, Medtronic, Inc., Minneapolis, MN). Pacing

protocols were initiated through the quadripolar catheter at multiple endocardial locations in the LV chamber: the LV apex (LVA), the LV free wall, and the lower septum. Furthermore, dobutamine was infused to induce ventricular arrhythmias, including monomorphic VTs (MVTs), polymorphic VTs (PVT) and premature ventricular complexes (PVCs). The activation sequences over the LV endocardium for both paceing and drug-induced VTs were obtained by using the clinical intracavitary NCM system (EnSite® 3000 NCM system, St. Jude Medical Inc., St. Paul, MN, USA).

The heart-torso geometry of each animal was obtained by performing pre-operative magnetic resonance imaging (MRI). For the recording of BSPMs, up to 100 disposable adhesive electrodes were attached to the anterior torso of the animal. The surface recordings and intracavitary mapping using NCM system (EnSite 3000, St. Jude Medical Inc., St. Paul, MN, USA) were simultaneously performed during different pacing protocols and induced arrhythmias. The 3D locations of the surface electrodes and the fiducial points were recorded using a radio frequency digitizer (Fastrak, Polhemus Inc.). All ECGs recorded from the surface electrodes were referred to the Wilson Center Terminal (WCT).

6.2.2 Principles of the 3D cardiac electrical imaging

Data analyses were performed on 150 paced beats at 10 LV locations and 96 beats of drug-induced arrhythmias including MVTs, PVTs, and PVCs. The physical-model-based 3D CEI technique was applied to inversely estimate the electrical activities throughout the three-dimensional (3D) ventricular myocardium. The forward modeling and inverse solution of the 3DCEI technique were described in previous chapter. In brief,

the realistic heart-torso geometry model was constructed from MRI images for each animal by using a commercial software package CURRY 6.0 (Compumedics, Charlotte, NC). This heart-torso model was further exported for further forward and inverse computation. The electrical conductivities for the torso, the blood cavities in the heart chambers, the lung, and myocardium, were set to 0.2, 0.67, 0.05, and 0.21 S/m, respectively. A distributed ECD model was used to represent the cardiac electric sources within the ventricular myocardium. Based on the bidomain theory (Miller & Geselowitz 1978), given a tessellated geometrical heart-torso model, extracellular potentials measurable over the torso surface are linearly related to the 3D ECD distribution. The ECD was inversely solved from the BSPMs with a generalized regularization technique commonly used for discrete ill-posed problem and weighted minimal norm least square estimation (Wang et al. 1992). The regularization parameter was determined based on the classic L-curve method (Hansen 1992). The activation time at each myocardial site was determined as the instant when the time course of the estimated local ECD reached its maximum magnitude (Liu et al. 2006).

6.2.3 Evaluation of the 3DCEI solutions

The capability of the 3DCEI approach to estimate global 3D activation sequences was evaluated by quantitatively comparing the imaged activation sequence with the activation sequences obtained from NCM. The global activation sequences throughout the myocardium were reconstructed by 3D CEI, based upon the preoperative MRI model. An imaging registration procedure were performed to couple the MRI-based endocardial surface which was used for inverse solution and the NCM-recorded endocardial surface.

A multi-dimensional registration method was applied to minimize the averaged distance between the two sets of special points from the two surfaces (Liu et al. 2008). Thereby we were able to compare the imaging results with the output of the NCM system over identical coordinate.

In the current study, CC and RE were utilized to quantify the agreement and disagreement between imaging results and NCM measurements. The equations for calculating CC and RE are provided in Chapter 5. Other than CC and RE, the performance of this 3DCEI technique was further evaluated by calculating localization error (LE) in pacing conditions. LE gives the Euclidean distance between the imaged pacing sites and the NCM-recorded pacing sites and therefore gives quantitative assessment on the capability of localizing initiation sites. LE is defined as the distance between the site or the center of mass of the earliest endocardial breakthrough from NCM measurements and the center of mass of the endocardial region with the earliest imaged activation time.

6.3 **Results**

6.3.1 Pacing in the swine heart

For paced rhythm, a total of 150 beats of single-site LV pacing from multiple endocardial pacing sites were analyzed (15 beats for each location). The overall performance of 3DCEI in imaging ventricular activation during LV pacing is summarized in Table 5. For each animal, the imaging performance varied between difference anatomical pacing sites. The averaged performance for pacing were 0.77 ± 0.07 for CC and 0.30 ± 0.09 for RE, suggesting good agreement between the estimated activation

sequences and the NCM-obtained activation sequences. The averaged LE was 7.2 ± 2.1 mm, suggesting reasonable localization accuracy when imaging subjects with intact hearts.

Fig. 21 represents an example of the imaging results that was observed when pacing a swine from the LV apex. The left column shows the endocardial activation sequences obtained from the clinical NCM system. The right column shows the imaged activation sequences over the endocardium and epicardium. The spatial distribution of the activation sequence over the ventricular myocardium is color-coded. The red corresponds to early excitation, whereas blue corresponds to late activation. The propagation pattern of the imaged activation sequence over the endocardium surface closely approximated the measured activation sequence. Corresponding quantitative comparison gave a CC of 0.88 and a RE of 0.12. The earliest activation site (black asterisk, Fig. 21, right column) was estimated in close proximity to the actual pacing site (black asterisk, Fig. 21, left column) with a LE of 6.9 mm.

TABLE 5

QUANTITATIVE COMPARISON BETWEEN NCM-ACQUIRED ENDOCARDIAL ACTIVATION SEQUENCE AND IMAGED ACTIVATION SEQUENCE DURING SINGLE SITE PACING IN THE SWINE HEART

Swine #	Pacing Sites	CC	RE	LE (mm)
S1	LVA	0.85	0.15	7.7
	MLW	0.66	0.37	6.1
	BLW	0.68	0.35	8.6
	LLW	0.76	0.33	7.5
S2	LVA	0.84	0.15	6.7
	MLW	0.85	0.34	9.1
	LS	0.73	0.31	8.2
S3	MLW	0.72	0.38	5.8
	LLW	0.83	0.25	6.2
S4	LS	0.72	0.37	5.4
Mean	All Locations	0.77 ± 0.07	0.30 ± 0.09	7.2 ± 2.1

CC, correlation coefficient; RE, relative error; LE, localization error; LVA, LV apex; MLW, middle left wall; BLW, basal left wall; LLW, lower left wall; LS, lower septum.

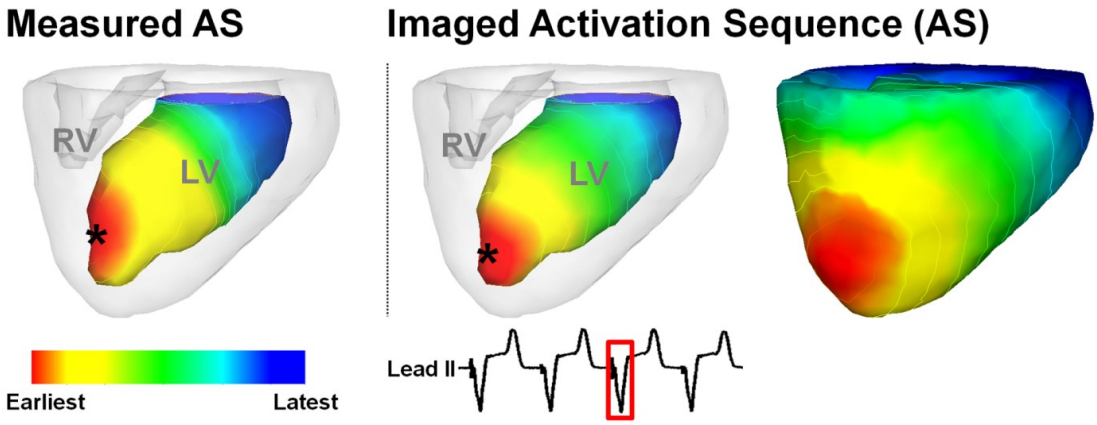

Fig. 21: Imaging result for pacing from LV apex in swine S1. The left column shows the activation sequences obtained from NCM. The right column shows the reconstructed 3D activation sequence over the endocardium and epicardium. The activation sequence is color-coded from red to blue. The red corresponds to early excitation, whereas blue corresponds to late activation. The pacing site and the estimated initiation site of activation are marked by a black asterisk in the left column and right column, respectively. Quantitative comparison gave a CC of 0.88, a RE of 0.12, and a LE of 6.9 mm.

6.3.2 Ventricular arrhythmias

Frequent episodes of nonsustained MVTs and PVTs were observed with the delivery of dobutamine. A total of 96 ventricular ectopic beats were analyzed, including 38 beats of PVT, 54 beats of MVT, and 4 beats of PVC. A focal mechanism was observed from these ectopic beats. The VT beats were initiated from a single site or sequentially from multiple focal sites in the ventricles, including lateral walls and apex. For PVCs, different focal initiation sites were observed, including the right ventricular free wall and the apex. For these VTs and PVCs beats in the swine heart, quantitative comparisons were made between the activation sequences reconstructed from 3DCEI and the activation sequences acquired from NCM. The comparison results are summarized in Table 6. Overall, the imaged activation sequences show good correlation with the NCE-acquired activation sequence, with a CC of 0.74 ± 0.08 and a RE of 0.34 ± 0.07. The averaged LE for imaging earliest LV endocardial breakthrough was 7.6 ± 2.9 mm, suggesting reasonable localization accuracy when imaging ventricular arrhythmias in the closed-chest condition.

TABLE 6
QUANTITATIVE COMPARISON BETWEEN NCM-ACQUIRED ENDOCARDIAL ACTIVATION SEQUENCE AND IMAGED ACTIVATION SEQUENCE DURING DRUG-INDUCED VENTRICULAR ARRHYTHMIAS IN THE SWINE HEART

Swine #	Origin Sites	Arrhythmia types	Number of Beats	CC	RE	LE
S1	LVA	PVT	9	0.81	0.24	8.6
	MRW	PVT	2	0.73	0.27	3.0
	MLW	PVT	3	0.64	0.34	5.5
	BRW	MVT	10	0.63	0.45	4.9
S2	LVA	PVT	6	0.72	0.37	5.9
	BRW	MVT, PVT, PVC	50	0.76	0.34	7.9
S3	LVA	PVT, PVC	10	0.67	0.32	8.8
	LLW	PVT	3	0.76	0.30	10.2
	MRW	PVT, PVC	3	0.66	0.29	9.3
Mean			96	0.74±0.08	0.34±0.07	7.6±2.9

CC, correlation coefficient; RE, relative error; LE, localization error; LVA, LV apex; MRW, middle right wall; MLW, middle left wall; BRW, basal right wall; BLW, basal left wall; LLW, lower left wall; LS, lower septum; PVT, polymorphic ventricular tachycardia; MVT, monomorphic ventricular tachycardia; PVC, premature ventricular complexes

Fig. 22 shows a representative example of nonsustained MVT in swine S2. The VT beat originated from the right ventricular basal right wall by a focal mechanism and the electrical excitation propagated to the LV free wall. The VT beats in this monomorphic episode demonstrated focal initiation at the same LV site as well as similar global activation patterns. The overall imaged activation pattern was consistent with the endocardial measurements, with a CC of 0.76, an RE of 0.29, for this case. The LV endocardial breakthrough was well localized with a LE of 4.1 mm.

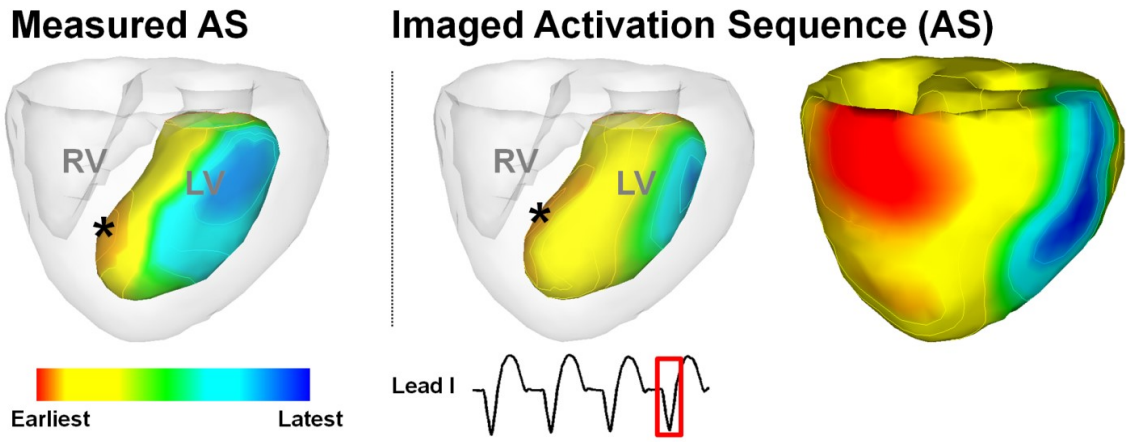

Fig. 22: Imaging result for Monomorphic VT in swine S2. The left column shows the activation sequences acquired from NCM. The right column shows the reconstructed 3D activation sequence. The activation sequence is color-coded from red to blue. The red corresponds to early excitation, whereas blue corresponds to late activation. The black asterisks in the left and right column represent the LV endocardial breakthrough from NCM acquisitions and from imaging results, respectively. Quantitative comparison gave a CC of 0.76, an RE of 0.29, and a LE of 4.1 mm for the imaged beat.

Fig. 23 shows one selected example of imaging nonsustained PVT beats in swine S1. Unlike the MVT, the VT beats in the polymorphic episode show difference in initiation sites and propagation patterns. The first selected PVT beat initiated from the RV middle free wall, then propagate to the LV lateral free wall (Fig. 23A). The earliest LV endocardial breakthrough was found at the LV lower septum. The second selected beat originated from the LV apex and propagate to the LV basal posterior free wall (Fig. 23B). The imaged activation patterns over the LV endocardium surface are in good agreement with the measurement from NCM. Corresponding quantitative comparison gave a CC of 0.84 and a RE of 0.11 for the first beat in Fig. 23A, and a CC of 0.88, RE of 0.17 for the second beat in Fig. 23B. The earliest LV endocardial breakthrough was identified with a LE of 4.1 mm and 6.1 mm, for Fig. 23A and B, respectively.

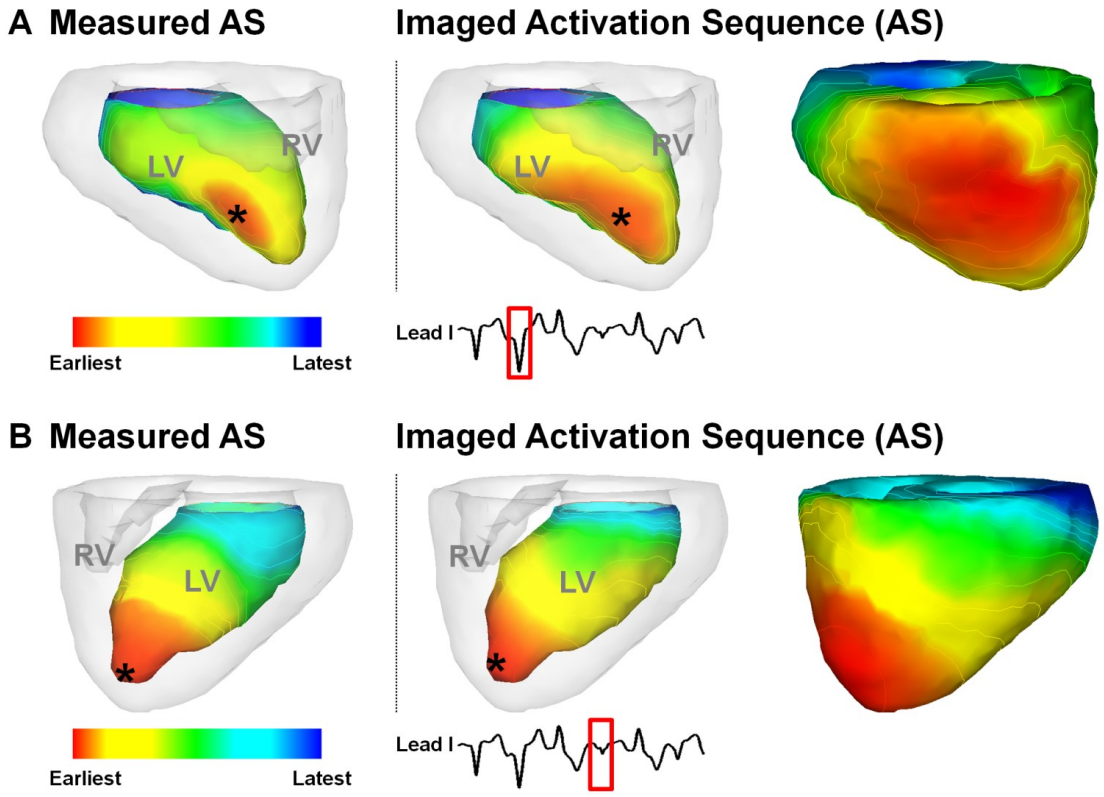

Fig. 23: Comparison between the endocardial activation sequences acquired from NCM and the activation sequences reconstructed from 3DCEI for the first beat (A) and the second beat (B) from a nonsustained PVT episode in swine S1. The endocardial and epicardial surfaces are displayed, respectively, in a right lateral view for beat 1, and left anterior view for beat 2. The measured endocardial breakthrough and the estimated one are marked by a black asterisk in the left column and right column, respectively. CC is 0.84, RE is 0.11, and LE is 4.1 mm for the beat in A, and CC is 0.88, RE is 0.17, and LE is 6.1 mm for the beat in B.

Fig. 24 shows another example of PVTs in swine S2. Similarly, the VT beats in this polymorphic episode are featured by shifting initiation sites and time-dependent propagation patterns. The first selected VT beat initiated from the RV basal lateral free wall, then propagated to the LV lateral free wall (Fig. 24A). The earliest LV endocardial breakthrough was detected at the LV lower septum (black asterisk, Fig. 24A). Later on, the VT beat was detected to originate from the LV apex (Fig. 24B) other than the RV free

wall. The imaged activation patterns are in good consistency with the NCM acquisitions. Corresponding quantitative comparison gave a CC of 0.84 and a RE of 0.29 for the first beat in Fig. 24A, and a CC of 0.75, RE of 0.27 for the second beat in Fig. 24B. The earliest LV endocardial breakthrough was identified with a localization error of 4.3 mm and 7.7 mm, for Fig. 24A and B, respectively.

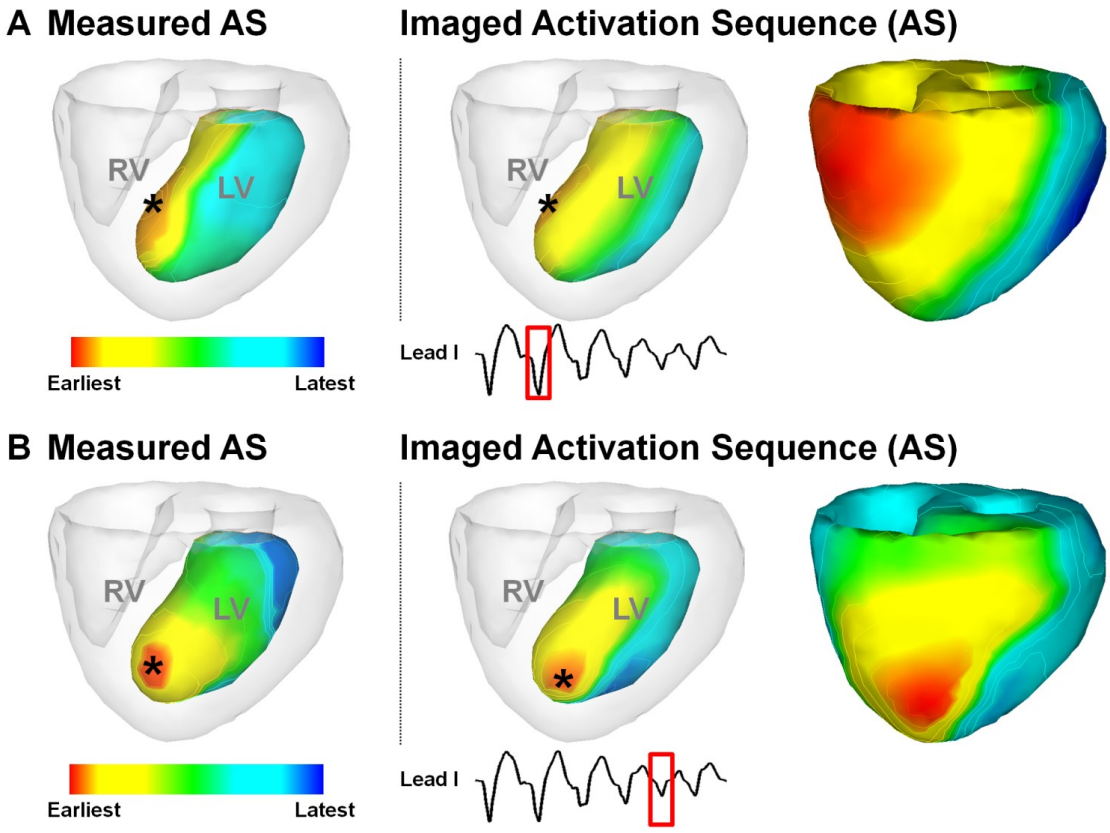

Fig. 24: Comparison between the endocardial activation sequences acquired from NCM and the activation sequences reconstructed by using 3DCEI for the first selected beat (A) and the second selected beat (B) from a nonsustained PVT in swine S2. The endocardial and epicardial surfaces are displayed in a left anterior view. The red corresponds to early excitation, whereas blue corresponds to late activation. The measured LV endocardial breakthrough through and the estimated breakthrough are marked by a black asterisk in the left column and right column, respectively. CC is 0.84, RE is 0.29, and LE is 4.2 mm for the beat in A, and CC is 0.75, RE is 0.27, and LE is 7.7 mm for the beat in B.

6.4 Discussion

In the present study, we have extended the validation of the physical-model-based 3DCEI technique in a closed-chest swine model with the aid of clinical endocardial non-contact mapping technique. The performance in noninvasively imaging the global ventricular activation sequence and localizing the initiation sites for pacing and ectopic beats were evaluated. Quantitative comparison showed a good consistency between the noninvasively reconstructed activation sequence and its endocardial counterparts, as proved by a CC of 0.75, an RE of 0.31, averaged over all 150 paced and 96 ectopic beats. The initiation sites of the activation were characterized with a reasonable resolution of 7.3 mm. The results imply that 3DCEI is capable of reconstructing the spatial patterns of 3D ventricular activation and localizing the arrhythmogenic foci on a single beat basis.

Comprehensive validation studies in *in invo* models are essential for any imaging approaches before it can be developed into a clinical assistive tool. In the present swine study, a closed-chest experimental design were applied in which BSPMs were obtained simultaneously with the electrical recordings from NCM to provide quantitative assessment of the 3DCEI approach. Such closed-chest study constitutes an important part of the in vivo validation of the 3DCEI technique. In our previous validation on rabbit and canine models (Han et al. 2008, Han et al. 2011, Han et al. 2012, Han et al. 2015), transmural plunge needles were inserted into the myocardium after median sternotomy to provide simultaneous intracardiac recording for quantitative comparison. It is unclear whether the open-chest protocol would affect the imaging accuracy due to the change of the torso volume conductor property, although the surgery procedure was carefully

carried out and sectional computed tomography images before and after the sternotomy were acquired to minimize such changes of volume conductor. In contrast to the open-chest protocol, the closed-chest design provides a closer approximation to clinical conditions by ensuring the integrity of the biological system as well as the electrophysiological properties. As we experimented in the open-chest canine model, quantitative comparison between imaged activation sequences and measured activation sequences on both paced and ectopic beats gave an averaged CC of 0.74 and RE of 0.29. Findings from the present closed-chest model are comparable with the open-chest study, as supported by a CC of 0.75 and a RE of 0.31, averaged over all the paced and ectopic rhythm. Furthermore, for the two studies with different protocol, the initiation sites were both estimated to be ~7 mm from the measured sites. The result not only suggests that 3DCEI is capable of imaging activation sequence with reasonably good accuracy in an experimental setting close to clinical condition, but also provide supporting evidence to the validity of the previous open-chest model.

Single-beat noninvasive cardiac activation imaging is important for the clinical diagnosis and management of cardiac arrhythmias, especially those with unstable hemodynamics. Noninvasive characterization of the origin of ectopic rhythm before the intervention enables a more targeted procedure, and therefore is likely to shorten the procedural time and reduce the risk of catheter ablation. In the present study, we have delivered dobutamine to the swine model to induce multiform arrhythmias, including nonsustained PVTs, MVTs and PVCs, in order to resemble arrhythmic activities in the human. The origins of the ventricular arrhythmias have been well localized by the

noninvasive 3DCEI approach with reasonably good accuracy. The performance of VT imaging is consistent with LV pacing imaging in terms of both activation pattern and localization. Moreover, 3DCEI is also capable of imaging the beat-to-beat variations in activation patterns and initiation sites for the elicited PVTs. These results imply that the approach may offer the potential to image focal ventricular arrhythmias on a beat-to-beat basis in clinical practice and facilitate the selection of therapeutic strategies for these arrhythmias.

6.5 Conclusions

3DCEI can non-invasively reconstruct global activation pattern and localize origin of activations during VTs within a clinically relevant range, in this in situ swine model. This approach offers the potential to aid in clinical management of cardiac arrhythmias and to provide novel insights as to their underlying mechanisms.

Chapter 7

Conclusions and Future Work

7.1 Conclusions

Noninvasive cardiac electrical imaging is of great importance to both clinical management of cardiovascular diseases and basic scientific research. In the dissertation, we have taken one step forward to translate the technique into clinical application by extending the physical-model-based three-dimensional cardiac electrical imaging (3DCEI) technique and using it for several cardiovascular diseases, such as atrial arrhythmias and myocardial infarction. We've evaluated the capability of atrial electrical imaging in clinical settings. Furthermore, we've also evaluated the performance of the 3DCEI with the standard in clinical routine by performing the study in an in situ swine heart model with the aid of non-contact mapping system. These promising results represent an important step toward the potential clinical establishment of the 3DCEI technique and also show the potential in aiding in the investigation of the underlying mechanisms.

The computer simulation on myocardial infarction shows that the 3DCEI technique has the potential to characterize electrical abnormal substrates. The present computer simulation study in a realistic human model with various cases of infarctions demonstrates that the physical-model-based 3DCEI can noninvasively identify MI substrates with minimal dependency on the physiological knowledge of the cardiac

electrical properties. The promising results imply a broader application of 3DCEI – it can be used not only to image 3-D activation sequence under normal or pathological conditions but also to identify electrical substrates.

In the present dissertation work, we've further extended the 3DCEI technique for the imaging of atrial arrhythmias. By integrating the spectral analysis with noninvasive cardiac source imaging technique, 3DCEI is capable of localizing the high-frequency drivers during AF and reconstructing the global dominant frequency map. This innovative frequency-based 3DCEI has been evaluated on patients with paroxysmal or persistent atrial fibrillation. The consistency between localized highest-DF sites and ablation sites shows that 3DCEI is capable of delineating electrical activities from a spectral viewpoint and characterizing sites with fast activation rates which might act as the drivers maintaining AF. The capability of imaging the dynamic migration of AF drivers over time indicates that 3DCEI might be used to facilitate current basic research on the mechanism of their initiation and sustenance. The imaging result also implies the potential application of 3DCEI as a clinical useful tool to help identifying potential targets for ablation treatments of both paroxysmal and persistent AF.

The application of 3DCEI on healthy subjects and patients with atrial flutter shows that it is able to image cardiac rhythm of both focal pattern and reentrant pattern. In the study, we evaluated the performance of CEI on imaging atrial activations in a clinical setting, and compared the results with clinical EP studies from the same patients or with the published invasive measurements from isolated hearts. The close match between imaged atrial activation maps and clinical intracardiac maps/historical publications

demonstrated the capability of CEI to localize focal initiation, to delineate reentry loop, and to reconstruct global activation patterns in great details. While clinical catheter mapping requires stable hemodynamics to reconstruct reliable activation map, CEI may help depicting VT reentry circuits and slow conductions by using single beat and translating such electrophysiological properties into a more effective therapy.

We've further evaluated the performance of 3DCEI in in situ heart during ventricular pacing and arrhythmias. Although the capability of 3DCEI in imaging ventricular activation patterns has been rigorously validated in animal models by using plunge needles, questions remain on the uncertainty the sternotomy brings in to the volume conductor model regarding conductivities and geometry, and also on the effect the plunge needles have on the model after insertion (e.g., change of conductivities). The imaging results suggest that the 3DCEI is capable of preserving critical information regarding ventricular excitation (e.g., global activation time, initiation sites of etopic beats) in different experimental and clinical settings.

7.2 Future work

The present dissertation study provides promising results on the physical-model-based 3DCEI approach and also extends the application to atria electrical imaging. There are some works that can be made to further promote the development of 3DCEI technique.

One important contribution of the work lies in that it extends the application of CEI to atria electrical imaging and further evaluates it in clinical setting, which is an

important step to translate it into a clinical useful tool. In the previous studies, the investigation of CEI is concentrated on the imaging of ventricular activation sequence in animal models. In this dissertation study, we adapt the CEI technique to image atrial arrhythmia and evaluate the performance on human subjects in clinical settings, which is an important step toward clinical use. However, the evaluation scheme can be further improved in several ways. For rigorous clinical validation, it is desired to compare real endocardial DF measurements and the reconstructed DF from CEI. Therefore, simultaneous recording of body surface potential and intracardiac electrical activities in clinical setting is needed. In the long run, randomized controlled trials with control group will also be needed to assess the capability of CEI to guide catheter ablation.

Besides animal experiments, it is also important to evaluate the CEI technique on human subjects with ventricular arrhythmias. Previous work in our lab demonstrated that CEI had the capability of imaging experimentally-induced ventricular arrhythmias in pathological hearts (Han et al. 2011, Han et al. 2012, Han et al. 2013, Han et al. 2015, Han et al. 2010). However, some human arrhythmias can be much more complicated than those we have induced experimentally in animal models. Besides, in certain situations, the mechanisms of arrhythmias in human can be very different from those in animal models. Therefore, to further improve the CEI technique and to develop it into a clinical useful application, it would be important to validate the approach in human subjects with ventricular arrhythmias in clinical settings, to quantify its capability of imaging human arrhythmias, and to establish its clinical role in advancing clinical treatments of those heart diseases.

In conclusion, despite many challenges lying ahead, with the integrated efforts put into algorithm development, experimental validation, and clinical evaluation, it can be foreseen that the physical-model-based CEI approach promises to become an important clinical tool for noninvasive diagnosis and treatment of cardiovascular diseases, and may also advance the understanding of the basic pathophysiological mechanisms that underly the cardiac abnormality.

Reference

Abildskov, J.A., Burgess, M.J., Lux, R.L. & Wyatt, R.F. 1976, "Experimental evidence for regional cardiac influence in body surface isopotential maps of dogs", *Circulation research,* vol. 38, no. 5, pp. 386-391.

Akahoshi, M., Hirai, M., Inden, Y., Sano, H., Shimizu, A., Kondo, T., Makino, M., Horiba, M., Yoshida, Y., Tsuboi, N., Hirayama, H., Ito, T., Hayashi, H. & Saito, H. 1997, "Body-surface distribution of changes in activation-recovery intervals before and after catheter ablation in patients with Wolff-Parkinson-White syndrome: clinical evidence for ventricular 'electrical remodeling' with prolongation of action-potential duration over a preexcited area", *Circulation,* vol. 96, no. 5, pp. 1566-1574.

Andersn, H.R., Falk, E. & Nielsen, D. 1987, "Right ventricular infarction: frequency, size and topography in coronary heart disease: a prospective study comprising 107 consecutive autopsies from a coronary care unit", *Journal of the American College of Cardiology,* vol. 10, no. 6, pp. 1223-1232.

Antman, E., Bassand, J.P., Klein, W., Ohman, M., Lopez Sendon, J.L., Rydén, L., Simoons, M. & Tendera, M. 2000, "Myocardial infarction redefined--a consensus document of The Joint European Society of Cardiology/American College of Cardiology committee for the redefinition of myocardial infarction: The Joint European Society of Cardiology/American College of Cardiology Committee", *Journal of the American College of Cardiology,* vol. 36, no. 3, pp. 959.

Armoundas, A.A., Feldman, A.B., Mukkamala, R. & Cohen, R.J. 2003, "A single equivalent moving dipole model: An efficient approach for localizing sites of origin of ventricular electrical activation", *Annals of Biomedical Engineering,* vol. 31, no. 5, pp. 564-576.

Atienza, F., Almendral, J., Jalife, J., Zlochiver, S., Ploutz-Snyder, R., Torrecilla, E.G., Arenal, Á., Kalifa, J., Fernández-Avilés, F. & Berenfeld, O. 2009, "Real-time dominant frequency mapping and ablation of dominant frequency sites in atrial fibrillation with left-to-right frequency gradients predicts long-term maintenance of sinus rhythm", *Heart Rhythm,* vol. 6, no. 1, pp. 33-40.

Barber, M. & Fischmann, E. 1961, "Heart dipole regions and the measurement of dipole moment", vol. 192, pp. 141-142.

Barr, R.C., Ramsey, M. & Spach, M.S. 1977, "Relating epicardial to body surface potential distributions by means of transfer coefficients based on geometry measurements", *Biomedical Engineering, IEEE Transactions on,* vol. BME-24, no. 1, pp. 1-11.

Bellman, R., Collier, C., Kagiwada, H., Kalaba, R. & Selvester, R. 1964, "Estimation of heart parameters using skin potential measurements", *Communications of the ACM,* vol. 7, no. 11, pp. 666-668.

Berger, T., Fischer, G., Pfeifer, B., Modre, R., Hanser, F., Trieb, T., Roithinger, F.X., Stuehlinger, M., Pachinger, O. & Tilg, B. 2006, "Single-beat noninvasive imaging of cardiac electrophysiology of ventricular pre-excitation", *Journal of the American College of Cardiology,* vol. 48, no. 10, pp. 2045-2052.

Berger, T., Pfeifer, B., Hanser, F.F., Hintringer, F., Fischer, G., Netzer, M., Trieb, T., Stuehlinger, M., Dichtl, W. & Baumgartner, C. 2011, "Single-beat noninvasive imaging of ventricular endocardial and epicardial activation in patients undergoing CRT", *PLoS One,* vol. 6, no. 1, pp. e16255.

Bojarnejad, M., Blake, J.R., Bourke, J., Shepherd, E., Murray, A. & Langley, P. 2014, "Non-invasive estimation of left atrial dominant frequency in atrial fibrillation from different electrode sites: insight from body surface potential mapping", *J.Atrial Fibrillation,* vol. 7, no. 3, pp. 6-10.

Bojarnejad, M., Blake, J., Bourke, J.P., Murray, A. & Langley, P. 2012, "Comparing power spectral density of the 64-channel surface ECG with left atrial electrograms in patients in atrial fibrillation", *Computing in Cardiology*IEEE, , pp. 713.

Brooks, D.H., Ahmad, G.F., MacLeod, R.S. & Maratos, G.M. 1999, "Inverse electrocardiography by simultaneous imposition of multiple constraints", *Biomedical Engineering, IEEE Transactions on,* vol. 46, no. 1, pp. 3-18.

Cakulev, I., Sahadevan, J., Arruda, M., Goldstein, R.N., Hong, M., Intini, A., Mackall, J.A., Stambler, B.S., Ramanathan, C., Jia, P., Strom, M. & Waldo, A.L. 2013, "Confirmation of novel noninvasive high-density electrocardiographic mapping with electrophysiology study: implications for therapy", *Circulation.Arrhythmia and electrophysiology,* vol. 6, no. 1, pp. 68-75.

Cerqueira, M.D., Weissman, N.J., Dilsizian, V., Jacobs, A.K., Kaul, S., Laskey, W.K., Pennell, D.J., Rumberger, J.A., Ryan, T. & Verani, M.S. 2002, "Standardized myocardial segmentation and nomenclature for tomographic imaging of the heart", *Circulation,* vol. 105, no. 4, pp. 539-542.

Ciaccio, E.J., Chow, A.W., DAVIES, D., Wit, A.L. & Peters, N.S. 2004, "Localization of the isthmus in reentrant circuits by analysis of electrograms derived from clinical noncontact mapping during sinus rhythm and ventricular tachycardia", *Journal of cardiovascular electrophysiology,* vol. 15, no. 1, pp. 27-36.

Codreanu, A., Odille, F., Aliot, E., Marie, P., Magnin-Poull, I., Andronache, M., Mandry, D., Djaballah, W., Régent, D. & Felblinger, J. 2008, "Electroanatomic characterization of post-infarct scars: comparison with 3-dimensional myocardial scar reconstruction based on magnetic resonance imaging", *Journal of the American College of Cardiology,* vol. 52, no. 10, pp. 839-842.

Compumedics (ed) 2008, *Curry User Guide*, Compumedics USA Inc, Charlotte, NC.

Cuculich, P.S., Wang, Y., Lindsay, B.D., Faddis, M.N., Schuessler, R.B., Damiano Jr, R.J., Li, L. & Rudy, Y. 2010, "Noninvasive Characterization of Epicardial Activation in Humans With Diverse Atrial Fibrillation PatternsClinical Perspective", *Circulation,* vol. 122, no. 14, pp. 1364-1372.

Cuppen, J.J.M. & Van Oosterom, A. 1984, "Model studies with the inversely calculated lsochrones of ventricular depolarization", *Biomedical Engineering, IEEE Transactions on,* vol. BME-31, no. 10, pp. 652-659.

De Ambroggi, L., Aime, E., Ceriotti, C., Rovida, M. & Negroni, S. 1997, "Mapping of ventricular repolarization potentials in patients with arrhythmogenic right ventricular dysplasia: principal component analysis of the ST-T waves", *Circulation,* vol. 96, no. 12, pp. 4314-4318.

Durrer, D., Van Dam, R., Freud, G., Janse, M., Meijler, F. & Arzbaecher, R. 1970, "Total excitation of the isolated human heart", *Circulation,* vol. 41, no. 6, pp. 899-912.

Flowers, N. & Horan, L. 1995, "Body surface potential mapping", *Cardiac Electrophysiology,* , pp. 1049-1067.

Franzone, P.C., Guerri, L., Taccardi, B. & Viganotti, C. 1985, "Finite element approximation of regularized solutions of the inverse potential problem of electrocardiography and applications to experimental data", *Calcolo,* vol. 22, no. 1, pp. 91-186.

Gabriel, S., Lau, R. & Gabriel, C. 1996, "The dielectric properties of biological tissues: II. Measurements in the frequency range 10 Hz to 20 GHz", *Physics in Medicine and Biology,* vol. 41, no. 11, pp. 2251-2269.

Gepstein, L., Hayam, G. & Ben-Haim, S.A. 1997, "A novel method for nonfluoroscopic catheter-based electroanatomical mapping of the heart: in vitro and in vivo accuracy results", *Circulation,* vol. 95, no. 6, pp. 1611-1622.

Geselowitz, D.B. 1960, "Multipole representation for an equivalent cardiac generator", *Proceedings of the IRE,* vol. 48, no. 1, pp. 75-79.

Goldberger, E. 1942, "The aVL, aVR, and aVF leads: a simplification of standard lead electrocardiography", *American Heart Journal,* vol. 24, no. 3, pp. 378-396.

Gornick, C.C., Adler, S.W., Pederson, B., Hauck, J., Budd, J. & Schweitzer, J. 1999, "Validation of a new noncontact catheter system for electroanatomic mapping of left ventricular endocardium", *Circulation,* vol. 99, no. 6, pp. 829-835.

Greensite, F. & Huiskamp, G. 1998, "An improved method for estimating epicardial potentials from the body surface", *Biomedical Engineering, IEEE Transactions on,* vol. 45, no. 1, pp. 98-104.

Greensite, F. 2004, "Heart surface electrocardiographic inverse solutions" in *Modeling and Imaging of Bioelectrical Activity—Principles and Applications*, ed. B. He, Springer, , pp. 119-160.

Guillem, M.S., Climent, A.M., Castells, F., Husser, D., Millet, J., Arya, A., Piorkowski, C. & Bollmann, A. 2009, "Noninvasive mapping of human atrial fibrillation", *Journal of cardiovascular electrophysiology,* vol. 20, no. 5, pp. 507-513.

Guillem, M.S., Climent, A.M., Millet, J., Arenal, A., Fernandez-Aviles, F., Jalife, J., Atienza, F. & Berenfeld, O. 2013, "Noninvasive localization of maximal frequency sites of atrial fibrillation by body surface potential mapping", *Circulation.Arrhythmia and electrophysiology,* vol. 6, no. 2, pp. 294-301.

Gulrajani, R.M., Pham-Huy, H., Nadeau, R.A., Savard, P., Guise, J., Primeau, R.E. & Roberge, F.A. 1984a, "Application of the single moving dipole inverse solution to the study of the Wolff-Parkinson-White syndrome in man", *Journal of electrocardiology,* vol. 17, no. 3, pp. 271-287.

Gulrajani, R.M., Roberge, F.A. & Savard, P. 1984b, "Moving dipole inverse ECG and EEG solutions", *Biomedical Engineering, IEEE Transactions on,* vol. 31, no. 12, pp. 903-910.

Gulrajani, R.M. 2004, "The forward problem of electrocardiography: Theoretical underpinnings and applications" in *Modeling and Imaging of Bioelectrical Activity-Principles and Applications*, ed. B. He, Springer, , pp. 43-79.

Gulrajani, R. 1998, "The forward and inverse problems of electrocardiography", *IEEE Engineering in Medicine and Biology Magazine,* vol. 17, no. 5, pp. 84-101.

Habel, N., Znojkiewicz, P., Thompson, N., Müller, J.G., Mason, B., Calame, J., Calame, S., Sharma, S., Mirchandani, G. & Janks, D. 2010, "The temporal variability of dominant frequency and complex fractionated atrial electrograms constrains the

validity of sequential mapping in human atrial fibrillation", *Heart Rhythm,* vol. 7, no. 5, pp. 586-593.

Haissaguerre, M., Hocini, M., Shah, A.J., Derval, N., Sacher, F., Jais, P. & Dubois, R. 2013, "Noninvasive panoramic mapping of human atrial fibrillation mechanisms: a feasibility report", *Journal of cardiovascular electrophysiology,* vol. 24, no. 6, pp. 711-717.

Haissaguerre, M., Hocini, M., Denis, A., Shah, A.J., Komatsu, Y., Yamashita, S., Daly, M., Amraoui, S., Zellerhoff, S., Picat, M.Q., Quotb, A., Jesel, L., Lim, H., Ploux, S., Bordachar, P., Attuel, G., Meillet, V., Ritter, P., Derval, N., Sacher, F., Bernus, O., Cochet, H., Jais, P. & Dubois, R. 2014, "Driver domains in persistent atrial fibrillation", *Circulation,* vol. 130, no. 7, pp. 530-538.

Han, C., Liu, Z., Liu, C., Pogwizd, S. & He, B. 2007a, "Three-Dimensional Activation Sequence Imaging in a Rabbit Model", *29th Annual International Conference of the IEEE Engineering in Medicine and Biology Society, 2007. EMBS 2007*, pp. 5609.

Han, C., Liu, Z., Pogwizd, S. & He, B. 2007b, "Imaging Three-Dimensional Ventricular Activation Sequence under Dual-site Pacing in a Rabbit Model", *Joint Meeting of the 6th International Symposium on Noninvasive Functional Source Imaging of the Brain and Heart and the International Conference on Functional Biomedical Imaging, 2007. NFSI-ICFBI 2007*, pp. 272.

Han, C., Liu, Z., Zhang, X., Pogwizd, S. & He, B. 2008, "Noninvasive three-dimensional cardiac activation imaging from body surface potential maps: a computational and experimental study on a rabbit model", *Medical Imaging, IEEE Transactions on,* vol. 27, no. 11, pp. 1622-1630.

Han, C., Pogwizd, S., Killingsworth, C., Yan, J. & He, B. 2010, "Noninvasive Three-dimensional Cardiac Activation Imaging of Ventricular Tachycardia in the Rabbit Heart", *Circulation,* vol. 122, no. 21 Supplement, pp. A17255.

Han, C., Pogwizd, S.M., Killingsworth, C.R. & He, B. 2012, "Noninvasive reconstruction of the three-dimensional ventricular activation sequence during pacing and ventricular tachycardia in the canine heart", *American Journal of Physiology-Heart and Circulatory Physiology,* vol. 302, no. 1, pp. H244-H252.

Han, C., Pogwizd, S.M., Killingsworth, C.R. & He, B. 2011, "Noninvasive Imaging of Three-dimensional Cardiac Activation Sequence during Pacing and Ventricular Tachycardia", *Heart Rhythm,* vol. 8, no. 8, pp. 1266-1272.

Han, C., Pogwizd, S.M., Killingsworth, C.R., Zhou, Z. & He, B. 2013, "Noninvasive cardiac activation imaging of ventricular arrhythmias during drug-induced QT prolongation in the rabbit heart", *Heart Rhythm,* vol. 10, no. 10, pp. 1509-1515.

Han, C., Liu, C., Pogwizd, S. & He, B. 2009, "Noninvasive three-dimensional cardiac activation imaging on a rabbit model", *Conference proceedings : ...Annual International Conference of the IEEE Engineering in Medicine and Biology Society.IEEE Engineering in Medicine and Biology Society.Conference,* vol. 2009, pp. 3271-3273.

Han, C., Pogwizd, S.M., Yu, L., Zhou, Z., Killingsworth, C.R. & He, B. 2015, "Imaging cardiac activation sequence during ventricular tachycardia in a canine model of nonischemic heart failure", *American journal of physiology.Heart and circulatory physiology,* vol. 308, no. 2, pp. H108-14.

Hansen, P.C. 1992, "Analysis of discrete ill-posed problems by means of the L-curve", *SIAM Review,* , pp. 561-580.

Hansen, P.C. & O'Leary, D.P. 1993, "The use of the L-curve in the regularization of discrete ill-posed problems", *SIAM Journal on Scientific Computing,* vol. 14, no. 6, pp. 1487-1503.

He, B. (ed) 2004, *Modeling and Imaging of Bioelectrical Activity–Principles and Applications*, Kluwer Academic/Plenum Publishers, New York.

He, B., Li, G. & Zhang, X. 2003, "Noninvasive imaging of cardiac transmembrane potentials within three-dimensional myocardium by means of a realistic geometry anisotropic heart model", *IEEE Transactions on Biomedical Engineering,* vol. 50, no. 10, pp. 1190-1202.

He, B. & Wu, D. 2001, "Imaging and visualization of 3-D cardiac electric activity", *Information Technology in Biomedicine, IEEE Transactions on,* vol. 5, no. 3, pp. 181-186.

He, B. & Cohen, R.J. 1992, "Body surface Laplacian ECG mapping", *Biomedical Engineering, IEEE Transactions on,* vol. 39, no. 11, pp. 1179-1191.

He, B., Li, G. & Zhang, X. 2002, "Noninvasive three-dimensional activation time imaging of ventricular excitation by means of a heart-excitation model", *Physics in Medicine and Biology,* vol. 47, no. 22, pp. 4063-4078.

He, B. & Liu, C. 2010, "Cardiac Electrophysiological Imaging: Solving the Inverse Problem of Electrocardiography" in *Cardiac Electrophysiology Methods and Models* Springer, , pp. 357-373.

He, B., Liu, C. & Zhang, Y. 2007, "Three-dimensional cardiac electrical imaging from intracavity recordings", *Biomedical Engineering, IEEE Transactions on,* vol. 54, no. 8, pp. 1454-1460.

Horan, L.G., Flowers, N.C. & Brody, D.A. 1963, "Body surface potential distribution: Comparison of naturally and artificially produced signals as analyzed by digital computer", *Circulation research,* vol. 13, no. 5, pp. 373-387.

Huiskamp, G. & Greensite, F. 1997, "A new method for myocardial activation imaging", *IEEE Transactions on Biomedical Engineering,* vol. 44, no. 6, pp. 433-446.

Iaizzo, P.A. 2009, *Handbook of cardiac anatomy, physiology, and devices,* Springer Science & Business Media.

Ideker, R.E., Smith, W.M., Wolf, P., Danieley, N.D. & Bartram, F.R. 1987, "Simultaneous multichannel cardiac mapping systems", *Pacing and Clinical Electrophysiology,* vol. 10, no. 2, pp. 281-292.

Jamison, C., Navarro, C., Turner, C., Shannon, J., Anderson, J. & Adgey, J. 2011, "The inverse problem utilizing the boundary element method for a nonstandard female torso", *Biomedical Engineering, IEEE Transactions on,* vol. 58, no. 4, pp. 876-883.

January, C.T., Wann, L.S., Alpert, J.S., Calkins, H., Cigarroa, J.E., Cleveland, J.C., Conti, J.B., Ellinor, P.T., Ezekowitz, M.D. & Field, M.E. 2014, "2014 AHA/ACC/HRS guideline for the management of patients with atrial fibrillation", *Circulation,* vol. 130, no. 23, pp. 2071-2104.

Jia, P., Punske, B., Taccardi, B. & Rudy, Y. 2000, "Electrophysiologic Endocardial Mapping from a Noncontact Nonexpandable Catheter: A Validation Study of a Geometry-Based Concept", *Journal of cardiovascular electrophysiology,* vol. 11, no. 11, pp. 1238-1251.

Johnston, P.R. & Gulrajani, R.M. 1997, "A new method for regularization parameter determination in the inverse problem of electrocardiography", *Biomedical Engineering, IEEE Transactions on,* vol. 44, no. 1, pp. 19-39.

Kadish, A., Hauck, J., Pederson, B., Beatty, G. & Gornick, C. 1999, "Mapping of atrial activation with a noncontact, multielectrode catheter in dogs", *Circulation,* vol. 99, no. 14, pp. 1906-1913.

Khoury, D.S., Berrier, K.L., Badruddin, S.M. & Zoghbi, W.A. 1998, "Three-dimensional electrophysiological imaging of the intact canine left ventricle using a noncontact multielectrode cavitary probe: study of sinus, paced, and spontaneous premature beats", *Circulation,* vol. 97, no. 4, pp. 399-409.

Kinch, J.W. & Ryan, T.J. 1994, "Right ventricular infarction", *New England Journal of Medicine,* vol. 330, no. 17, pp. 1211-1217.

Konings, K., Kirchhof, C., Smeets, J., Wellens, H., Penn, O.C. & Allessie, M.A. 1994, "High-density mapping of electrically induced atrial fibrillation in humans", *Circulation,* vol. 89, no. 4, pp. 1665-1680.

Lai, D., Liu, C., Eggen, M.D., Iaizzo, P.A. & He, B. 2010, "Equivalent moving dipole localization of cardiac ectopic activity in a swine model during pacing", *Information Technology in Biomedicine, IEEE Transactions on,* vol. 14, no. 6, pp. 1318-1326.

Lazar, S., Dixit, S., Marchlinski, F.E., Callans, D.J. & Gerstenfeld, E.P. 2004, "Presence of left-to-right atrial frequency gradient in paroxysmal but not persistent atrial fibrillation in humans", *Circulation,* vol. 110, no. 20, pp. 3181-3186.

Lazzara, R., El-Sherif, N., Hope, R.R. & Scherlag, B. 1978, "Ventricular arrhythmias and electrophysiological consequences of myocardial ischemia and infarction", *Circulation research,* vol. 42, no. 6, pp. 740.

Li, G. & He, B. 2004, "Non-invasive estimation of myocardial infarction by means of a heart-model-based imaging approach: a simulation study", *Medical and Biological Engineering and Computing,* vol. 42, no. 1, pp. 128-136.

Li, G. & He, B. 2001, "Localization of the site of origin of cardiac activation by means of a heart-model-based electrocardiographic imaging approach", *Biomedical Engineering, IEEE Transactions on,* vol. 48, no. 6, pp. 660-669.

Lin, W.S., Tai, C.T., Hsieh, M.H., Tsai, C.F., Lin, Y.K., Tsao, H.M., Huang, J.L., Yu, W.C., Yang, S.P. & Ding, Y.A. 2003, "Catheter ablation of paroxysmal atrial fibrillation initiated by non–pulmonary vein ectopy", *Circulation,* vol. 107, no. 25, pp. 3176-3183.

Liu, C., Skadsberg, N.D., Ahlberg, S.E., Swingen, C.M., Iaizzo, P.A. & He, B. 2008, "Estimation of Global Ventricular Activation Sequences by Noninvasive Three-Dimensional Electrical Imaging: Validation Studies in a Swine Model During Pacing", *Journal of cardiovascular electrophysiology,* vol. 19, no. 5, pp. 535-540.

Liu, C., Eggen, M.D., Swingen, C.M., Iaizzo, P.A. & He, B. 2012, "Noninvasive mapping of transmural potentials during activation in swine hearts from body surface electrocardiograms", *Medical Imaging, IEEE Transactions on,* vol. 31, no. 9, pp. 1777-1785.

Liu, Z., Liu, C. & He, B. 2006, "Noninvasive reconstruction of three-dimensional ventricular activation sequence from the inverse solution of distributed equivalent

current density", *Medical Imaging, IEEE Transactions on,* vol. 25, no. 10, pp. 1307-1318.

Liu, Z.W., Jia, P., Biblo, L.A., Taccardi, B. & Rudy, Y. 1998, "Endocardial potential mapping from a noncontact nonexpandable catheter: a feasibility study", *Annals of Biomedical Engineering,* vol. 26, no. 6, pp. 994-1009.

Liu, Z., Liu, C. & He, B. 2006, "Three-dimensional ventricular activation imaging by means of equivalent current source modeling and estimation", *Conference proceedings : ...Annual International Conference of the IEEE Engineering in Medicine and Biology Society.IEEE Engineering in Medicine and Biology Society.Conference,* vol. 1, pp. 4524-4527.

MacLeod, R.S. & Brooks, D.H. 1998, "Recent progress in inverse problems in electrocardiology", *Engineering in Medicine and Biology Magazine, IEEE,* vol. 17, no. 1, pp. 73-83.

Malmivuo, J. & Plonsey, R. (eds) 1995, *Bioelectromagnetism: Principles and Applications of Bioelectric and Biomagnetic Fields*, Oxford University Press, USA.

Martins, R.P., Kaur, K., Hwang, E., Ramirez, R.J., Willis, B.C., Filgueiras-Rama, D., Ennis, S.R., Takemoto, Y., Ponce-Balbuena, D., Zarzoso, M., O'Connell, R.P., Musa, H., Guerrero-Serna, G., Avula, U.M., Swartz, M.F., Bhushal, S., Deo, M., Pandit, S.V., Berenfeld, O. & Jalife, J. 2014, "Dominant frequency increase rate predicts transition from paroxysmal to long-term persistent atrial fibrillation", *Circulation,* vol. 129, no. 14, pp. 1472-1482.

Mehra, R., Zeiler, R.H., Gough, W.B. & El-Sherif, N. 1983, "Reentrant ventricular arrhythmias in the late myocardial infarction period. 9. Electrophysiologic-anatomic correlation of reentrant circuits", *Circulation,* vol. 67, no. 1, pp. 11-24.

Miller, W. & Geselowitz, D.B. 1978, "Simulation studies of the electrocardiogram. I. The normal heart", *Circulation research,* vol. 43, no. 2, pp. 301-315.

Mirvis, D.M. 1980, "Body surface distribution of electrical potential during atrial depolarization and repolarization", *Circulation,* vol. 62, no. 1, pp. 167-173.

Mirvis, D.M., Keller, F.W., Ideker, R.E., Cox Jr, J.W., Dowdie, R.F. & Zettergren, D.G. 1977, "Detection and localization of multiple epicardial electrical generators by a two-dipole ranging technique", *Circulation research,* vol. 41, no. 4, pp. 551-557.

Modre, R., Tilg, B., Fischer, G., Hanser, F., Messnarz, B., Seger, M., Schocke, M.F.H., Berger, T., Hintringer, F. & Roithinger, F.X. 2003, "Atrial noninvasive activation

mapping of paced rhythm data", *Journal of cardiovascular electrophysiology,* vol. 14, no. 7, pp. 712-719.

Mozaffarian, D., Benjamin, E.J., Go, A.S., Arnett, D.K., Blaha, M.J., Cushman, M., Das, S.R., de Ferranti, S., Despres, J.P., Fullerton, H.J., Howard, V.J., Huffman, M.D., Isasi, C.R., Jimenez, M.C., Judd, S.E., Kissela, B.M., Lichtman, J.H., Lisabeth, L.D., Liu, S., Mackey, R.H., Magid, D.J., McGuire, D.K., Mohler, E.R.,3rd, Moy, C.S., Muntner, P., Mussolino, M.E., Nasir, K., Neumar, R.W., Nichol, G., Palaniappan, L., Pandey, D.K., Reeves, M.J., Rodriguez, C.J., Rosamond, W., Sorlie, P.D., Stein, J., Towfighi, A., Turan, T.N., Virani, S.S., Woo, D., Yeh, R.W., Turner, M.B. & American Heart Association Statistics Committee and Stroke Statistics Subcommittee 2016, "Heart Disease and Stroke Statistics-2016 Update: A Report From the American Heart Association", *Circulation,* vol. 133, no. 4, pp. e38-e360.

Naghavi, M., Wang, H., Lozano, R., Davis, A., Liang, X., Zhou, M., Vollset, S.E., Ozgoren, A.A., Abdalla, S. & Abd-Allah, F. 2015, "Global, regional, and national age-sex specific all-cause and cause-specific mortality for 240 causes of death, 1990-2013: a systematic analysis for the Global Burden of Disease Study 2013", *Lancet,* vol. 385, no. 9963, pp. 117-171.

Nash, M.P. & Pullan, A.J. 2005, "Challenges facing validation of noninvasive electrical imaging of the heart", *Annals of Noninvasive Electrocardiology,* vol. 10, no. 1, pp. 73-82.

Nielsen, B.F., Cai, X. & Lysaker, M. 2007, "On the possibility for computing the transmembrane potential in the heart with a one shot method: An inverse problem", *Mathematical biosciences,* vol. 210, no. 2, pp. 523-553.

Ohyu, S., Okamoto, Y. & Kuriki, S. 2002, "Use of the ventricular propagated excitation model in the magnetocardiographic inverse problem for reconstruction of electrophysiological properties", *Biomedical Engineering, IEEE Transactions on,* vol. 49, no. 6, pp. 509-519.

Oster, H.S., Taccardi, B., Lux, R.L., Ershler, P.R. & Rudy, Y. 1997, "Noninvasive electrocardiographic imaging: reconstruction of epicardial potentials, electrograms, and isochrones and localization of single and multiple electrocardiac events", *Circulation,* vol. 96, no. 3, pp. 1012.

Pascual-Marqui, R. 1995, "Reply to comments by Hämäläinen, Ilmoniemi and Nunez", *Source Localization: Continuing Discussion of the Inverse Problem (W.Skrandies, Ed.),* , pp. 16-28.

Pennell, D.J. 2010, "Cardiovascular magnetic resonance", *Circulation,* vol. 121, no. 5, pp. 692-705.

Petrutiu, S., Sahakian, A.V., Fisher, W. & Swiryn, S. 2009, "Manifestation of left atrial events and interatrial frequency gradients in the surface electrocardiogram during atrial fibrillation: contributions from posterior leads", *Journal of cardiovascular electrophysiology,* vol. 20, no. 11, pp. 1231-1236.

Pogwizd, S.M., McKenzie, J.P. & Cain, M.E. 1998, "Mechanisms underlying spontaneous and induced ventricular arrhythmias in patients with idiopathic dilated cardiomyopathy", *Circulation,* vol. 98, no. 22, pp. 2404-2414.

Pullan, A., Cheng, L., Nash, M., Bradley, C. & Paterson, D. 2001, "Noninvasive electrical imaging of the heart: theory and model development", *Annals of Biomedical Engineering,* vol. 29, no. 10, pp. 817-836.

Ramanathan, C., Ghanem, R.N., Jia, P., Ryu, K. & Rudy, Y. 2004, "Noninvasive electrocardiographic imaging for cardiac electrophysiology and arrhythmia", *Nature medicine,* vol. 10, no. 4, pp. 422-428.

Ramanathan, C., Jia, P., Ghanem, R., Ryu, K. & Rudy, Y. 2006, "Activation and repolarization of the normal human heart under complete physiological conditions", *Proceedings of the National Academy of Sciences,* vol. 103, no. 16, pp. 6309-6314.

Revishvili, A.S., Wissner, E., Lebedev, D.S., Lemes, C., Deiss, S., Metzner, A., Kalinin, V.V., Sopov, O.V., Labartkava, E.Z., Kalinin, A.V., Chmelevsky, M., Zubarev, S.V., Chaykovskaya, M.K., Tsiklauri, M.G. & Kuck, K.H. 2015, "Validation of the mapping accuracy of a novel non-invasive epicardial and endocardial electrophysiology system", *Europace : European pacing, arrhythmias, and cardiac electrophysiology : journal of the working groups on cardiac pacing, arrhythmias, and cardiac cellular electrophysiology of the European Society of Cardiology,* vol. 17, no. 8, pp. 1282-1288.

Rieta, J.J., Castells, F., Sánchez, C., Zarzoso, V. & Millet, J. 2004, "Atrial activity extraction for atrial fibrillation analysis using blind source separation", *Biomedical Engineering, IEEE Transactions on,* vol. 51, no. 7, pp. 1176-1186.

Roger, V.L., Go, A.S., Lloyd-Jones, D.M., Adams, R.J., Berry, J.D., Brown, T.M., Carnethon, M.R., Dai, S., de Simone, G. & Ford, E.S. 2011, "Heart Disease and Stroke Statistics—2011 Update1", *Circulation,* vol. 123, no. 4, pp. e18-e209.

Roten, L., Pedersen, M., Pascale, P., Shah, A., Eliautou, S., Scherr, D., Sacher, F. & Haissaguerre, M. 2012, "Noninvasive electrocardiographic mapping for prediction of tachycardia mechanism and origin of atrial tachycardia following bilateral pulmonary transplantation", *Journal of cardiovascular electrophysiology,* vol. 23, no. 5, pp. 553-555.

Rudy, Y. 2013, "Noninvasive electrocardiographic imaging of arrhythmogenic substrates in humans", *Circulation research,* vol. 112, no. 5, pp. 863-874.

Sanders, P., Berenfeld, O., Hocini, M., Jaïs, P., Vaidyanathan, R., Hsu, L.F., Garrigue, S., Takahashi, Y., Rotter, M. & Sacher, F. 2005, "Spectral analysis identifies sites of high-frequency activity maintaining atrial fibrillation in humans", *Circulation,* vol. 112, no. 6, pp. 789-797.

Schalij, M.J., van Rugge, F.P., Siezenga, M. & van der Velde, E.T. 1998, "Endocardial activation mapping of ventricular tachycardia in patients : first application of a 32-site bipolar mapping electrode catheter", *Circulation,* vol. 98, no. 20, pp. 2168-2179.

Schuessler, R.B., Kay, M.W., Melby, S.J., Branham, B.H., Boineau, J.P. & Damiano, R.J. 2006, "Spatial and temporal stability of the dominant frequency of activation in human atrial fibrillation", *Journal of electrocardiology,* vol. 39, no. 4, pp. S7-S12.

Seger, M., Modre, R., Pfeifer, B., Hintermuller, C. & Tilg, B. 2006, "Non-invasive imaging of atrial flutter", *Computing in Cardiology*IEEE, , pp. 601.

Shah, A.J., Hocini, M., Xhaet, O., Pascale, P., Roten, L., Wilton, S.B., Linton, N., Scherr, D., Miyazaki, S. & Jadidi, A.S. 2013, "Validation of novel 3-dimensional electrocardiographic mapping of atrial tachycardias by invasive mapping and ablation: a multicenter study", *Journal of the American College of Cardiology,* vol. 62, no. 10, pp. 889-897.

Shahidi, A.V., Savard, P. & Nadeau, R. 1994, "Forward and inverse problems of electrocardiography: modeling and recovery of epicardial potentials in humans", *Biomedical Engineering, IEEE Transactions on,* vol. 41, no. 3, pp. 249-256.

SippensGroenewegen, A., Lesh, M.D., Roithinger, F.X., Ellis, W.S., Steiner, P.R., Saxon, L.A., Lee, R.J. & Scheinman, M.M. 2000, "Body surface mapping of counterclockwise and clockwise typical atrial flutter: a comparative analysis with endocardial activation sequence mapping", *Journal of the American College of Cardiology,* vol. 35, no. 5, pp. 1276.

Skanes, A.C., Mandapati, R., Berenfeld, O., Davidenko, J.M. & Jalife, J. 1998, "Spatiotemporal periodicity during atrial fibrillation in the isolated sheep heart", *Circulation,* vol. 98, no. 12, pp. 1236-1248.

Skipa, O., Sachse, N., Werner, C. & Dossel, O. 2002, "Transmembrane potential reconstruction in anisotropic heart model", *Int.J.of Bioelectromagnetism,* vol. 4, no. 2, pp. 17-18.

Spach, M.S. & Barr, R. 1971, "Physiological correlates and clinical application of isopotential surface maps", *Vectorcardiography,* vol. 2, pp. 131-141.

Spragg, D.D., Dong, J., Fetics, B.J., Helm, R., Marine, J.E., Cheng, A., Henrikson, C.A., Kass, D.A. & Berger, R.D. 2010, "Optimal left ventricular endocardial pacing sites for cardiac resynchronization therapy in patients with ischemic cardiomyopathy", *Journal of the American College of Cardiology,* vol. 56, no. 10, pp. 774-781.

Sun, H., Velipasaoglu, E.O., Berrier, K.L. & Khoury, D.S. 1998, "Electrophysiological imaging of the right atrium using a noncontact multielectrode cavitary probe: study of normal and abnormal rhythms", *Pacing and clinical electrophysiology,* vol. 21, no. 11, pp. 2500-2505.

Taccardi, B. 1963, "Distribution of heart potentials on the thoracic surface of normal human subjects", *Circulation research,* vol. 12, no. 4, pp. 341.

Taccardi, B. 1962, "Distribution of heart potentials on dog's thoracic surface", *Circulation research,* vol. 11, no. 5, pp. 862-869.

Taccardi, B., Arisi, G., Macchi, E., Baruffi, S. & Spaggiari, S. 1987, "A new intracavitary probe for detecting the site of origin of ectopic ventricular beats during one cardiac cycle", *Circulation,* vol. 75, no. 1, pp. 272-281.

Throne, R.D. & Olson, L.G. 1994, "A generalized eigensystem approach to the inverse problem of electrocardiography", *Biomedical Engineering, IEEE Transactions on,* vol. 41, no. 6, pp. 592-600.

Tikhonov, A.N. & Arsenin, V.I. 1977, *Solutions of ill-posed problems,* Winston, Washington, DC.

Tilg, B., Fischer, G., Modre, R., Hanser, F., Messnarz, B. & Roithinger, F.X. 2003, "Electrocardiographic imaging of atrial and ventricular electrical activation", *Medical image analysis,* vol. 7, no. 3, pp. 391-398.

Tilg, B., Fischer, G., Modre, R., Hanser, F., Messnarz, B., Schocke, M., Kremser, C., Berger, T., Hintringer, F. & Roithinger, F.X. 2002, "Model-based imaging of cardiac electrical excitation in humans", *IEEE Transactions on Medical Imaging,* vol. 21, no. 9, pp. 1031-1039.

Tilg, B., Modre, R., Fischer, G., Hanser, F., Messnarz, B. & Roithinger, F.X. 2001, "Imaging of electrical function within the human atrium and ventricle from paced ecg mapping data" in *Functional Imaging and Modeling of the Heart* Springer, , pp. 148-155.

Tung, L. 1978, *A bi-domain model for describing ischemic myocardial dc potentials*, Massachusetts Institute of Technology.

Van Dam, P.M., Oostendorp, T.F., Linnenbank, A.C. & Van Oosterom, A. 2009, "Non-invasive imaging of cardiac activation and recovery", *Annals of Biomedical Engineering,* vol. 37, no. 9, pp. 1739-1756.

Van Wagoner, D.R., Piccini, J.P., Albert, C.M., Anderson, M.E., Benjamin, E.J., Brundel, B., Califf, R.M., Calkins, H., Chen, P.S., Chiamvimonvat, N., Darbar, D., Eckhardt, L.L., Ellinor, P.T., Exner, D.V., Fogel, R.I., Gillis, A.M., Healey, J., Hohnloser, S.H., Kamel, H., Lathrop, D.A., Lip, G.Y., Mehra, R., Narayan, S.M., Olgin, J., Packer, D., Peters, N.S., Roden, D.M., Ross, H.M., Sheldon, R. & Wehrens, X.H. 2015, "Progress toward the prevention and treatment of atrial fibrillation: A summary of the Heart Rhythm Society Research Forum on the Treatment and Prevention of Atrial Fibrillation, Washington, DC, December 9-10, 2013", *Heart rhythm : the official journal of the Heart Rhythm Society,* vol. 12, no. 1, pp. e5-e29.

Volkmer, M., Ouyang, F., Deger, F., Ernst, S., Goya, M., Bänsch, D., Berodt, K., Kuck, K.H. & Antz, M. 2006, "Substrate mapping vs. tachycardia mapping using CARTO in patients with coronary artery disease and ventricular tachycardia: impact on outcome of catheter ablation", *Europace,* vol. 8, no. 11, pp. 968.

Wang, D., Kirby, R.M., MacLeod, R.S. & Johnson, C.R. 2013, "Inverse electrocardiographic source localization of ischemia: An optimization framework and finite element solution", *Journal of computational physics,* vol. 250, pp. 403-424.

Wang, J.Z., Williamson, S.J. & Kaufman, L. 1992, "Magnetic source images determined by a lead-field analysis: the unique minimum-norm least-squares estimation", *Biomedical Engineering, IEEE Transactions on,* vol. 39, no. 7, pp. 665-675.

Wang, L., Wong, K.C.L., Zhang, H., Liu, H. & Shi, P. 2011, "Noninvasive Computational Imaging of Cardiac Electrophysiology for 3-D Infarct", *Biomedical Engineering, IEEE Transactions on,* vol. 58, no. 4, pp. 1033-1043.

Wang, L., Zhang, H., Wong, K., Liu, H. & Shi, P. 2010, "Physiological-model-constrained noninvasive reconstruction of volumetric myocardial transmembrane potentials", *Biomedical Engineering, IEEE Transactions on,* vol. 57, no. 2, pp. 296-315.

Wang, Y., Cuculich, P.S., Woodard, P.K., Lindsay, B.D. & Rudy, Y. 2007a, "Focal atrial tachycardia after pulmonary vein isolation: noninvasive mapping with electrocardiographic imaging (ECGI)", *Heart rhythm: the official journal of the Heart Rhythm Society,* vol. 4, no. 8, pp. 1081-1084.

Wang, Y., Schuessler, R.B., Damiano, R.J., Woodard, P.K. & Rudy, Y. 2007b, "Noninvasive electrocardiographic imaging (ECGI) of scar-related atypical atrial flutter", *Heart rhythm : the official journal of the Heart Rhythm Society,* vol. 4, no. 12, pp. 1565-1567.

Wilson, F.N., Johnston, F.D., Macleod, A.G. & Barker, P.S. 1934, "Electrocardiograms that represent the potential variations of a single electrode", *American Heart Journal,* vol. 9, no. 4, pp. 447-458.

Wittkampf, F.H., Wever, E.F., Vos, K., Geleijns, J., Schalij, M.J., VAN DER TOL, J. & Robles de Medina, Etienne O 2000, "Reduction of radiation exposure in the cardiac electrophysiology laboratory", *Pacing and Clinical Electrophysiology,* vol. 23, no. 11, pp. 1638-1644.

Xi, Q., Sahakian, A.V. & Swiryn, S. 2003, "The effect of QRS cancellation on atrial fibrillatory wave signal characteristics in the surface electrocardiogram", *Journal of electrocardiology,* vol. 36, no. 3, pp. 243-249.

Yamashita, Y. & Takahashi, T. 1984, "Use of the finite element method to determine epicardial from body surface potentials under a realistic torso model", *Biomedical Engineering, IEEE Transactions on,* , no. 9, pp. 611-621.

Yu, L., Zhou, Z. & He, B. 2015, "Temporal Sparse Promoting Three Dimensional Imaging of Cardiac Activation", *Medical Imaging, IEEE Transactions on,* vol. 34, no. 11, pp. 2309-2319.

Zeppenfeld, K., Schalij, M.J., Bartelings, M.M., Tedrow, U.B., Koplan, B.A., Soejima, K. & Stevenson, W.G. 2007, "Catheter ablation of ventricular tachycardia after repair of congenital heart disease: electroanatomic identification of the critical right ventricular isthmus", *Circulation,* vol. 116, no. 20, pp. 2241-2252.

Zhang, X., Ramachandra, I., Liu, Z., Muneer, B., Pogwizd, S.M. & He, B. 2005, "Noninvasive three-dimensional electrocardiographic imaging of ventricular activation sequence", *American Journal of Physiology- Heart and Circulatory Physiology,* vol. 289, no. 6, pp. H2724-H2732.

Zhou, Z., Han, C., Yang, T. & He, B. 2015, "Noninvasive Imaging of 3-Dimensional Myocardial Infarction From the Inverse Solution of Equivalent Current Density in Pathological Hearts", *Biomedical Engineering, IEEE Transactions on,* vol. 62, no. 2, pp. 468-476.

Zhou, Z., Jin, Q., Chen, L., Yu, L., Wu, L. & He, B. 2016a, "Noninvasive Imaging of High Frequency Drivers and Reconstruction of Global Dominant Frequency Maps in

Patients with Paroxysmal and Persistent Atrial Fibrillation", *Biomedical Engineering, IEEE Transactions on,* vol. 63, no. 6, pp. 1333-1340.

Zhou, Z., Jin, Q., Yu, L., Wu, L. & He, B. 2016b, "Noninvasive Imaging of Human Atrial Activation during Atrial Flutter and Normal Rhythm from Body Surface Potential Maps", *PloS one,* vol. 11, no. 10, pp. e0163445.

Zoni-Berisso, M., Lercari, F., Carazza, T. & Domenicucci, S. 2014, "Epidemiology of atrial fibrillation: European perspective", *Clin Epidemiol,* vol. 6, pp. 213-220.